GEOLOGICAL SURVEY OF CANADA
OPEN FILE 6984

Core, petrographic, and rock petrophysical evaluation of the Blue Fiord Formation from wells in the Canadian Arctic Islands

J.C. Wendte

2012

Natural Resources Canada | Ressources naturelles Canada

Canada

GEOLOGICAL SURVEY OF CANADA
OPEN FILE 6984

Core, petrographic, and rock petrophysical evaluation of the Blue Fiord Formation from wells in the Canadian Arctic Islands

J.C. Wendte

2012

doi:10.4095/289887

This publication is available from the Geological Survey of Canada Bookstore (http://gsc.nrcan.gc.ca/bookstore_e.php).
It can also be downloaded free of charge from GeoPub (http://geopub.nrcan.gc.ca/).

Recommended citation:
Wendte, J.C., 2012. Core, petrographic, and rock petrophysical evaluation of the Blue Fiord Formation from wells in the Canadian Arctic Islands; Geological Survey of Canada, Open File 6984, 126 p. doi:10.4095/289887

Publications in this series have not been edited; they are released as submitted by the author.

Frontispiece

The author, Dr. Jack Wendte of the Geological Survey of Canada (GSC) in Calgary, is shown examining core at the GSC's Geological Core and Sample Repository in Calgary, Alberta, Canada.

TABLE OF CONTENTS

ABSTRACT

This report summarizes the lithology, depositional aspects, diagenesis, and reservoir quality of limestones and dolostones of the Late Silurian to earliest Middle Devonian Blue Fiord Formation from the subsurface of the Canadian Arctic Islands. The report focuses on two key aspects. Firstly, the report provides a summary of the depositional facies and diagenetic paragenesis of limestones from the Bent Horn Oil Field on Cameron Island. Secondly, the report provides a detailed summary and interpretation of diagenetic aspects as well as an appraisal of porosity and permeability of dolostones from the three wells on Banks Island.

SYNOPSIS

Introduction

This report summarizes the lithology, depositional aspects, diagenesis, and reservoir quality of limestones and dolostones of the Late Silurian to earliest Middle Devonian Blue Fiord Formation from the Canadian Arctic Islands. It is based on the detailed description of conventional cores from 22 wells, a thorough examination of 274 thin sections taken from these cores, and an evaluation of porosity and permeability primarily based on existing, full-diameter core segments and supplemented by the additional analysis of 36 one-inch diameter core plugs taken during this study.

This study focuses on the Late Silurian to earliest Middle Devonian Blue Fiord Formation because it is judged to have the best potential for gas and oil production of any of the Cambrian, Ordovician, Silurian and Devonian rock units in the Canadian Arctic Islands. It is the main reservoir of the Bent Horn oil field on Cameron Island, the only oil field in the Canadian Arctic Islands. Oil was discovered in 1974 and a total of three oil wells were drilled from 1974 to 1976. Several other wells were drilled on Cameron Island from the mid-1970s to the early 1980s in an unsuccessful effort to extend the field.

Of the three oil wells, oil was produced from one. W. Bent Horn A-02 produced up to 5300 barrels per day of light gravity crude oil (43° API) with minimal water production. Cumulative production from 1985 to 1993 was 321,470 m^3. Two tanker loads a year were shipped from Bent Horn to Montreal on an ice-breaking tanker. W. Bent Horn A-02 was shut-in in 1995. All three oil wells are currently held under Significant Discovery Licences by Suncor Energy Inc.

The Blue Fiord Formation includes two main intervals: firstly, a more widespread interval of probable Late Silurian to Early Devonian age. Cores examined from this interval include those from Prince Patrick and Banks Islands; secondly, a more areally restricted interval limited to reef-fringed carbonate banks of Late Silurian to earliest Middle Devonian age. In addition to cores from 12 wells on Cameron Island, cores from three additional wells on Melville and Vanier Islands were also examined.

In order to discriminate between these two intervals in this report, Late Silurian to earliest Middle Devonian intervals from the more areally restricted carbonates of Cameron, Melville and Vanier Islands are referred to as the Blue Fiord Formation and Late Silurian to Early Devonian intervals from the more areally widespread carbonates of Prince Patrick and Banks Islands are referred to as the “Blue Fiord” Formation.

In addition to this synopsis and an appendix incorporating the results of the analysis of one-inch diameter plugs taken during this study, the report includes detailed summaries from the core intervals on (1) Cameron Island, (2) Melville and Vanier Islands, (3) Prince Patrick Island and (4) Banks Island. These summaries include core photographs and photomicrographs of the thin sections in addition to written texts.

Testing/Analysis Procedures

Thirty-six one-inch diameter core plugs were analyzed for porosity, permeability, bulk density and grain density by AGAT Laboratories in Calgary. The results of this analysis are incorporated in the appendix of this report.

Two hundred seventy-four thin sections were made from 137 samples by Calgary Rock and Materials in Calgary. One set of 137 thin sections was stained with Alizarin Red-S and Potassium Ferricyanide and the other set was not stained. These thin sections are stored at the Core and Sample Repository of the Geological Survey of Canada in Calgary.

Samples were taken from the core intervals on the following lists, from 22 wells whose locations are shown in Synopsis Figure 1.

Cameron Island

1. Bent Horn A-57 10960-11054 ft.
2. Bent Horn F-72 10279-10443 ft.
3. Bent Horn F-72A 10120-10168 ft., 10216-10310 ft., 10695-10704 ft., 10716-10728 ft.
4. Bent Horn N-72 10520-10537 ft., 10720-10739 ft., 10500-11530 ft.
5. Cape Fleetwood M-21 10912-10967 ft., 11500-11528 ft.
6. W. Bent Horn A-02 9056-9146 ft., 11000-11025 ft.
7. W. Bent Horn E-43 10080-10168 ft., 11000-11060 ft.
8. W. Bent Horn G-02 2755-2789 m, 3099.6-3136 m
9. W. Bent Horn I-01 10667-10688 ft.
10. W. Bent Horn I-01A 10145-10205 ft.
11. W. Bent Horn M-12 9161-9217 ft., 10505-10564 ft.
12. W. Bent Horn C-44 10444-11504 ft.

Melville Island

13. King Point West B-53 3606-3626.5 ft.
14. Richardson Point G-12 7903-7962.5 ft., 9690-9735 ft.

Vanier Island

15. Key Point O-51 7359-7419 ft.

Prince Patrick Island

16. Dyer Bay L-49 10373-10405 ft.
17. Wilkie Point J-51 5900-5916 ft.

Banks Island

18. Kusrhaak D-16 11995-12025 ft., 12450-12477.5 ft.
19. Muskox D-87 2073-2091 m
20. Parker River J-72 949-960 m, 1002-1005 m
21. Storkerson Bay A-15 6446-6473.5 ft.
22. Tiritchik M-48 4631-4639.5 ft.

Description of Results

– All the intervals from cores of the Blue Fiord Formation on Cameron Island consist of limestones. Deposition of carbonates from these intervals occurred on a reefal foreslope. Porosities measured from either full-diameter core pieces or one-inch diameter core plugs are in most cases approximately one to one and a half percent or less. Matrix permeabilities are mainly less than 0.01 mD. Some fractures are still open.

- All the intervals from cores of the Blue Fiord Formation on Melville and Vanier Islands also consist of limestones. Deposition of carbonates from these intervals occurred on reefal foreslopes. Porosities measured from either full-diameter core pieces or one-inch diameter core plugs are in most cases approximately one percent or less. Matrix permeabilities are mainly less than 0.01 mD.
- All the intervals from cores of the "Blue Fiord" Formation on Prince Patrick Island consist of limestones. They have no observable porosity or permeability.
- The intervals from cores of the "Blue Fiord" Formation on Banks Island consist of both limestones and dolostones. The limestone intervals occur in Tiritchik M-48 (4631-4639.5 ft.), Storkerson Bay A-15 (6446-6473.5 ft.) and Parker River J-72 (949-960 m). These core intervals have no visible porosity and permeability.
- The dolostone core intervals occur in Parker River J-72 (1002-1005 m), Muskox D-87 (2073-2091 m) and Kurshaak D-16 (11995-12025 ft. and 12450-12477.5 ft.). The dolostones in Muskox D-87 are characterized by the occurrence of zebroid fabrics and vugs of dissolution origin. Porosities measured from full-diameter pieces range from 0.09% to 8.5%, with an average porosity of 3.94%. K_{max}'s of these intervals range from 0.01 mD to 2350 mD, with an average K_{max} of 68.31 mD. However, 38 of the 43 full-diameter pieces have K_{max}'s less than 10 mD (0.01 mD to 8.80 mD), with an average K_{max} of 1.41 mD.

  The dolostones in both cores from Kurshaak D-16 (11995-12025 ft. and 12450-12477.5 ft.) consist of mainly dolobreccias. Only the lower core interval was analyzed for porosity and permeability. Porosities measured from full-diameter pieces range from 0.8% to 4.1%, with an average porosity of 2.1%. K_{max}'s of these intervals range from 0.04 mD to 11.10 mD, with an average permeability of 2.13 mD.

  The dolostones in the lower core interval (1002-1005 m) of Parker River J-72 consist of very fine to fine (sand-sized) crystalline dolomites. Porosities measured from full-diameter samples range from 4.5% to 13.8%, with an average porosity of 7.46%. K_{max}'s of these intervals range from 0.8 mD to 50.4 mD.

Interpretation of Results

Oil production from the Bent Horn oil field on Cameron Island is through fractures. The common attribution of oil production from this field from karst vugs and caverns is a myth. There is no evidence from the cores or drilling times recorded on the tower sheets to support this interpretation. The best chance of encountering open fractures in future wells is from horizontal wells.

The limestone intervals on Melville and Vanier Islands have only rare observable pororsity. They have no reservoir quality.

The limestone intervals on Prince Patrick and Banks Islands lack observable porosity and permeability. They have no reservoir quality.

The dolostones on Banks Island have porosities and permeabilities capable of sustaining hydrocarbon recovery. They are interpreted to be fault-controlled hydrothermal dolomites. Three-D seismic analysis would aid in delineating traps of this type.

Implications for Future Work

The understanding of dolomitization is critical for future exploration. Analytical geochemical analysis will aid in verifying the interpretation of hydrothermal dolomitization of "Blue Fiord" carbonates on Banks Island. Toward this goal, I would recommend (1) stable oxygen and carbonate isotopic analyses of both matrix dolomites and saddle dolomite cements, (2) radiogenic Sr-isotope analyses of both matrix dolomites and saddle dolomite cements, and (3) two-phase aqueous fluid inclusion analysis of saddle dolomite cements. I would also recommend running these analyses on macrocalcite cements that follow the formation of saddle dolomites, infilling pores sheltered beneath dolobreccia clasts, in the Kurshaak D-16 well. Geochemical characterization of these calcite cements may allow for understanding the change from saddle dolomite to calcite cement.

Synopsis Figure 1

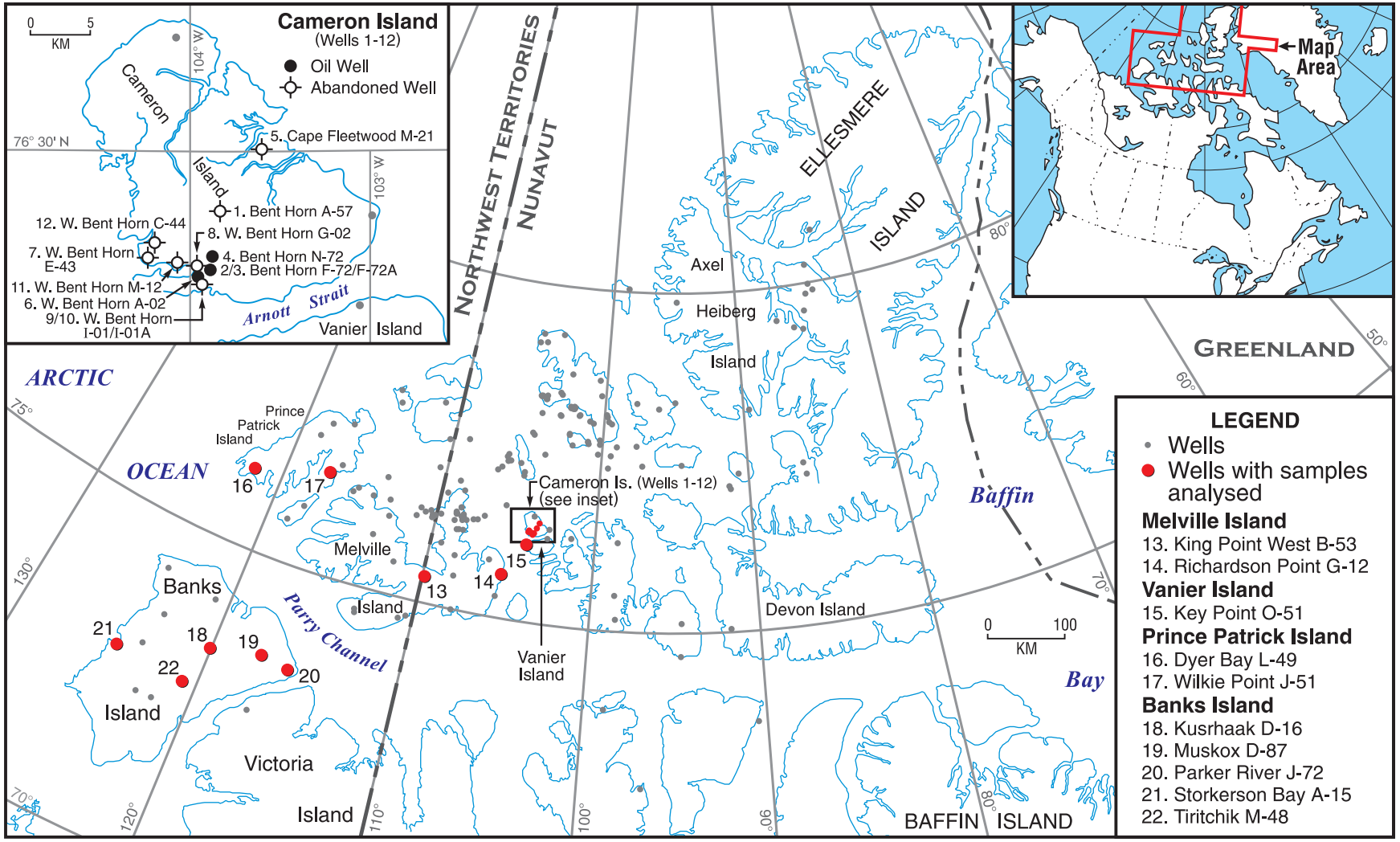

Map of Canadian Arctic Islands showing location of wells with cores examined during this study. Well numbers correspond to those listed for wells noted in the Synopsis of this report.

SECTION A: SUMMARY OF CORES AND THIN SECTIONS OF THE BLUE FIORD FORMATION FROM CAMERON ISLAND, INCLUDING THOSE FROM THE BENT HORN OIL FIELD

Characterization of the Bent Horn Oil Field

Oil in the Bent Horn Oil Field occurs in limestones of the Lower and Middle Devonian Blue Fiord Formation. These limestones make up the upper part of an isolated, reef-rimmed carbonate bank, up to an estimated thickness of 1200-1500 m, of Late Silurian to earliest Middle Devonian age.

These limestones were buried to an estimated depth of 3 to 5 km from loading by terrigenous clastic strata from Middle to Late Devonian time. Limestones of the Blue Fiord Formation were then displaced by thrusting from latest Devonian to earliest Carboniferous time, followed by rapid subsidence due to rifting related to the opening of the Sverdrup Basin between Early Carboniferous and Mid-Permian time.

Oil was discovered in 1974 and a total of three oil wells were drilled near the southern coast of Cameron Island, from 1974 to 1976. Of these wells, only one (W. Bent Horn A-02) was capable of sustained production, with a cumulative production between 1985 and 1993 of 321,470 m^3, but was shut in in 1995. Several other wells were drilled on Cameron Island from the mid-1970's to the early 1980's in an unsuccessful effort to extend the field.

The present study is based on the detailed examination of cores from 12 wells. Of these wells, 10 are located near the southern margin of the isolated bank, near the southern coast of Cameron Island, and two further north near the eastern margin of the isolated bank.

Despite the numerous penetrations, only foreslope facies were encountered in the cores. The majority of rocks in these cores are clast or grain-supported limestones of two main types. The first type are floatstones and rudstones that contain fragments of tabular stromatoporoids and tabular tabulate corals, and have peloidal-skeletal grainstone or low-mud packstone matrices (Figures A1, A2, and A3). These rocks are interpreted as debris deposited on the upper and intermediate portions of a reefal foreslope. The second type are peloidal and skeletal grainstones and low-mud packstones (Figures A4 and A5). These rocks consist of either finely broken-up reef-formers, commonly micritized to form peloids, or smaller skeletal constituents, such as crinoid columnals. These low-mud packstones and grainstones are interpreted as foreslope sands deposited further downslope. A less common occurring lithology are floatstones containing both laminar and branching tabulate corals (Figures A6 and A7). These floatstones commonly have wackestone matrices, and are interpreted to have been deposited in relatively deep water foreslope settings, close to where the corals grew.

Rocks of the foreslope facies had very high depositional porosities, consisting of interparticle and intraskeletal pores. However, practically all these pores are infilled by calcite cements. Porosities measured from either full-diameter core pieces or small-diameter plugs are in most cases approximately one to one and a half percent or less (refer to the analysis of small-diameter core plugs in the appendix). Maximum permeabilities measured from these intervals are mainly less than 0.01 mD.

The cements that infill these pores are of two main varieties (Figure A8). Firstly, radiaxial calcite crystals occur as isopachous linings around particles. Multiple generations of these cements occur within large depositional cavities. Overall, infilling by these cements reduced porosity by only a very small amount. Secondly, equant crystals of non-ferroan calcite infilled the remainder of the primary pores. The precipitation of these calcites followed that of the radiaxial calcites and these cements are the main pore filler of matrix pores in limestones of the Blue Fiord Formation. Crystals generally coarser than 100 (?) microns are twinned.

Extensive micropores of dissolution origin and some solution vugs are also present. However, almost all of these voids are infilled by bitumen. Micropores of dissolution origin occur most commonly in the peloids and to a lesser degree in skeletal particles and in the laminae and pillar of stromatoporoids and the tabulae and septae of corals (Figures A9 and A10). Some solution vugs are present and occur mainly

within equant calcite cements, some of which infill fractures. In most of these cases, the solution vugs occur along and adjacent to crystal contacts (Figure A11) and along or adjacent to the contacts between the calcite cements and the adjacent stromatoporoid or coral fragments. These positions would have been preferential pathways of fluid flow. Some of the bitumen-infilled vugs within equant calcite cements also occur along the traces of horizontal trending stylolites (Figure A12). Some of the solution vugs also extend into adjacent crystals of dolomite and barite.

Despite the lack of either observable or measured porosity, all core pieces released an oil scum when etched with hydrochloric acid. The oil is interpreted to be residual and is thought to be somehow intermixed with the bitumen.

Both macro and micro hairline fractures occur commonly in limestones of the Blue Fiord Formation. The macro-fractures are most commonly completely infilled by calcite and some barite, although some remain partially open (Figure A13). The intensity of fracturing and brecciation increases in proximity to thrust faults (Figures A14 and A15). Some of the macro-fractures appear to be of dilational origin (Figure A16). The hairline micro-fractures occur most commonly in fragments of stromatoporoids and corals. These micro-fractures cut both the walls of these components and the equant calcites infilling their chambers (Figure A17). They are infilled by bitumen.

Sustained oil production is attributed to be from partially open macro-fractures in the portion of the Blue Fiord Formation that occurs in repeated thrust-fault slices along the southern margin of the bank. Only three of the 10 wells in this part of the bank were deemed to be capable of oil production. I interpret this to result from the calcite cementation and the infilling by bitumen of not only the matrix pores of the Blue Fiord Formation, but also of the fractures.

Diagenetic Minerals

Radiaxial calcite occurs most commonly, as previously noted, as isopachous cements around grains and within large depositional cavities. In one case, radiaxial calcite lines the interior of a biomold of an aragonitic grain of uncertain affinity (Figure A18). In another case, a narrow band within a multiple generation of radiaxal calcite has been completely dissolved along the sides of the depositional cavity. The void created by this dissolution has been infilled, geopetally, by marine internal sediment and by a later generation of equant, non-ferroan calcite (refer to Figure A8).

Equant non-ferroan calcites, as previously noted, infill all visible interparticle and intraskeletal pores, as well as most macro-fractures. Coarse crystals of equant calcite infilling both matrix pores and fractures are twinned. Relatively coarse crystals of bladed calcite also infill some fractures.

Dolomite occurs both as a replacive phase and rarely as a cement. Replacive dolomite is commonly ferroan or weakly ferroan and occurs as rhombs. In most cases, replacive dolomite occurs as minor small rhombs, with crystal diameters less than 100 microns, scattered throughout the matrix. In a few cases, replacive dolomite forms small patches or selectively replaces the micritic matrix in packstones containing remnant calcitic skeletal grains (Figure A19). In these cases, the dolomite forms a planar-s mosaic (Figure A20). Even more rarely, dolomite crystals replace the initial phase of radiaxial calcite cement that lines large cavities (Figure A21). In this mode, the dolomite appears to occur as a cement with an isopachous lining around the cavity, but is in fact replacive. In one thin section, dolomite was observed as a cement growing off from replacive dolomite rhombs (Figure A22). In this case, the dolomite crystals have well-developed scalenohedral crystal facies. These dolomite crystals are overgrown by later equant crystals of non-ferroan calcite cement.

Barite occurs commonly in fractures and, to a much lesser extent, in shelter cavities. In the Blue Fiord Formation, barite commonly occurs as tabular-shaped crystals that both overgrow and are overgrown by equant crystals of non-ferroan calcite (Figure A23). Some of the fractures in which barite occurs cut patches consisting of replacement dolomites. Barite also occurs as radiating fibrous forms, infilling fractures in both limestones of the Blue Fiord Formation and in quartzose siltstones and very-fine

sandstones within a faulted slice of the Cape De Bray (?) Formation in one core (well Bent Horn F-72A) (Figure A24).

Fluorite was not observed in cores of the Blue Fiord Formation, but was observed as cubic crystals in quartzose siltstones and very-fine sandstones in a faulted slice of the Cape De Bray (?) Formation (well Bent Horn F-72A). In this occurrence, cubic crystals of fluorite are commonly associated with, and overgrown by, tabular crystals of barite (Figure A25).

Sphalerite occurs commonly but in minor concentrations in core from one well (Bent Horn I-01A) in the Blue Fiord Formation. Three modes of occurrence were noted. Firstly, sphalerite occurs as botryoidal growths lining one fracture that occurs immediately above a trace of a thrust fault within the Blue Fiord Formation (Figure A26). These botryoidal growths of sphalerite are overgrown by and cut by fractures infilled by calcite cement. Secondly, sphalerite occurs as anhedral replacive masses that occur along the trace of near-vertical stylolites (Figure A27). Thirdly, sphalerite occurs as anhedral replacive masses associated with quartzose siltstones infilling a narrow, mm-scale near-vertical fissure. In this case, the vertical fissure is cut through equant calcite cements that infill a fracture (Figure A28). Rare discrete crystals of sphalerite were noted in cores from other wells, including Bent Horn F-72A where it occurs in association with barite in a faulted slice of the Cape De Bray (?) Formation (refer to Figure A24).

Euhedral crystals of authigenic quartz occurs in minor concentrations in some cores. These crystals occur as replacement of limestone either scattered throughout the matrix or along the traces of near-vertical stylolites (Figure A29).

Diagenetic Phases

The Blue Fiord Formation at Bent Horn has undergone multiple phases of diagenesis. The initial phase was either at or just beneath the sea floor, from marine or modified marine waters. The second phase of diagenesis corresponds to the burial from loading of foreland basin deposits, shed from the rising Ellesmerian highlands during Middle Devonian to Late Devonian time. During this phase, the Blue Fiord Formation at Bent Horn is estimated to have been buried to a depth of 3-5 km. The third phase of diagenesis corresponds to the episodes of imbricate thrusting of the Blue Fiord Formation during the continuation of the Ellesmerian orogeny, during latest Devonian to earliest Carboniferous time. At Bent Horn, thrusting was from the south and displaced Blue Fiord strata along the southern margin of the isolated bank. The fourth phase is the extension and burial related to the opening of the Sverdrup Basin from Early Carboniferous to Mid-Permian time.

The attribution of diagenetic processes or products to these phases is based on the identification of elements that are considered to be diagnostic of these phases. The early marine phase is characterized by calcite cements with typical marine fabrics (refer to Figures A8, A18, and A21). Attribution of diagenesis during the burial from Middle Devonian to Late Devonian time is based on the presence of diagenetic elements that precede structural deformation due to thrusting or extensional tectonics. Identification of diagenesis during the phase of thrust faulting from latest Devonian to earliest Carboniferous time is based on discerning a relationship with compressive elements such as near-vertical stylolites (refer to Figures A14, A15, A27, and A29), granulated or brecciated rock textures (refer to Figures A14 and A27), and even micro-scale thrust faulting (to be documented later). The attribution of diagenetic processes and products to a later extensional phase during the opening of the Sverdrup Basin in later Carboniferous time is more speculative because of the lack of identification of mega-scale extensional structures, such as grabens, at Bent Horn, although normal faults occur approximately 10 km east of the Bent Horn complex and grabens are known to occur on adjacent Bathurst Island and in the offshore. The only elements at Bent Horn considered to be diagnostic of this phase of deformation are extensional micro-structures that can be demonstrated to affect both the Blue Fiord Formation and overlying strata (refer to Figure A28).

The discrimination between processes and products of the third and fourth diagenetic phases is particularly challenging and, in many cases, unresolvable. There are many reasons for this uncertainty. Firstly, there are multiple episodes of fracturing, which in some or in many cases cannot be objectively

related to a distinct phase of deformation. Secondly, relationships with certain diagnostic elements may not be restrictive to a certain phase of deformation. For example, the presence of some mineral occurrences along near-vertical stylolites may not be restrictive to the phase of thrust faulting. The presence of near-vertical stylolites implies horizontal compression and is itself conclusive evidence of formation during the thrusting phase. However, the minerals that occur along near-vertical stylolites may have precipitated from fluids that moved along the stylolites during a later extensional phase, when the stylolites may have opened. Thirdly, there is a paucity of diagenetic features that can be associated with extensional deformation. Fourthly, distinct generations of equant calcite cements that infill fractures cannot be related to distinct phases of diagenesis in many cases. Fifthly, there is a total lack of available good quality seismic lines along the southern margin of the isolated carbonate bank needed to identify extensional structures and to identify and map the thrust faults.

Paragenesis

During the initial phase of diagenesis, some pores in the foreslope facies were infilled by cements that precipitated from marine waters. The most common of these cements are multiple generations of radiaxial calcite cements that form an isopachous lining around large cavities (refer to Figures A8, A18, and A21). Most of these cements precipitated in voids of primary origin, but in one sample line the interior of biomolds formed by the dissolution of aragonite (refer to Figure A18). I interpret that dissolution of aragonite occurred from modified marine waters in the very shallow subsurface. In another case, a generation of cement within an overall succession of isopachous radiaxial cements infilling a large cavity was completely dissolved along the sides of the cavity. The void was partly infilled by marine internal sediment and later by equant calcite cements (refer to Figure A8). I interpret that the generation of cement may have been aragonite which dissolved in modified marine waters in the very shallow subsurface.

During the second phase, the Blue Fiord Formation was buried to an estimated depth of three to five kilometres. Two diagenetic episodes are attributed to this phase. Firstly, but of least importance, is replacement dolomite formation (refer to Figures A19, A20, and A21). Because dolomite only replaces depositional particles and radiaxial calcite marine cements, dolomitization is interpreted to have occurred in the shallow subsurface. Secondly, equant crystals of non-ferroan calcite infill most of the matrix pores, reducing matrix porosity to values approaching zero (refer to Figures A8, A18, and A21). Logically, cementation occurred from the precipitation of calcium carbonate liberated from the host limestones by pressure solution during progressive burial. These cements are cut by fractures that formed in either the third or fourth diagenetic phases.

The origin of micropores of dissolution origin is uncertain. One possibility is that dissolution occurred relatively early in the second phase of diagenesis, before cementation by equant calcite had appreciably reduced porosity and permeability. Obviously, dissolution would be favoured at a time of higher fluid flow when matrix permeability was high. An alternative explanation is that dissolution to form micropores occurred during the same phase as calcite dissolution in the formation of the larger vugs. This possibility is discussed later in this section.

The remaining diagenetic episodes are attributed to either the phase of thrust faulting (the third diagenetic phase) or a later extensional period of deformation (the fourth diagenetic phase). These episodes include extensive fracturing; calcite cementation of the fractures; the formation of fluorite, barite and sphalerite; authigenic quartz formation; the macro-scale dissolution of calcite and rarely barite and dolomite; possibly the micro-scale dissolution of calcite; calcite neomorphism; and lastly, the migration of oil into pores and its eventual transformation to bitumen.

Of these, the only diagenetic episodes that can be attributed with confidence to the phase of thrust faulting are the neomorphism of calcite, the formation of certain fractures and the precipitation of fracture-filling equant calcite cements in some cases. In one occurrence, extensive neomorphic calcite selectively occurs in the hanging wall of a micro-thrust fault, suggesting neomorphism during the phase of thrusting (Figure A30).

The increased density of fractures, in some intervals, toward the trace of thrust faults provides evidence that these fractures formed during the phase of thrust faulting (refer to Figures A14 and A15). As well, some bitumen-infilled micro-hairline fractures are truncated along steeply inclined or near-vertical stylolites (Figure A31). Thus, in the latter case, the final phase of compression and stylolite formation followed the episode of micro-fracturing. Therefore, the formation of these micro-fractures is attributed to the preceding part of the phase of thrust faulting. Overall, it is interpreted that the majority, but not all, of the fracturing occurred during the thrust faulting of the third diagenetic phase.

Some fracture-filling equant calcites are also cut by near-vertical stylolites (refer to Figure A29). Obviously, the equant calcites preceded the final phase of the formation of these compressional stylolites, which occurred during the phase of thrust faulting.

Despite occurring along near-vertical stylolites, sphalerite is interpreted to have formed during the fourth or extensional phase of deformation. The crucial observation to support this interpretation is that crystals of sphalerite are associated with quartz silt infilling a narrow, mm-scale, near-vertical fissure in one well (Bent Horn I-01A) (refer to Figure A28). The fissure cuts coarse crystals of equant calcite that infilled a near-vertical fracture. The formation of a near-vertical, open fissure implies extension. The infiltration and infilling by quartz silt implies that the fissure was open to a level above the top of the Blue Fiord Formation. The occurrence of sphalerite along near-vertical stylolites elsewhere in the same well suggests that these stylolites were opened during an extensional phase prior to sphalerite formation.

Formation of micropores of dissolution origin may be interpreted to be part of the same dissolution episode as macro-vug formation. Some of the vugs cut across crystals of equant calcite and rarely barite that infill fractures (refer to Figure A11). This implies dissolution during either the third or fourth diagenetic phase.

Other macro-solution vugs occur within equant crystals of non-ferroan calcite along the trace of horizontal-trending stylolites (refer to Figure A12). This implies that dissolution of calcite occurred from fluids that flowed along these stylolites once they had opened. This most likely would have happened from the relaxation of vertical stresses during the uplift associated with thrust faulting of the third depositional phase. From this it can be concluded that the dissolution of calcite to form macro-vugs occurred during either the third diagenetic phase or at the beginning of the fourth diagenetic phase prior to significant burial.

Calcite cementation of fractures may have occurred in either the third or fourth diagenetic phase. As previously noted, the truncation of some fracture-infilling calcite cements by near-vertical stylolites in certain cases implies that equant calcite was present before the end of the phase of thrust faulting (refer to Figure A29). In many cases, the attribution of equant calcite infilling fractures to a distinct diagenetic phase is equivocal.

Authigenic quartz occurs along some near-vertical stylolites (refer to Figure A29). This implies formation in either the third compressive diagenetic phase or in the fourth extensional phase when the near-vertical stylolites may have opened. Barite and fluorite formed during either thrusting (the third diagenetic phase) or extension (the fourth diagenetic phase).

Bitumen occurs as an infill of micropores of dissolution origin (refer to Figures A9 and A10), dissolution vugs (refer to Figures A11 and A12), micro-fractures (refer to Figure A17) and both horizontal and near-vertical stylolites (refer to Figures A12, A14, A15, A27, A31, and A32), as well as overgrowing calcite crystals infilling some fractures (Figure A32). Its formation followed that of all previous mineral phases. The migration of oil into the isolated bank complex is interpreted to have occurred during an episode of rapid burial and relatively high heat flow during the opening of the Sverdrup Basin. Bitumen apparently formed from the subsequent over-cooking of the oils.

Figure A1

Massive stromatoporoid clast (S)-*Stachyodes* rudstone-floatstone with a bitumen-bearing skeletal-peloidal grainstone (or low-mud packstone) matrix. Bitumen also fills hairline micro-fractures cutting the stromatoporoid clasts. Photograph taken of a wetted core surface. Foreslope debris facies, Bent Horn N-72, 10732.75 ft.

Figure A2

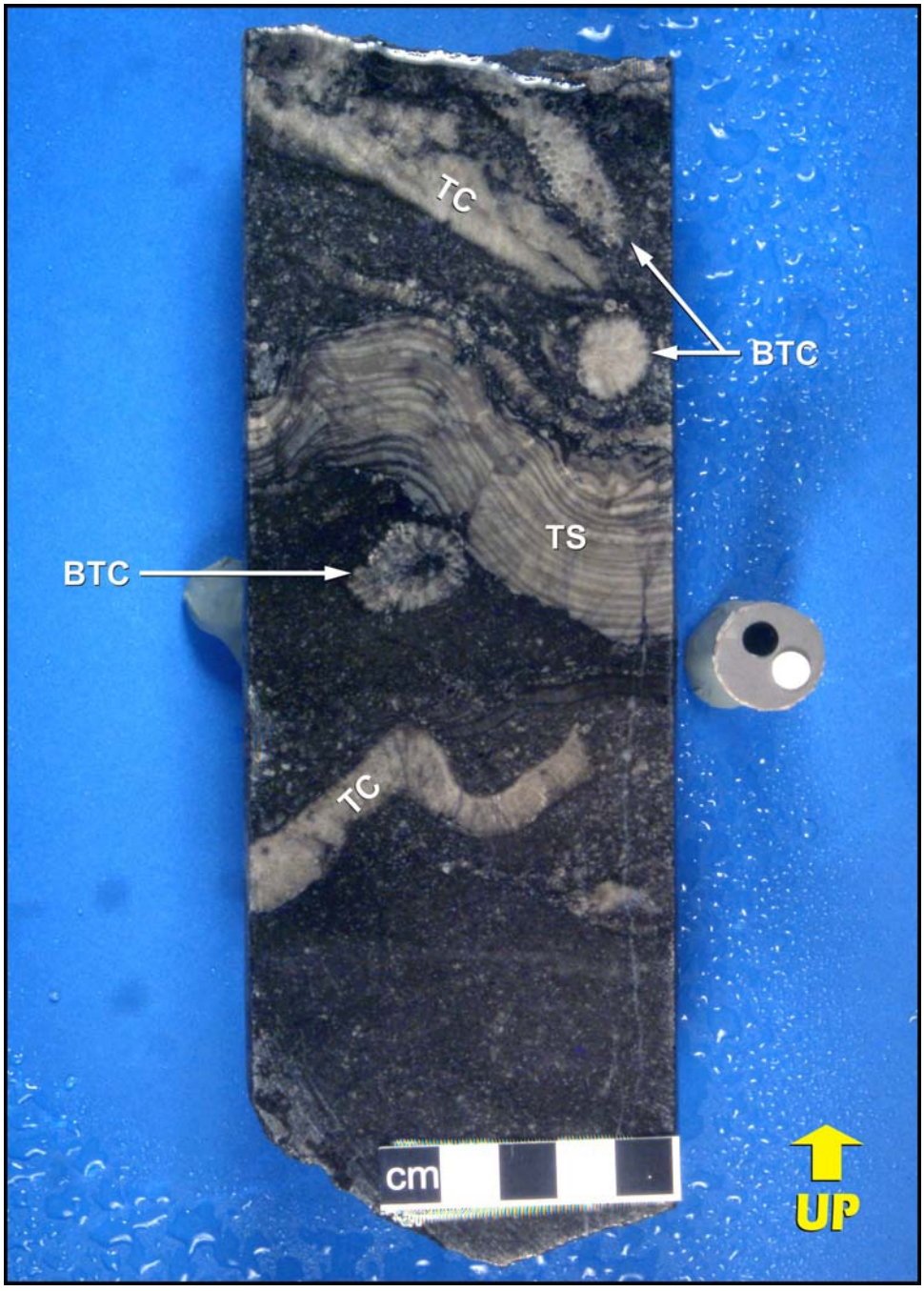

Stromatoporoid-tabulate coral clast floatstone with a bitumen-bearing peloidal-skeletal grainstone (or low-mud packstone) matrix. Large bioclasts include a tabular stromatoporoid (TS), a thinner laminar tabulate coral (TC) and some branching tabulate coral fragments (BTC). Photograph taken of a wetted core surface. Foreslope debris facies, W. Bent Horn G-02, 2766.99 m.

Figure A3

Tabulate coral clast floatstone with a bitumen-bearing skeletal-peloidal grainstone (or low-mud packstone) matrix. Photograph taken of a wetted core surface. Foreslope debris facies, Bent Horn F-72, 10358.50 ft.

Figure A4

Bitumen-bearing, planar cross-stratified, peloidal-skeletal grainstone. Coarse intervals contain large crinoid columnals and fragmented brachiopods. Photograph taken of a wetted core surface. Foreslope sand facies, W. Bent Horn E-43, 11016.50 ft.

Figure A5

Bitumen-bearing skeletal-peloidal low-mud packstone containing abundant crinoid columnals. Photograph taken of a wetted core surface. Foreslope sand facies, Bent Horn F-72, 10374.00 ft.

Figure A6

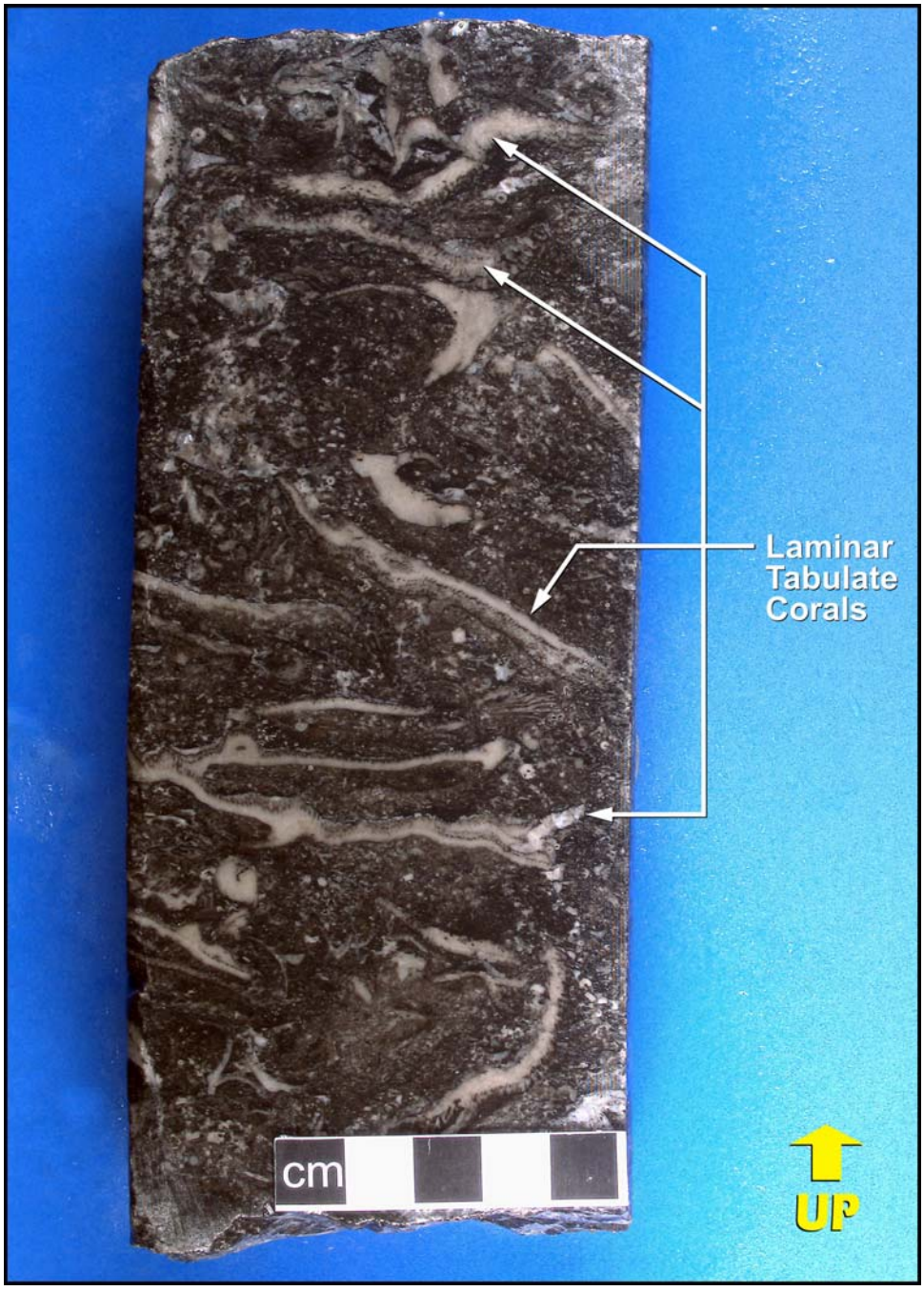

Laminar tabulate coral floatstone with a bitumen-bearing peloidal-skeletal low-mud packstone matrix. The grain-support texture of this rock is uncharacteristic for this facies. Note the branching form of one laminar coral (arrows). Photograph taken of a wetted core surface. Laminar-branching coral facies, Bent Horn A-57, 10998.50 ft.

Figure A7

Branching tabulate coral floatstone with a bitumen lean, pyritic mottled matrix. Photograph taken of a wetted core surface. Laminar-branching coral facies, W. Bent Horn M-12, 10560.84 ft.

Figure A8

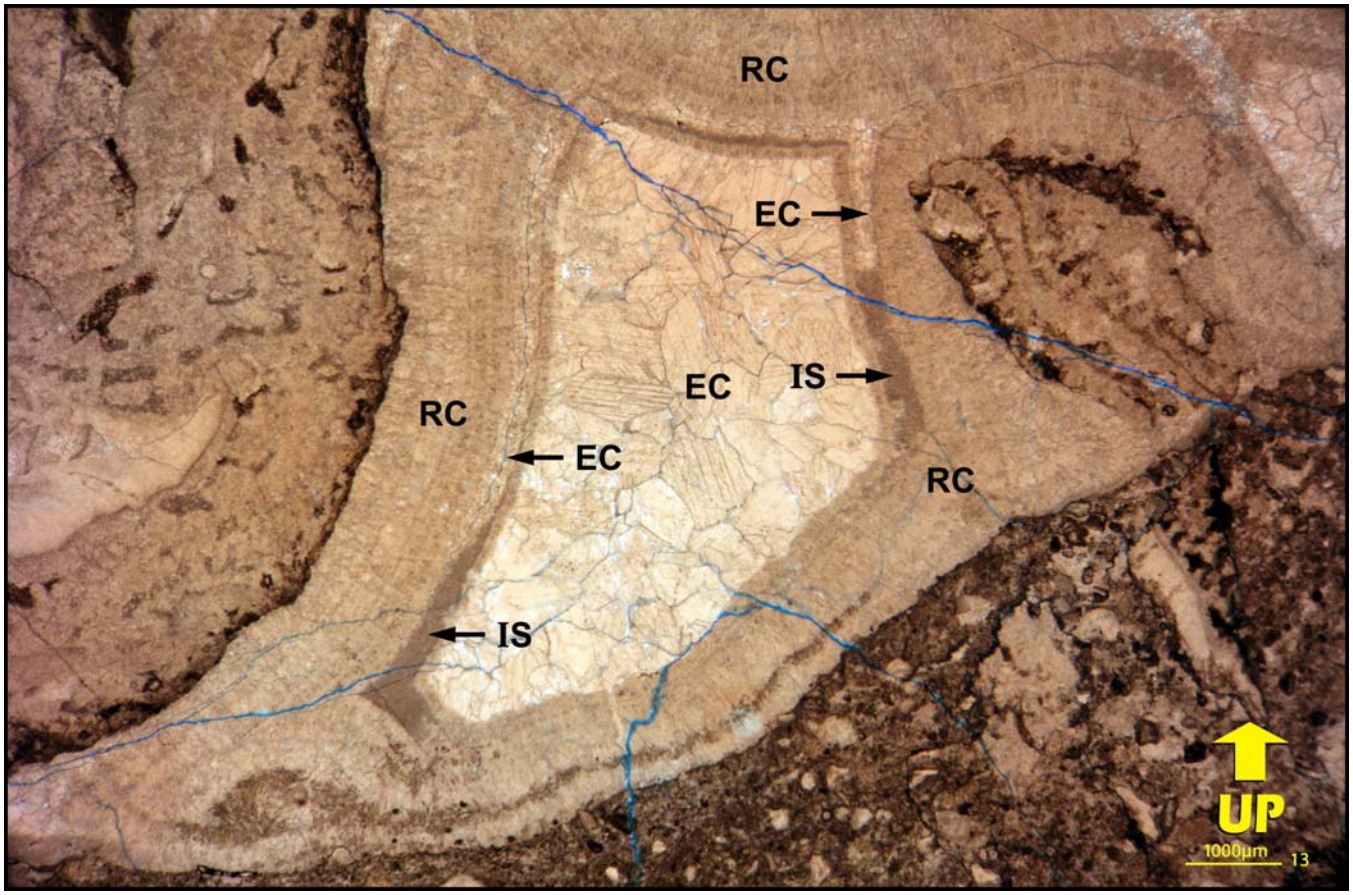

Photomicrograph, taken using a binocular microscope, of calcite cements infilling a large depositional cavity. Two varieties of calcite cement are present. Firstly, multiple generations of radiaxial calcite (RC) form an isopachous rind around the cavity. These cements are interpreted to have precipitated from marine waters pumped through foreslope deposits. Note that a thin cement interval within these generations has been completely dissolved along the sides of the cavity. This interval of cement is only partially dissolved along the base of the cavity. The void created by this dissolution was infilled by marine geopetal internal sediment (IS) and by a later generation of equant calcite cement (EC). Secondly, equant crystals of non-ferroan calcite (EC) precipitated during a later interval and completely infilled the cavity. These cements are the main filler of macroscopic voids in the Blue Fiord Formation at Bent Horn. Transmitted plane-polarized light, Bent Horn F-72, 10378.50 ft.

Figure A9

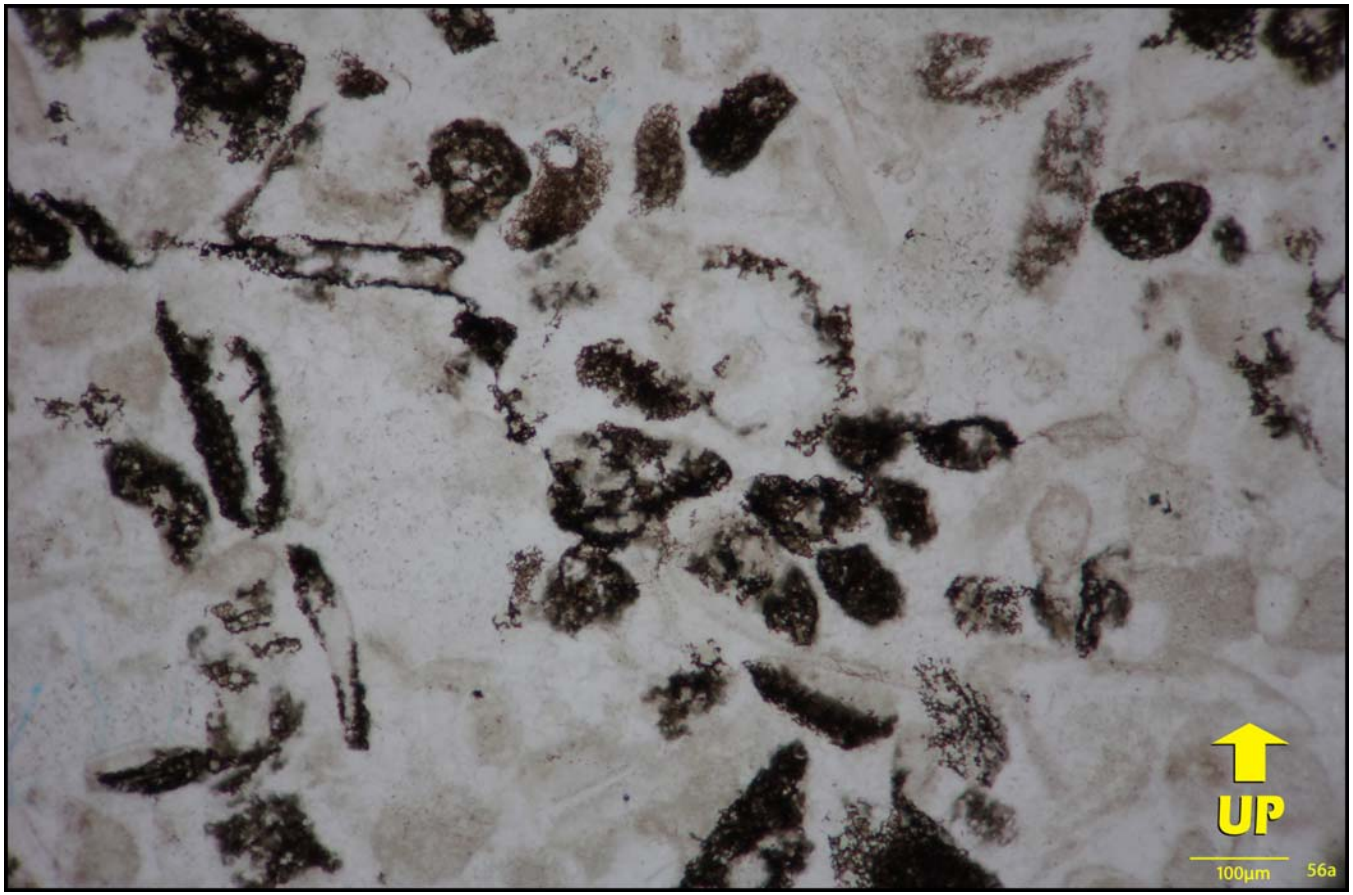

Photomicrograph illustrating the occurrence of bitumen infilling micropores of dissolution origin within peloids in a peloidal-skeletal grainstone. Bitumen is most readily identified from examination under diffused plane-polarized microscopy, such as used here. Photomicrograph taken using diffused plane-polarized light. W. Bent Horn E-43, 11021.70 ft.

Figure A10

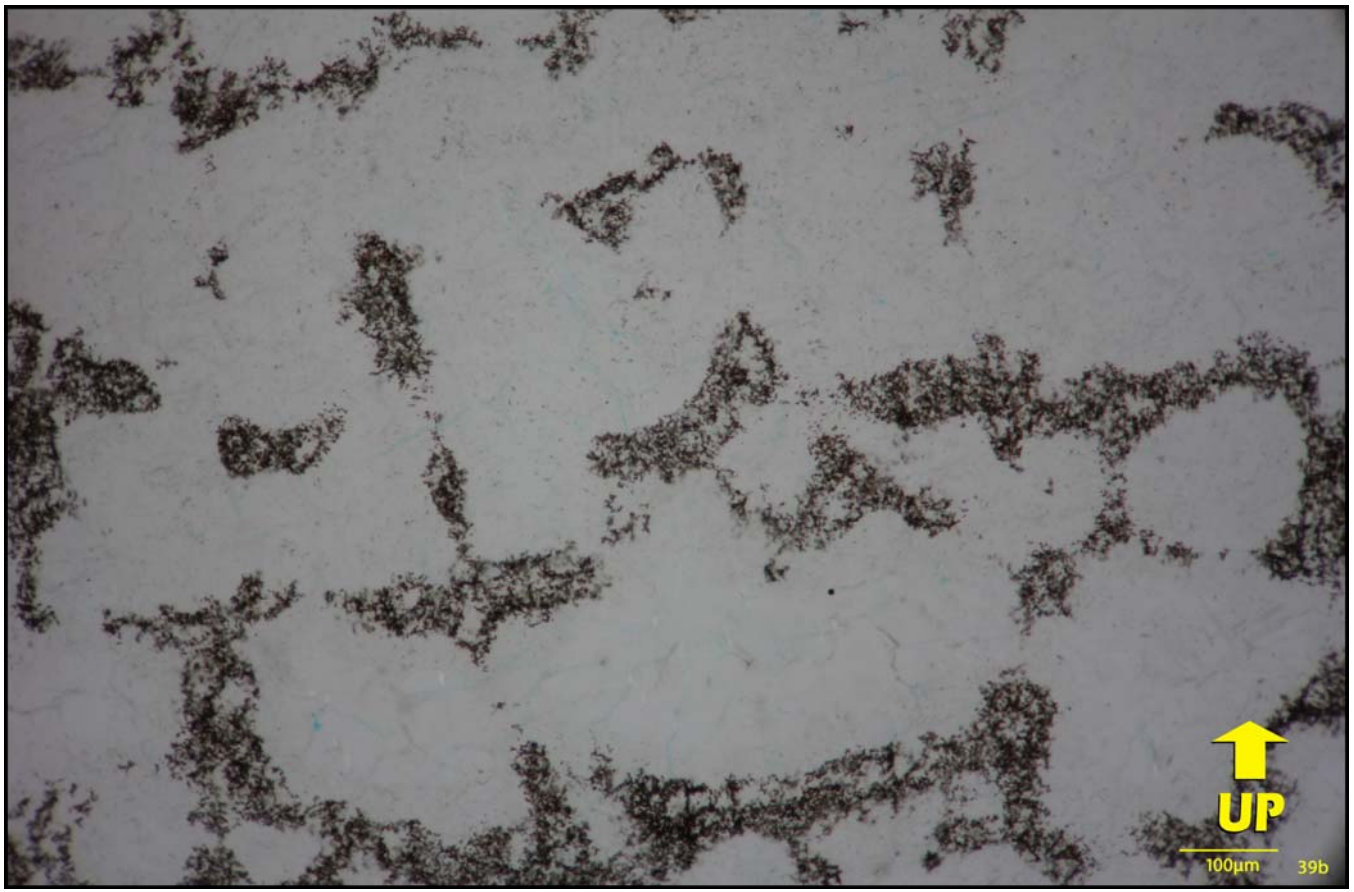

Photomicrograph illustrating the occurrence of bitumen infilling micropores of dissolution origin in the laminae and pillars of a stromatoporoid. Photomicrograph taken using diffused plane-polarized light. Cape Fleetwood M-21, 11503.00 ft.

Figure A11

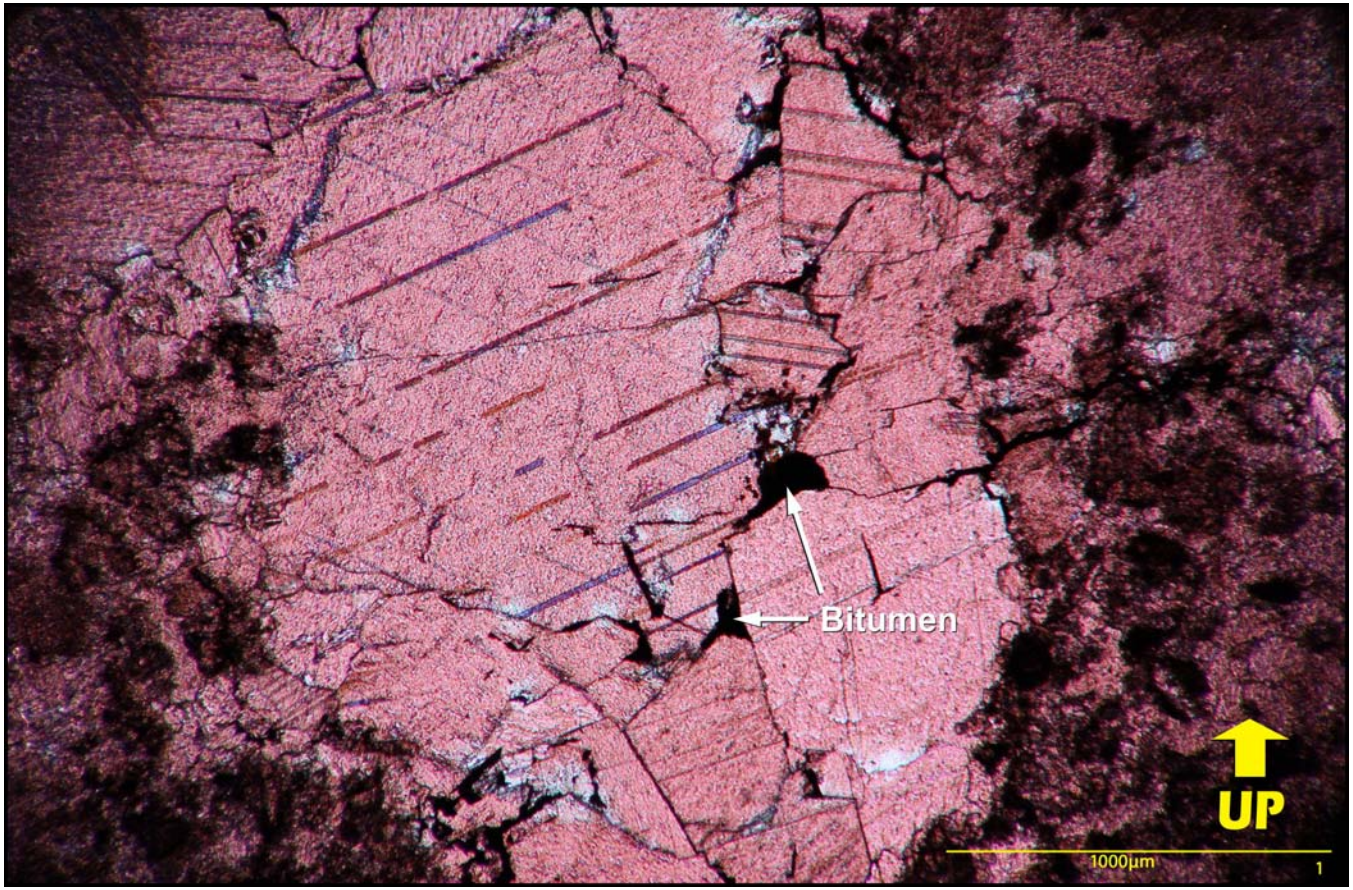

Photomicrograph illustrating the occurrence of bitumen infilling small vugs of dissolution origin within equant calcite cements that infill a fracture. Note that the bitumen-filled vugs occur along calcite crystal contacts. These contacts were preferential pathways of fluid flow. Photomicrograph taken using plane-polarized light. Bent Horn A-57, 11022.79 ft.

Figure A12

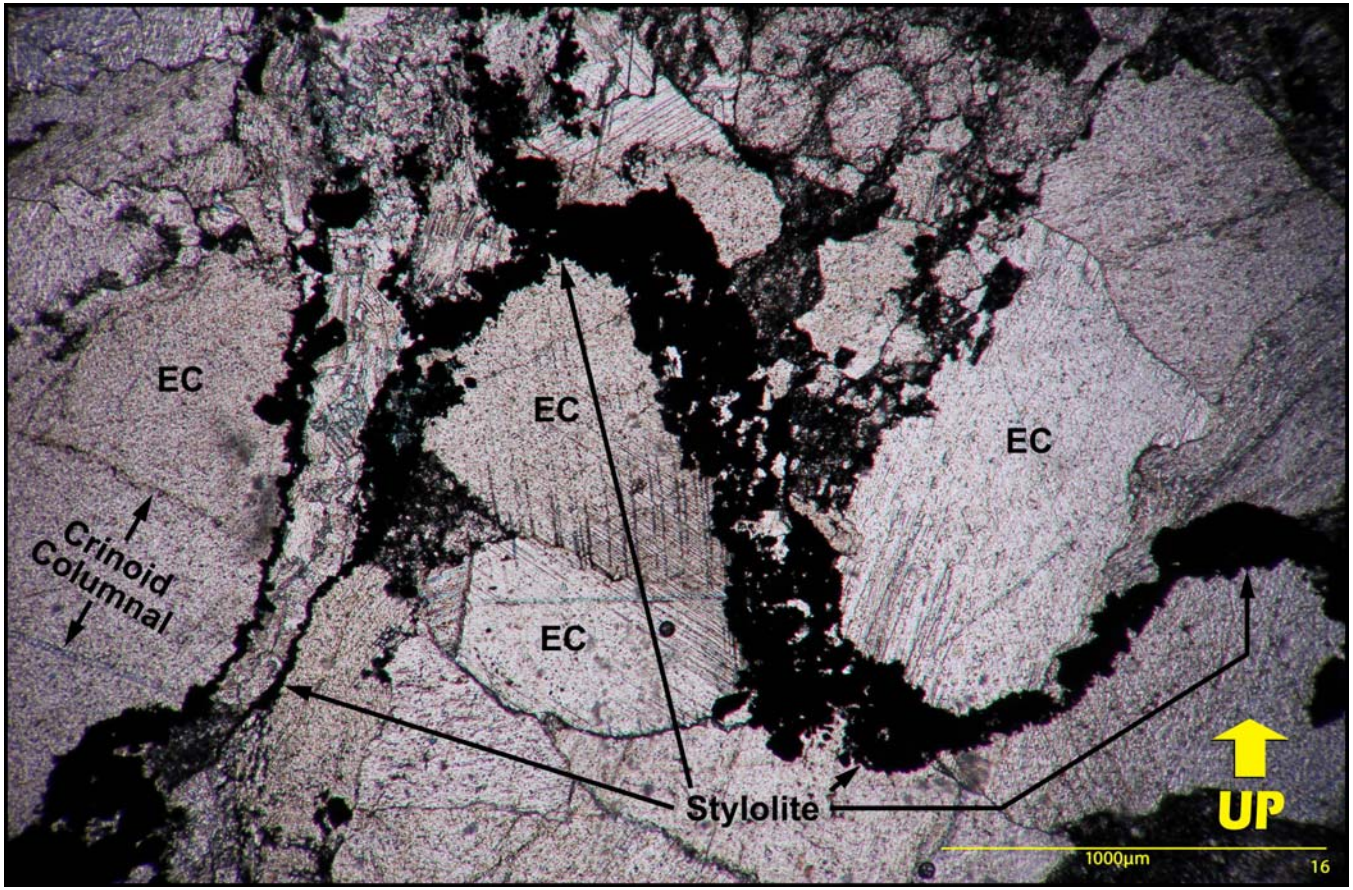

Photomicrograph showing the occurrence of bitumen infilling small vugs of dissolution origin within equant crystals of non-ferroan calcite (EC) adjacent to a horizontal trending stylolite. Photomicrograph taken using plane-polarized light. Bent Horn F-72, 10374.00 ft.

Figure A13

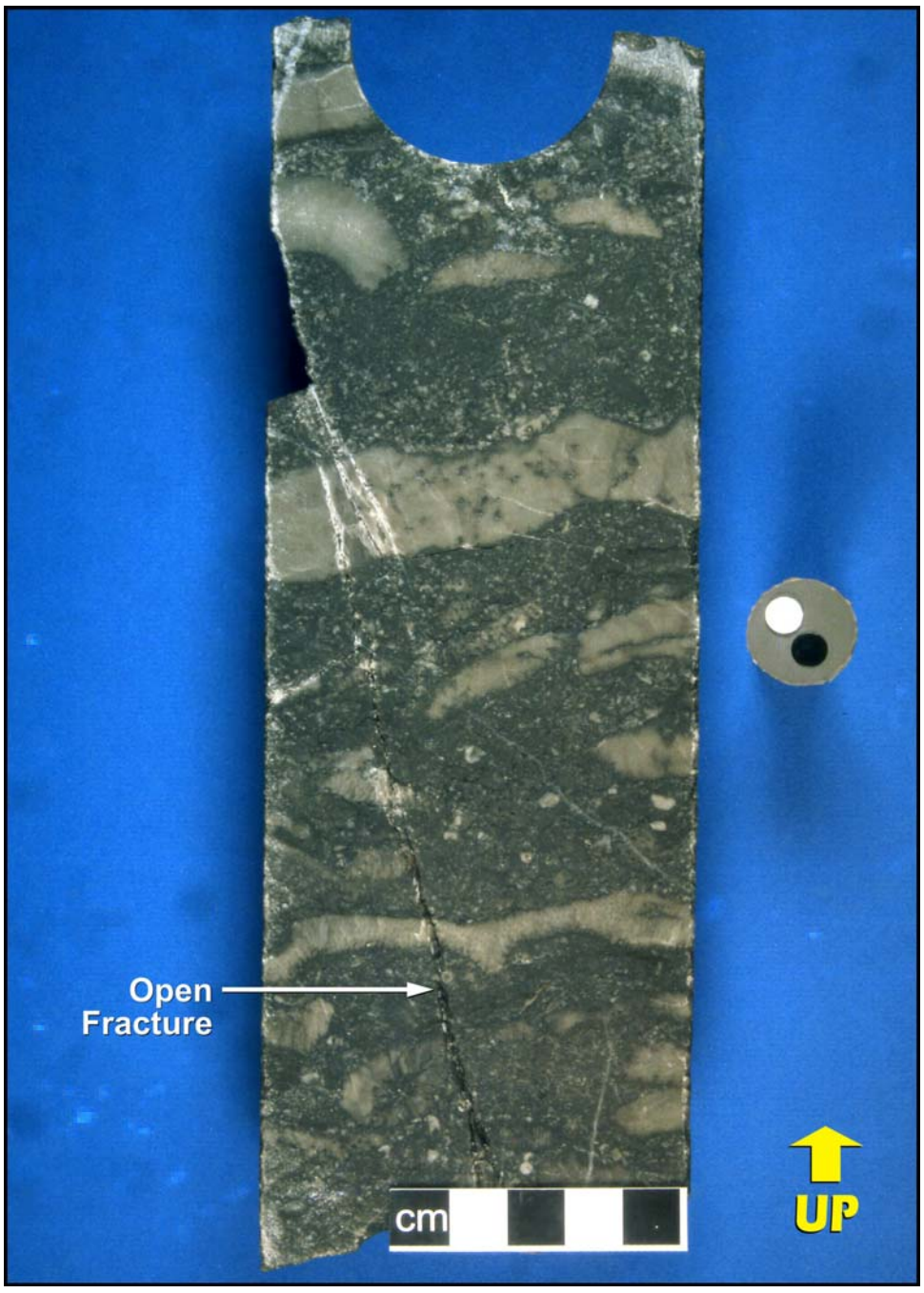

Partially open fracture in foreslope debris consisting of a tabular (tabulate) coral floatstone with a bitumen-bearing peloidal-skeletal grainstone matrix. The Blue Fiord core with this fracture is from the only oil well at Bent Horn capable of sustained production. Photograph taken of a wetted core surface. W. Bent Horn A-02, 9093.00 ft.

Figure A14

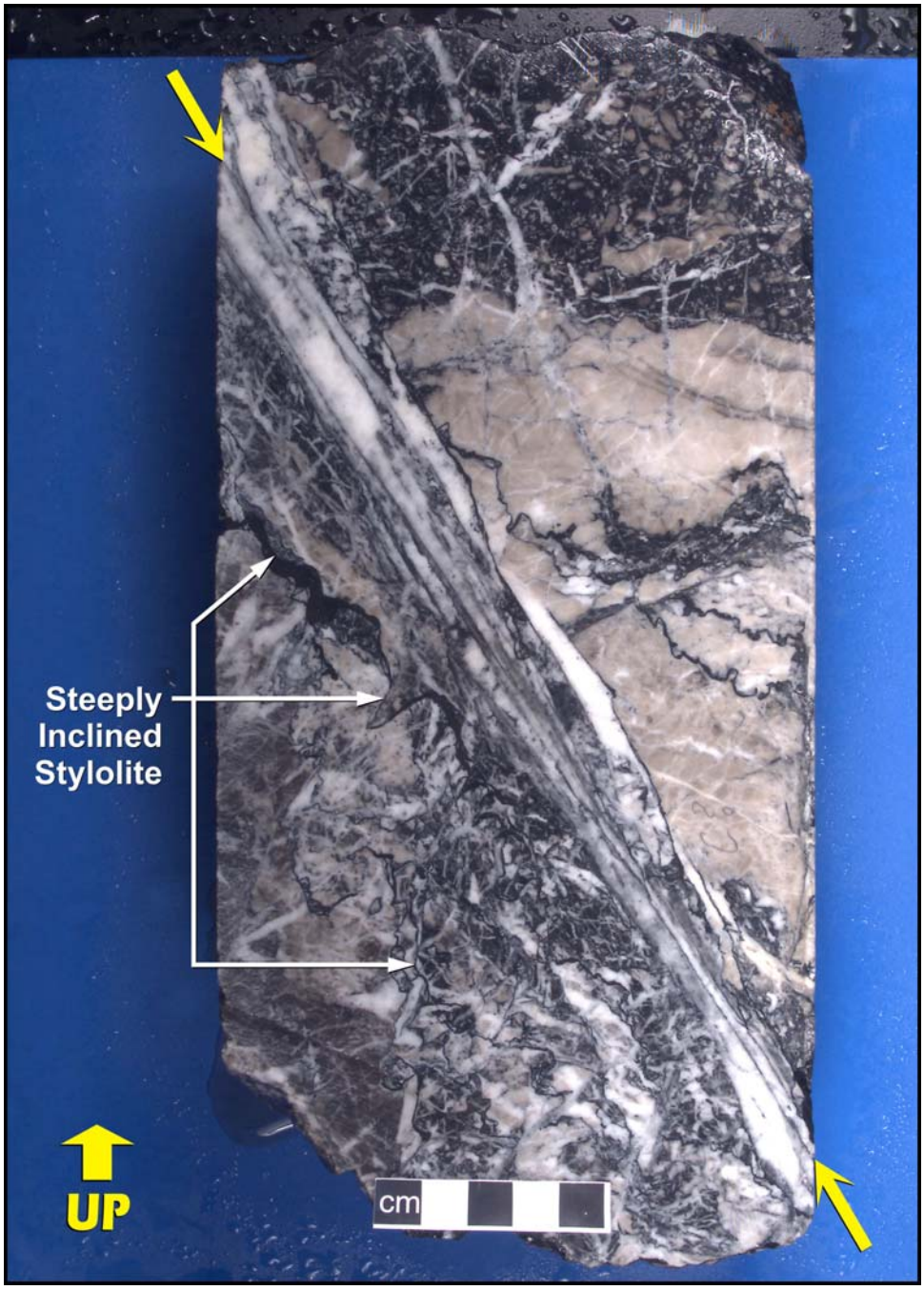

Interpreted thrust fault zone in the Blue Fiord Formation. The zone consists of multiple inclined parallel fractures (arrows), infilled by white equant calcite. Similar calcites infill other fractures, especially in the footwall of the thrust. Note the bitumen-infilled steeply inclined or near-vertical stylolites in the lower left part of the photograph. The presence of steeply inclined and near-vertical stylolites implies horizontal compression and is evidence supportive of thrust faulting. The position of this well lies in close proximity to the traces of thrust faults mapped from seismic by Panarctic Oils Ltd. Photograph taken of a wetted core surface. W. Bent Horn I-01, 10,675.95 ft.

Figure A15

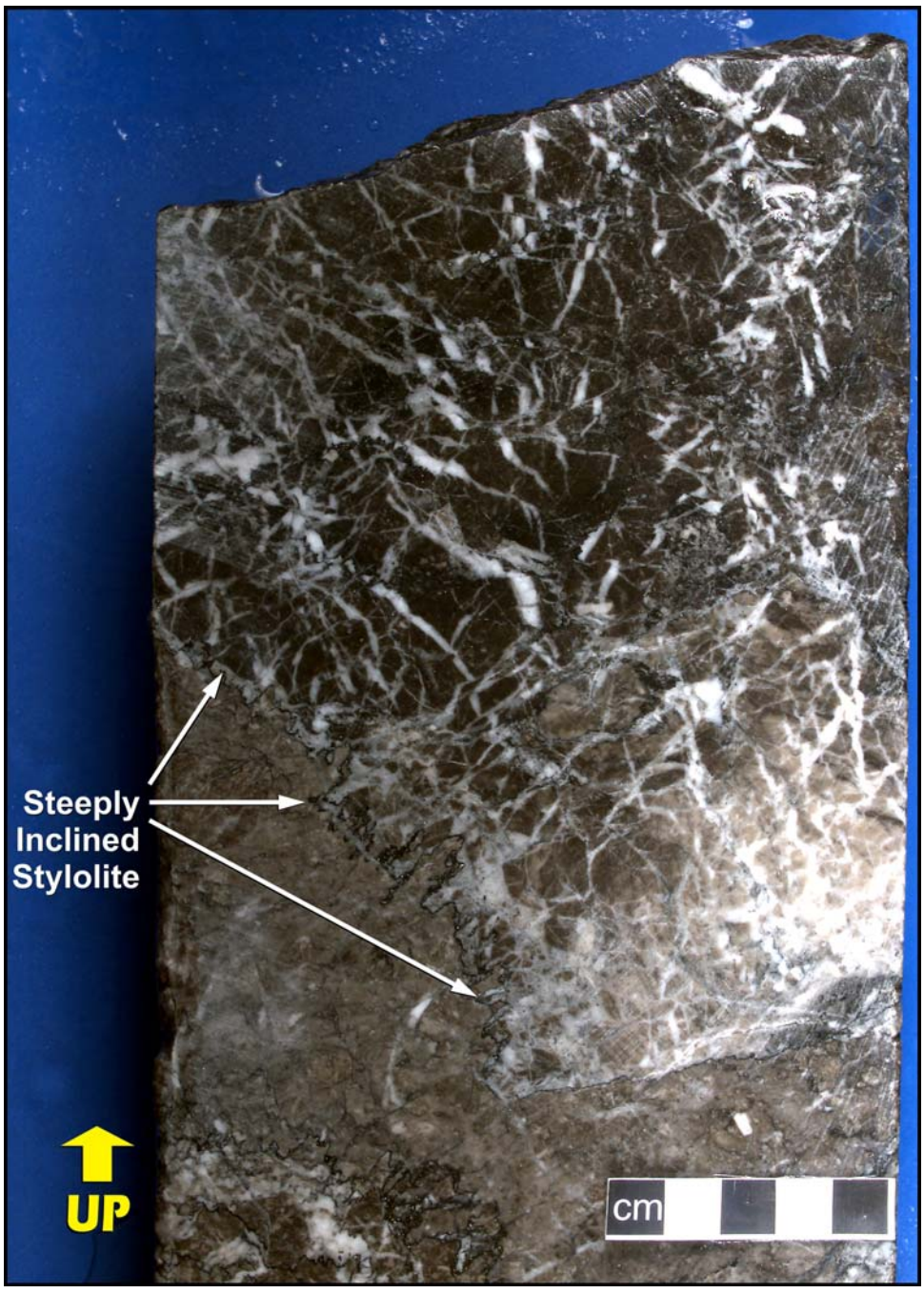

Another interpreted thrust fault in the Blue Fiord Formation, from the same well as the core piece illustrated in Figure A14. In this case, a bitumen-infilled, steeply inclined stylolite marks the trace of the fault. Note the intensive fracture-brecciation of rocks in the hanging wall. These fractures are also infilled by white calcite cement. Photograph taken of a wetted core surface. W. Bent Horn I-01, 10685.45 ft.

Figure A16

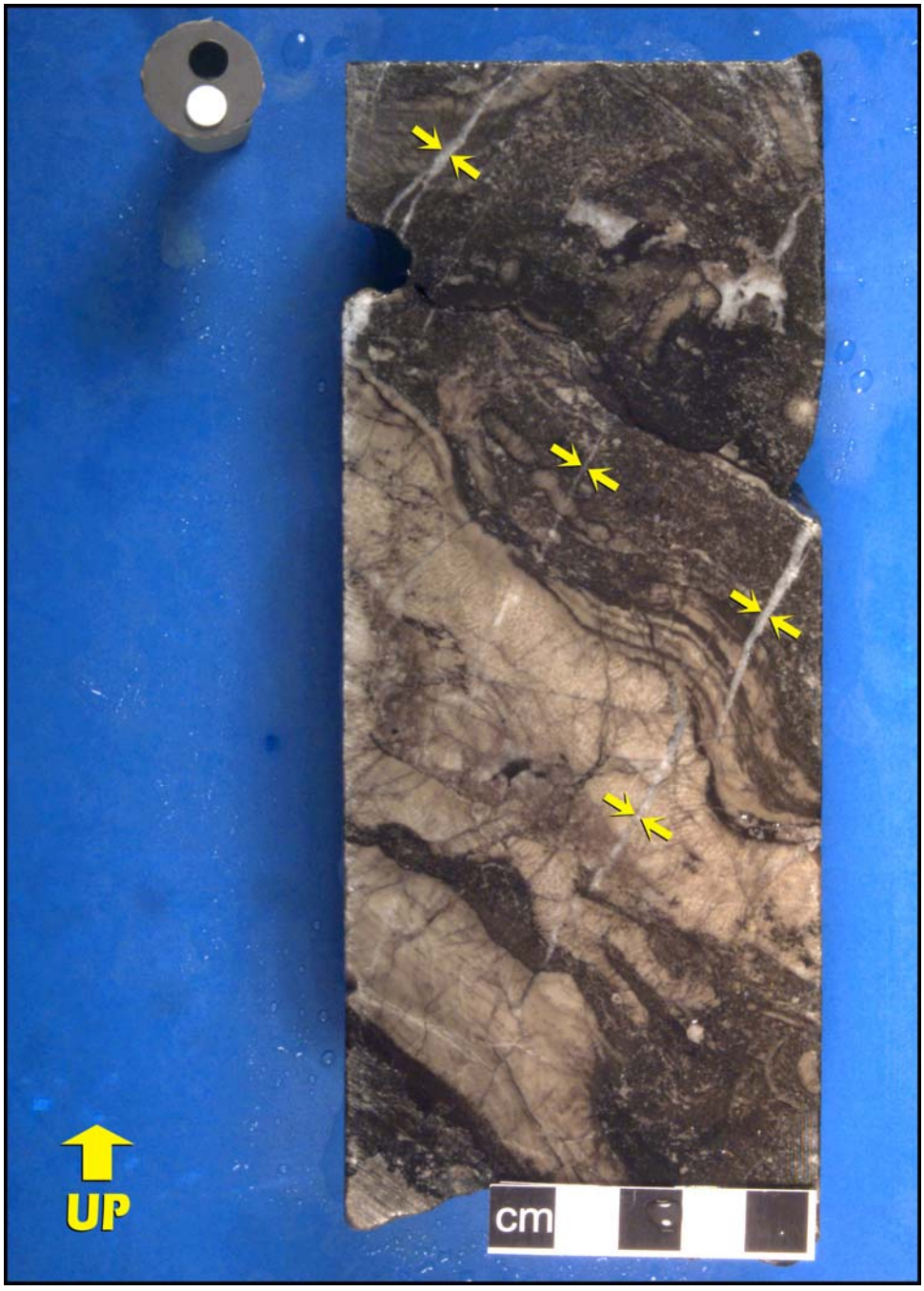

Subparallel, steeply inclined fractures (arrows) infilled by white calcite cement. The fractures are interpreted to be dilational, from the relaxation of compressive forces. Photograph taken of a wetted core surface. W. Bent Horn M-12, 9190.50 ft.

Figure A17

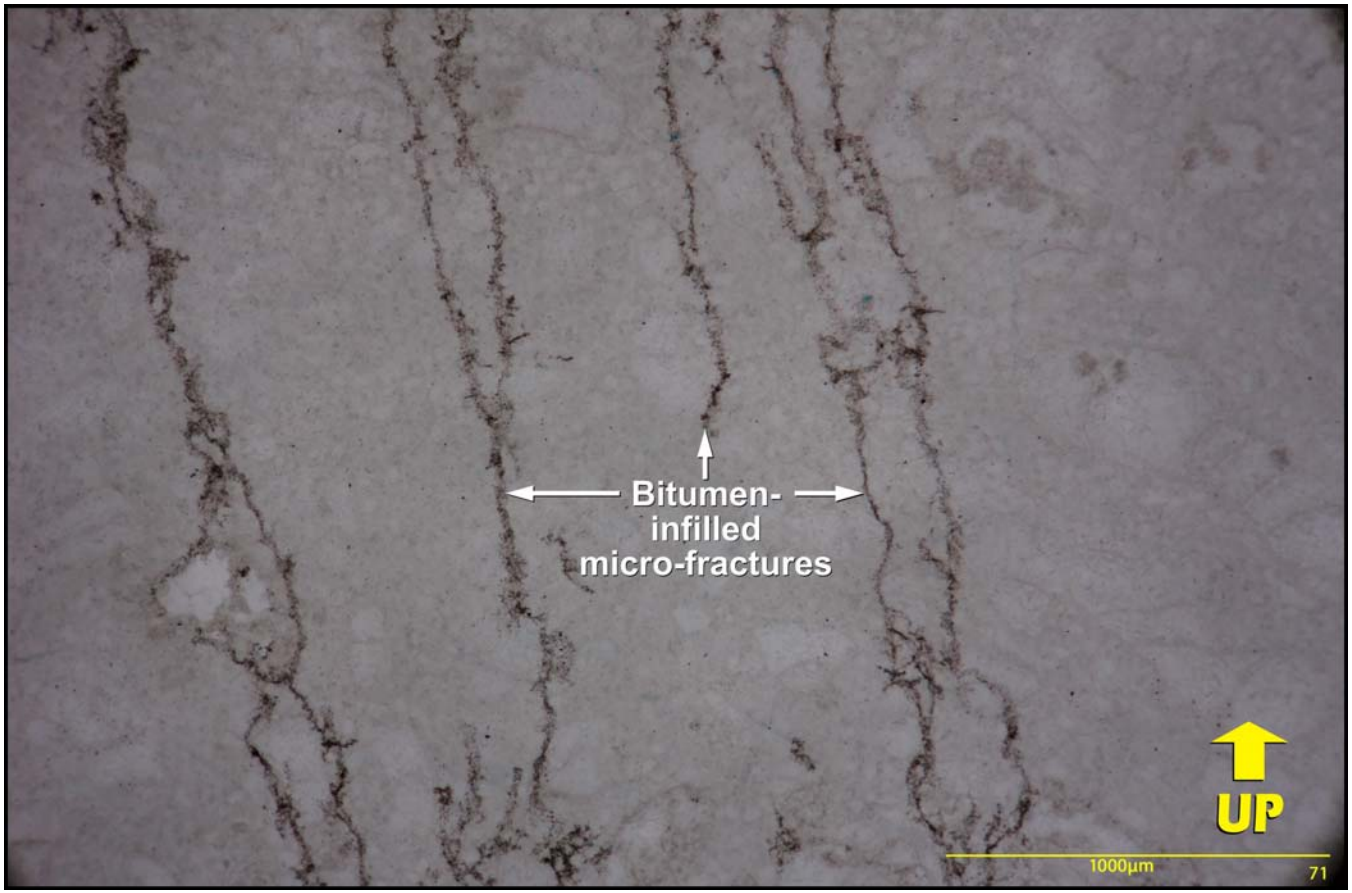

Photomicrograph showing bitumen-infilled, near-vertical micro-fractures cutting a stromatoporoid bioclast and the chamber-filling equant calcite cements. Photomicrograph taken using diffused plane-polarized light. Bent Horn N-72, 10730.10 ft.

Figure A18

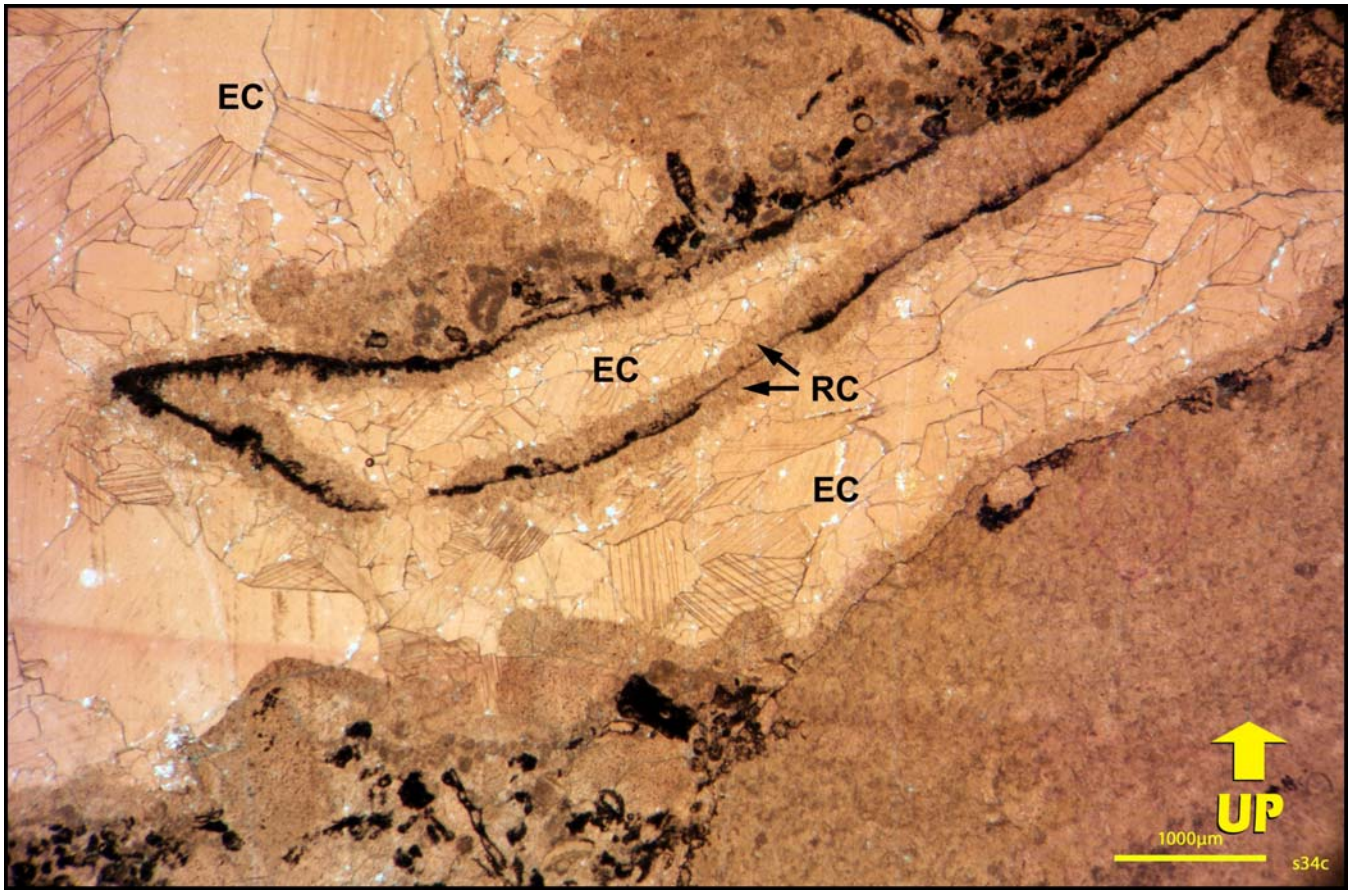

Photomicrograph, taking using a binocular microscope, of radiaxial calcite cement (RC) lining both the interior and exterior walls of a mold of an aragonitic component of uncertain affinity, possibly a valve of a bivalve. The remaining pore space is infilled by equant crystals of non-ferroan calcite (EC). The radiaxial calcite is interpreted to have precipitated from marine waters. The presence of a marine cement within a mold of an aragonitic component implies that dissolution of aragonite, to produce the mold, occurred sufficiently close to the seafloor to be partly infilled by a marine cement. Transmitted plane-polarized light. Cape Fleetwood M-21, 11528.00 ft.

Figure A19

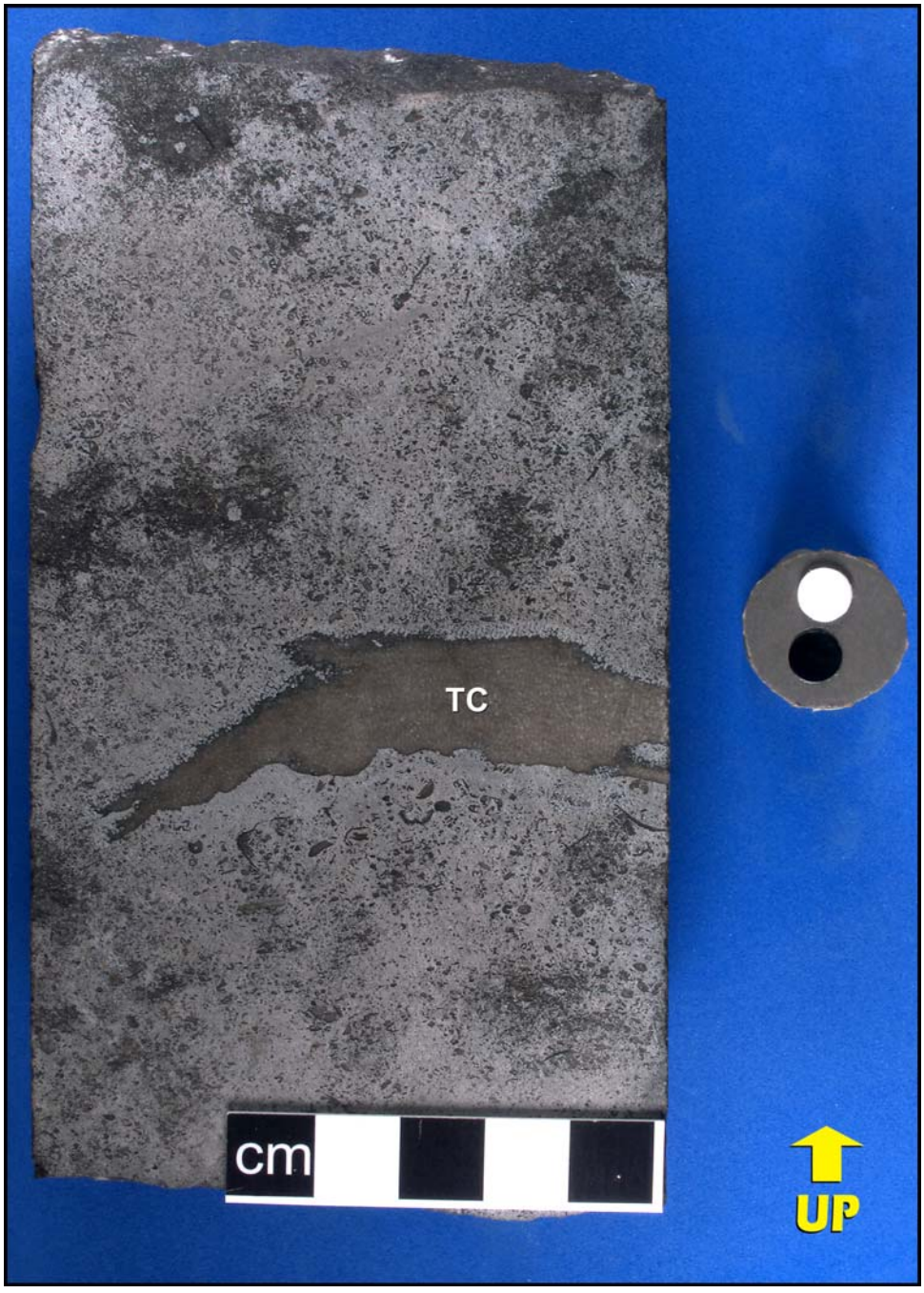

Extensive and selective dolomitization of peloids and micrite in a packstone containing one large tabulate coral bioclast (TC) and numerous finer skeletal particles. The skeletal constituents have not been replaced by dolomite. Photograph taken of a dry core surface. W. Bent Horn E-43, 11023.50 ft

Figure A20

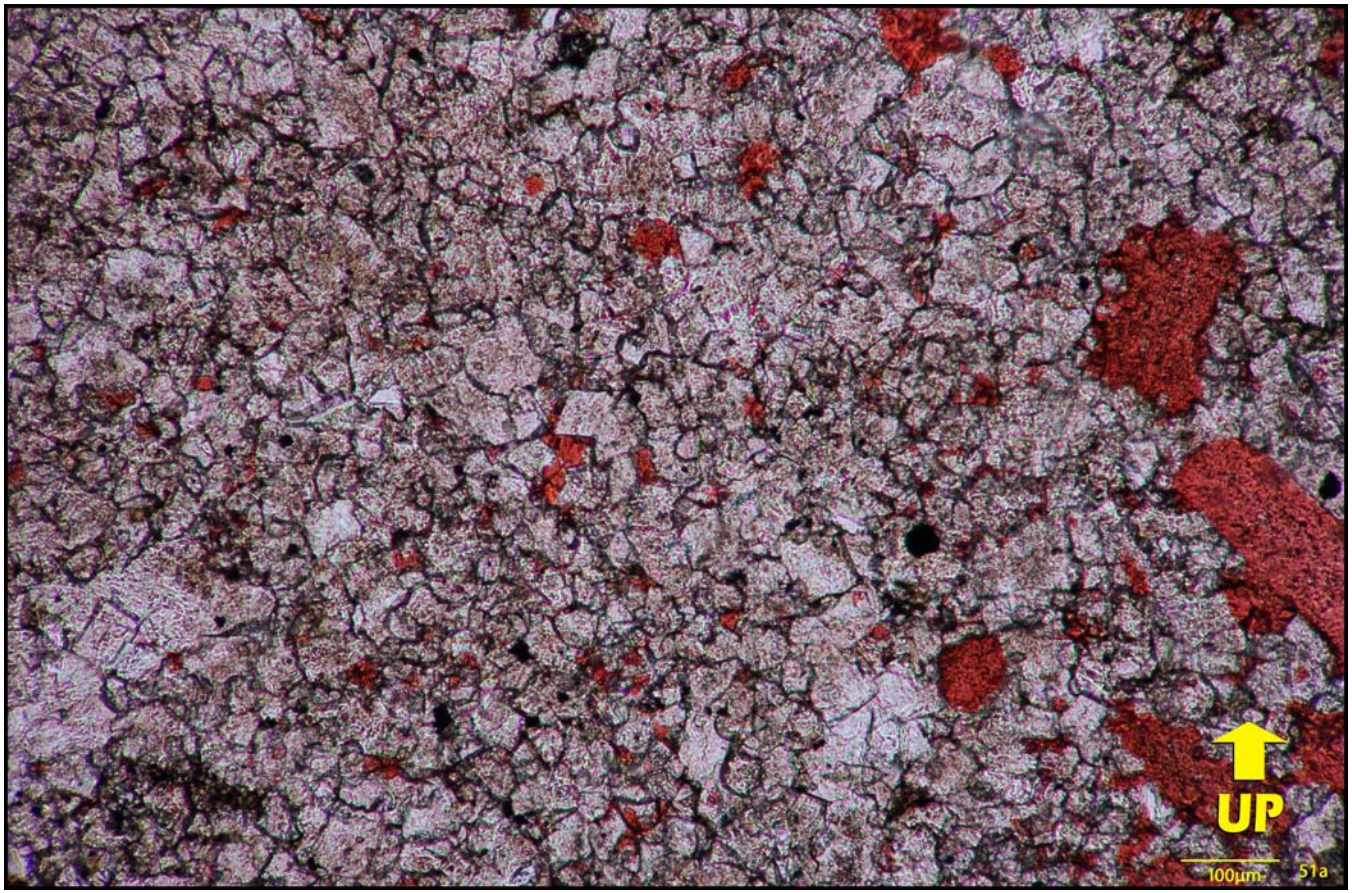

Photomicrograph illustrating an area of extensive dolomitization. Calcitic particles are red, stained by Alizarin Red S. The dolomite has a planar-s texture. Photomicrograph taken using plane-polarized light. W. Bent Horn E-43, 11037.45 ft.

Figure A21

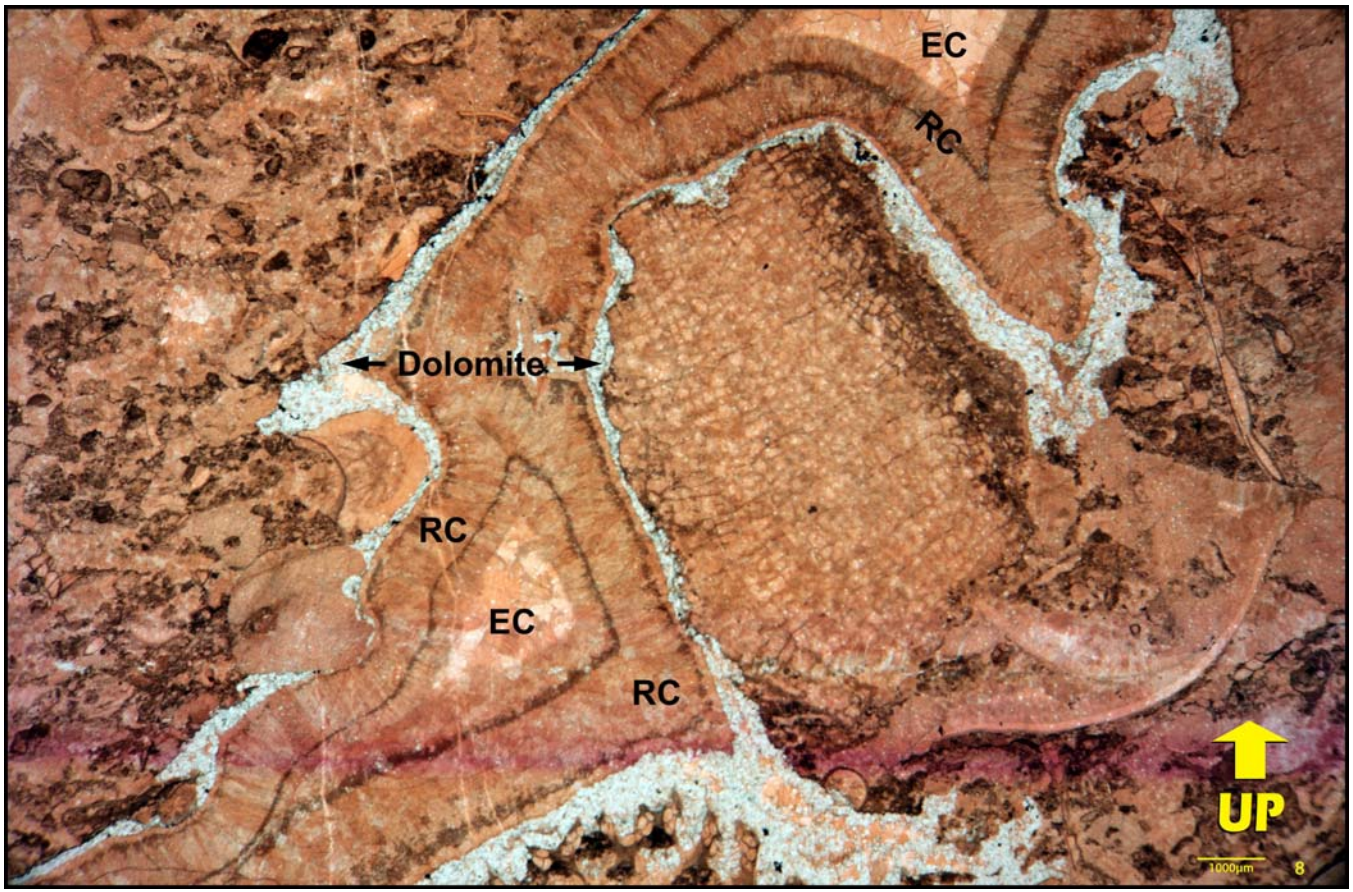

Photomicrograph illustrating dolomite replacing the initial phase of radiaxial calcite cement (RC) that lines a large depositional cavity. The distribution of the dolomite mimics that of an isopachous cement, but the dolomite is in fact replacive. Equant crystals of non-ferroan calcite (EC) infill the remaining pore space of the cavity. Photomicrograph taken using plane-polarized light. Bent Horn F-72, 10409.50 ft.

Figure A22

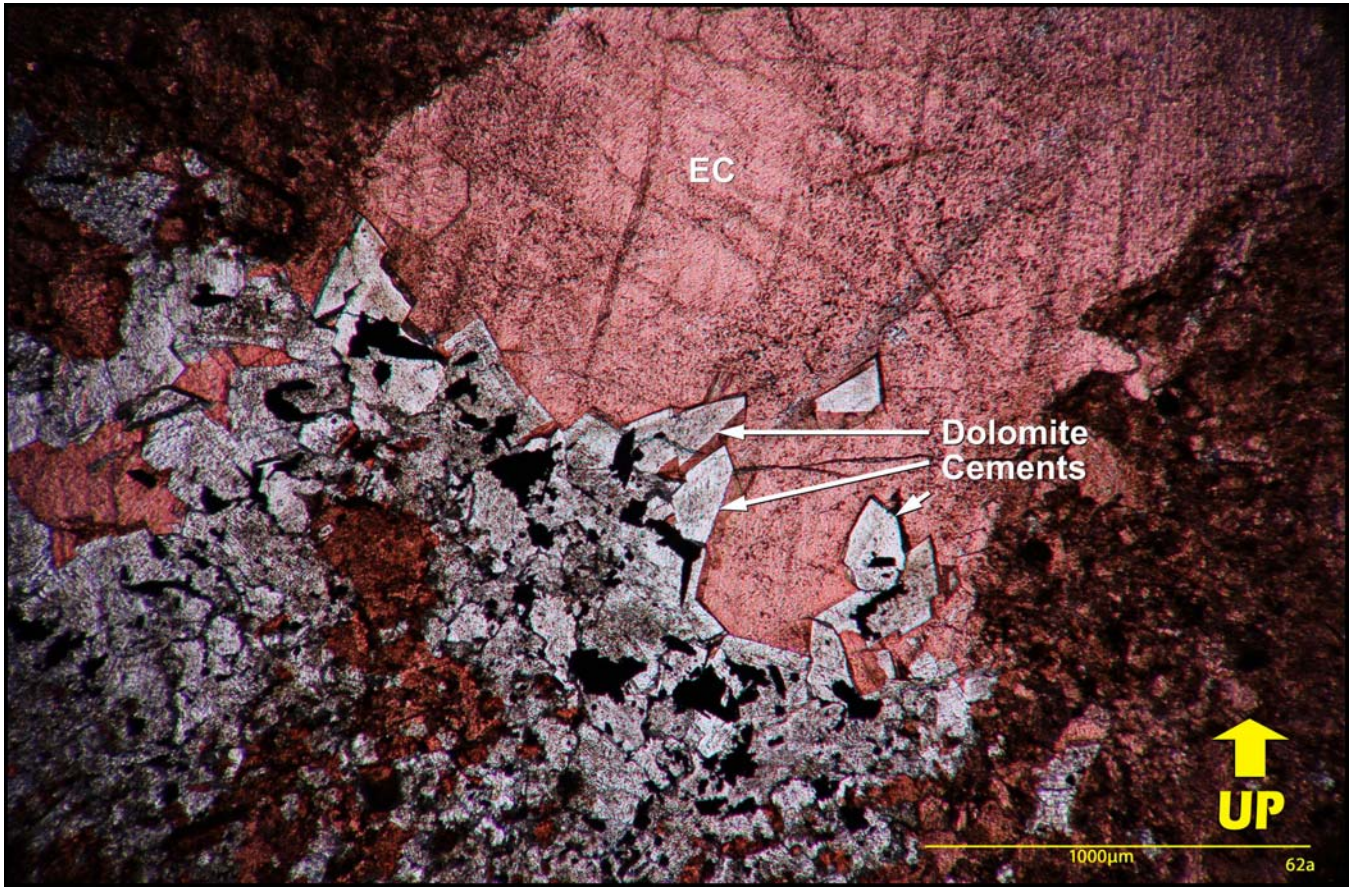

Photomicrograph illustrating the growth of dolomite cement crystals off from replacive dolomite rhombs into a short discontinuous fracture. The dolomite cement crystals have pointed scalenohedral faces that are overgrown by a coarse crystal of non-ferroan calcite (EC) (stained red by Alizarin Red S). Photomicrograph taken using plane-polarized light. W. Bent Horn G-02, 3124.10 m.

Figure A23

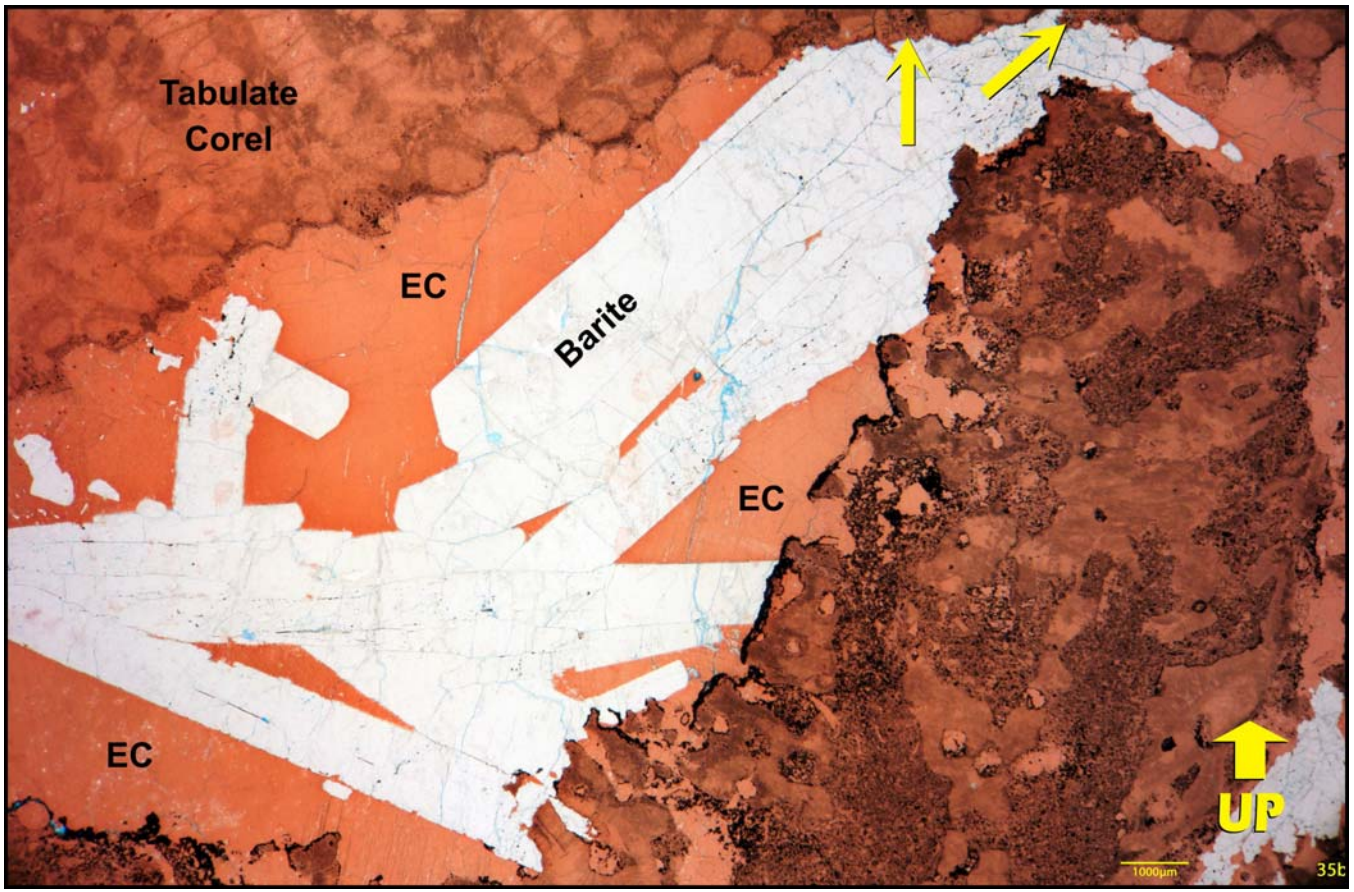

Photomicrograph, taken using a binocular microscope, illustrating tabular crystals of barite in a cavity sheltered by a tabular (tabulate) coral clast. The barite partially replaces fine crystals of non-ferroan calcite infilling the chambers of the coral (arrows in upper right of photograph) and are overgrown by later very coarse crystals of non-ferroan calcite (EC) which infill the remainder of the shelter cavity. Transmitted plane-polarized light. Cape Fleetwood M-21, 10961.25 ft.

Figure A24

Radiating fibrous form of barite crystals infilling fractures in a quartzose very fine sandstone within a thrust slice of the Cape De Bray (?) Formation. Photograph taken of a wetted core surface.
Bent Horn F-72A, 10717.80 ft.

Figure A25

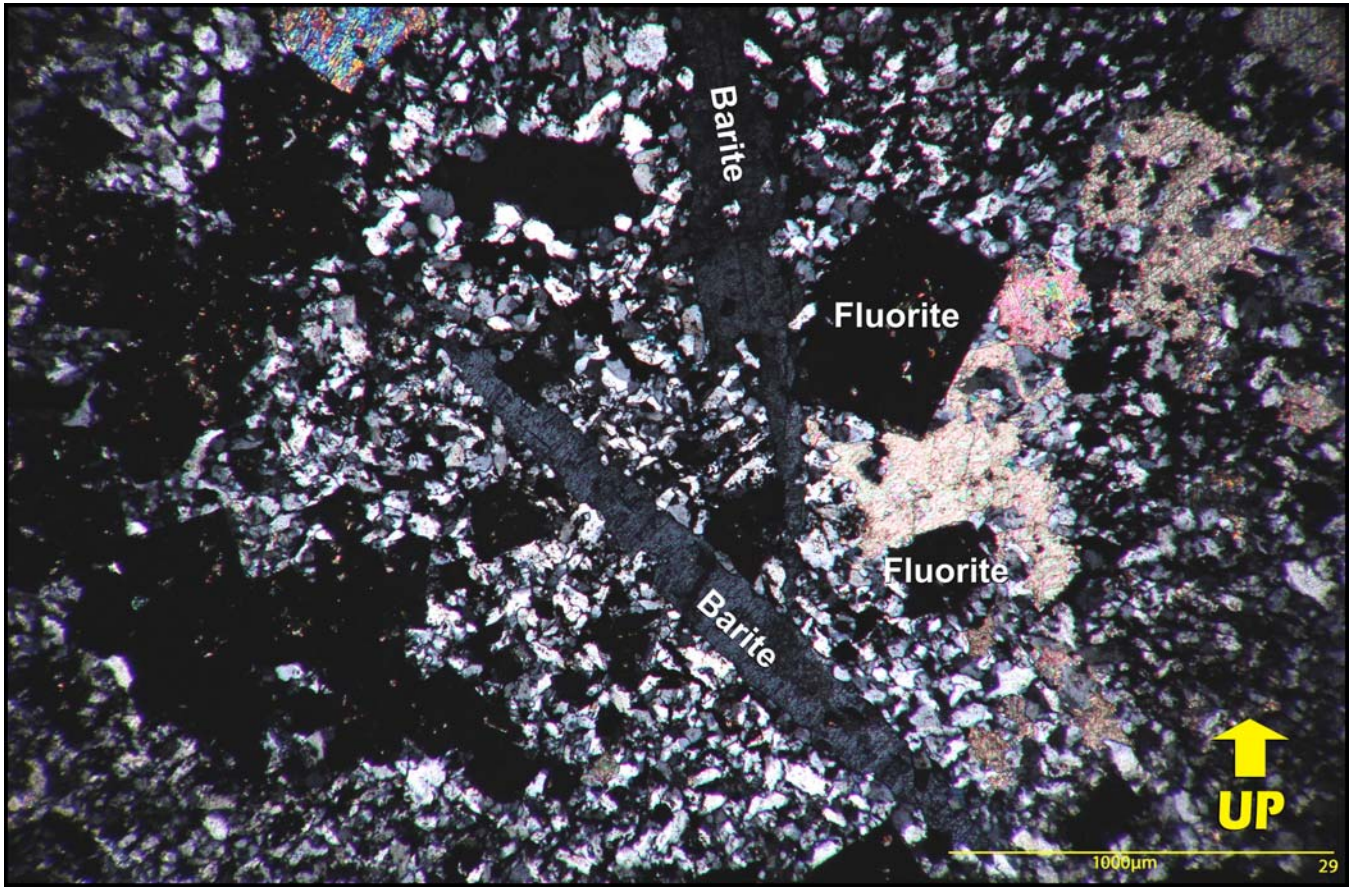

Photomicrograph illustrating the occurrence of fluorite and barite in a very fine quartzose sandstone within a faulted slice of the Cape De Bray (?) Formation. Fluorite occurs as cubic crystals and barite as tabular crystals that overgrow the fluorite crystals. Photomicrograph taken using cross-polarized light. Bent Horn F-72A, 10718.20 ft.

Figure A26

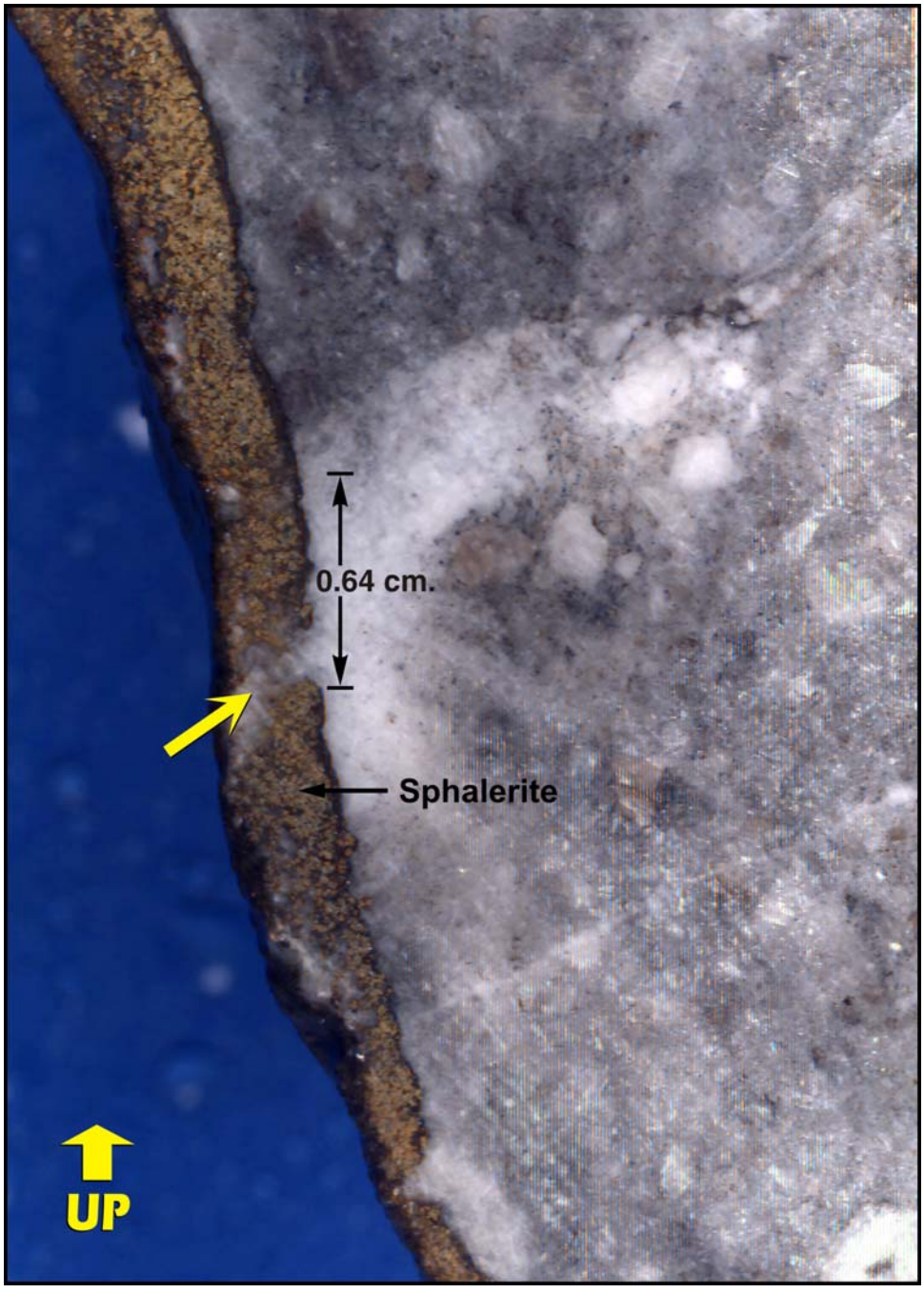

Botryoidal growth of sphalerite lining a fracture that occurs less than 1 ft. above the trace of a trust fault in the Blue Fiord Formation. White calcite also occurs as a thin overgrowth on the sphalerite, infills a short fracture (arrow) cutting the sphalerite and partially replaces the limestone wall rock. Slickensides occur on the backside of this core piece and are indicative of displacement within this zone. Photograph taken of a wetted core surface. Bent Horn I-01A, 10165.85 ft.

Figure A27

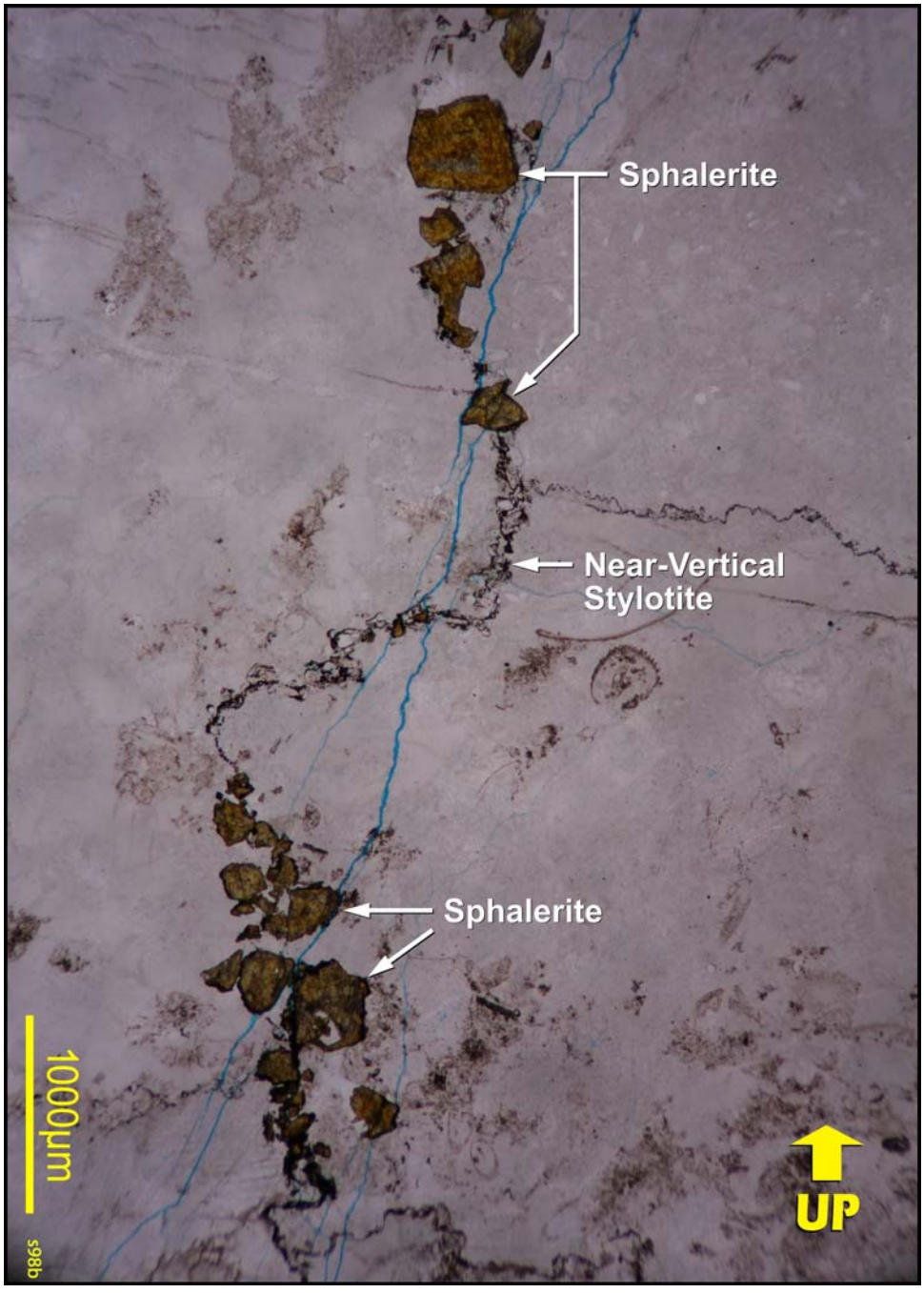

Photomicrograph illustrating anhedral masses of sphalerite occurring along the trace of a bitumen-infilled, near-vertical stylolite. This stylolite occurs 10 ft. below the trace of a thrust fault within the Blue Fiord Formation. Photomicrograph taken using diffused plane-polarized light.
Bent Horn I-01A, 10177.00 ft.

Figure A28

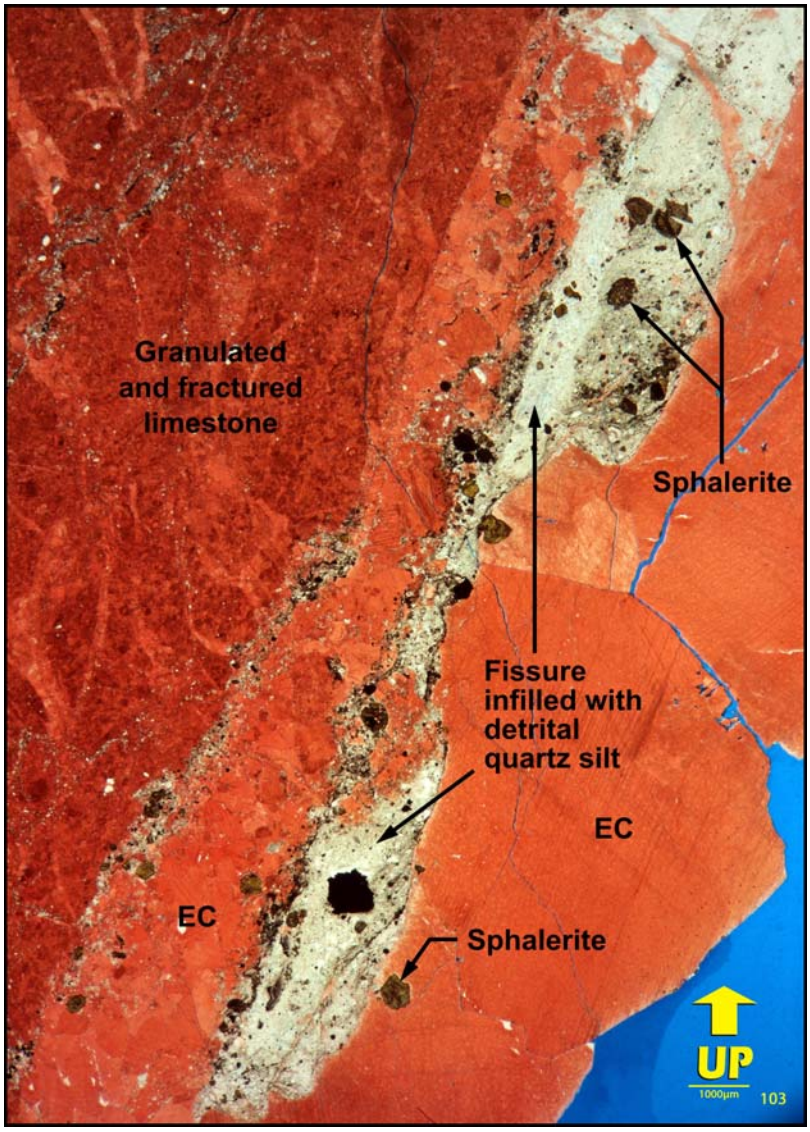

Photomicrograph, taken using a binocular microscope, illustrating the occurrence of anhedral masses of sphalerite within, or adjacent to, a near-vertical fissure infilled with detrital quartz silt. The near-vertical fissure is cut through coarse crystals of non-ferroan calcite (EC) that infill a fracture that is at least 9 mm wide. The adjacent limestone wall rock is extensively granulated and fractured. These narrower fractures are infilled by non-ferroan calcite and also contain both detrital and authigenic quartz. The formation of a near-vertical, open (prior to silt infiltration) fissure implies extension. The infiltration and infilling of the fissure by detrital quartz silt implies that the fissure was open to a level above the top of the Blue Fiord Formation. This rock is interpreted to have undergone two phases of deformation. Firstly, the limestone is interpreted to have undergone a compressional phase of deformation during thrust faulting, as evidenced by the granulation and fracturing of the limestone wall rock. Note that this sample is from a position less than 1 ft. below the trace of the thrust fault within the Blue Fiord Formation, alluded to in the two previous figure captions. Later, the rock is interpreted to have undergone an extensional phase of deformation, culminating in the opening of a near-vertical fissure and the infiltration of quartz silt from an overlying source. The mineralization of sphalerite is interpreted to be from fluids that moved through this fissure during this extensional phase of deformation. Transmitted plane-polarized light.
Bent Horn I-01A, 10167.40 ft.

Figure A29

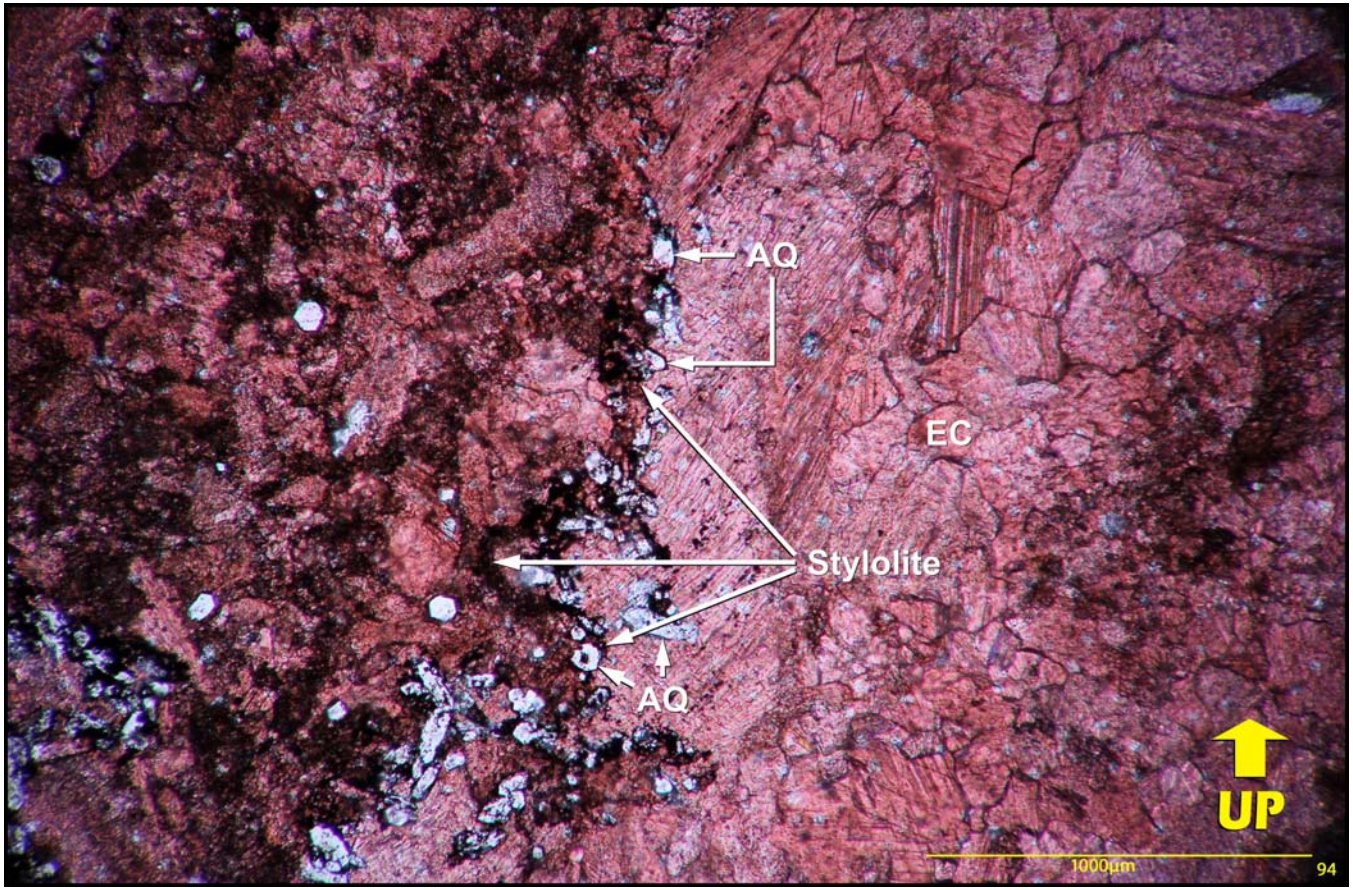

Photomicrograph illustrating the occurrence of authigenic quartz crystals (AQ) along the trace of a near-vertical stylolite, at the contact between the limestone wall rock and the equant crystals of non-ferroan calcite (EC) infilling a steeply inclined fracture. The equant calcite cement is intensively deformed, as evident by its brecciation and deformation of the twin lamellae. Photomicrograph taken using plane-polarized light. Bent Horn I-01A, 10203.50 ft.

Figure A30

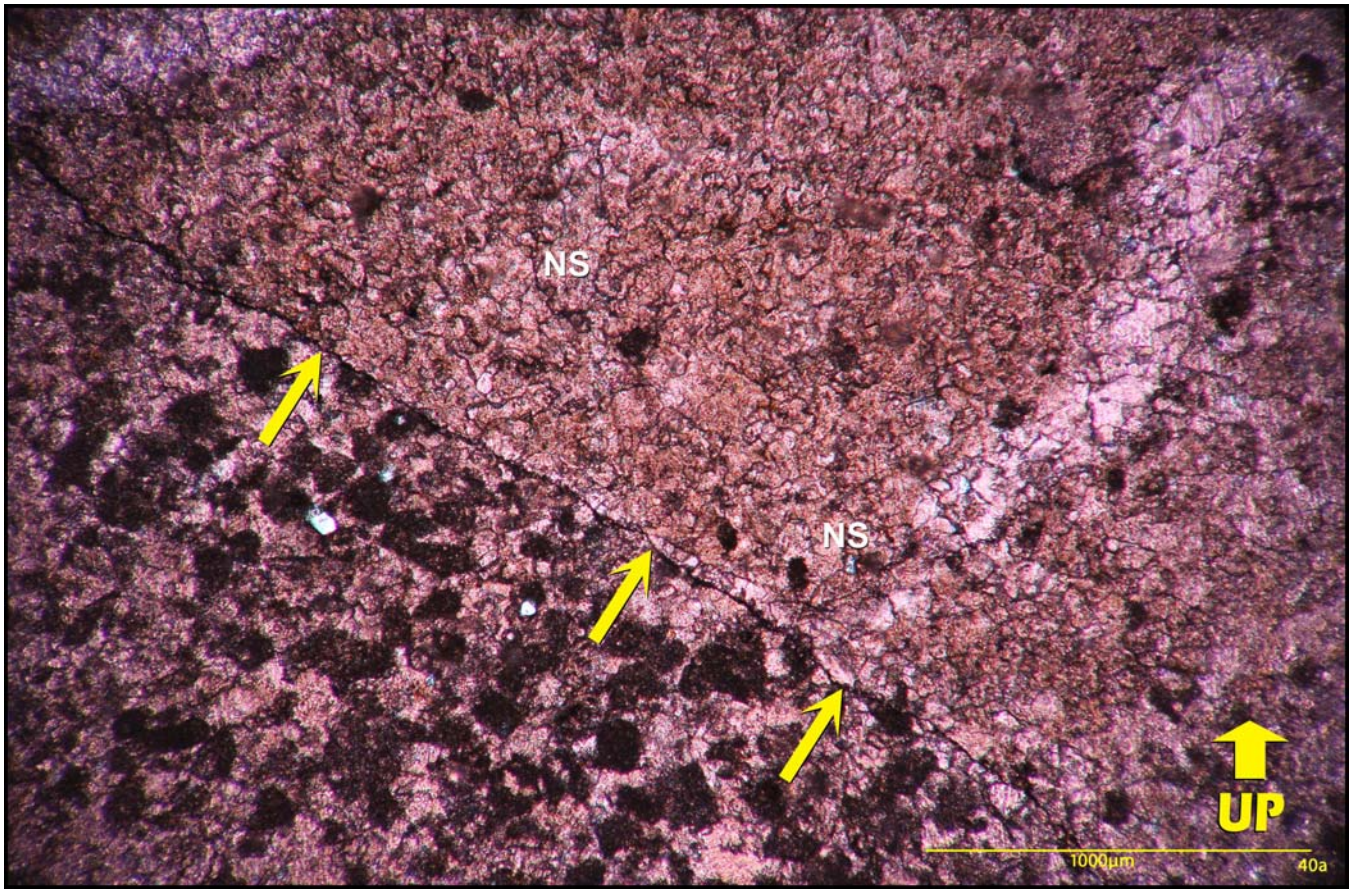

Photomicrograph showing the selective occurrence of neomorphic spar (NS) in the hanging wall of an interpreted micro-scale thrust fault. The parent limestone is a peloidal packstone. The abrupt contact (arrows) at the base of the neomorphic spar suggests that the contact is a fault. The identification of the fault as a thrust is based on the presence of a diagonally-trending stylolite elsewhere in the thin section, striking approximately perpendicular to the trace of the fault, consistent with displacement during compression. The depositional texture of the host limestone in the hanging wall has been obliterated by neomorphism but is still intact in the foot wall. Photomicrograph taken using plane-polarized light. W. Bent Horn A-02, 9132.90 ft.

Figure A31

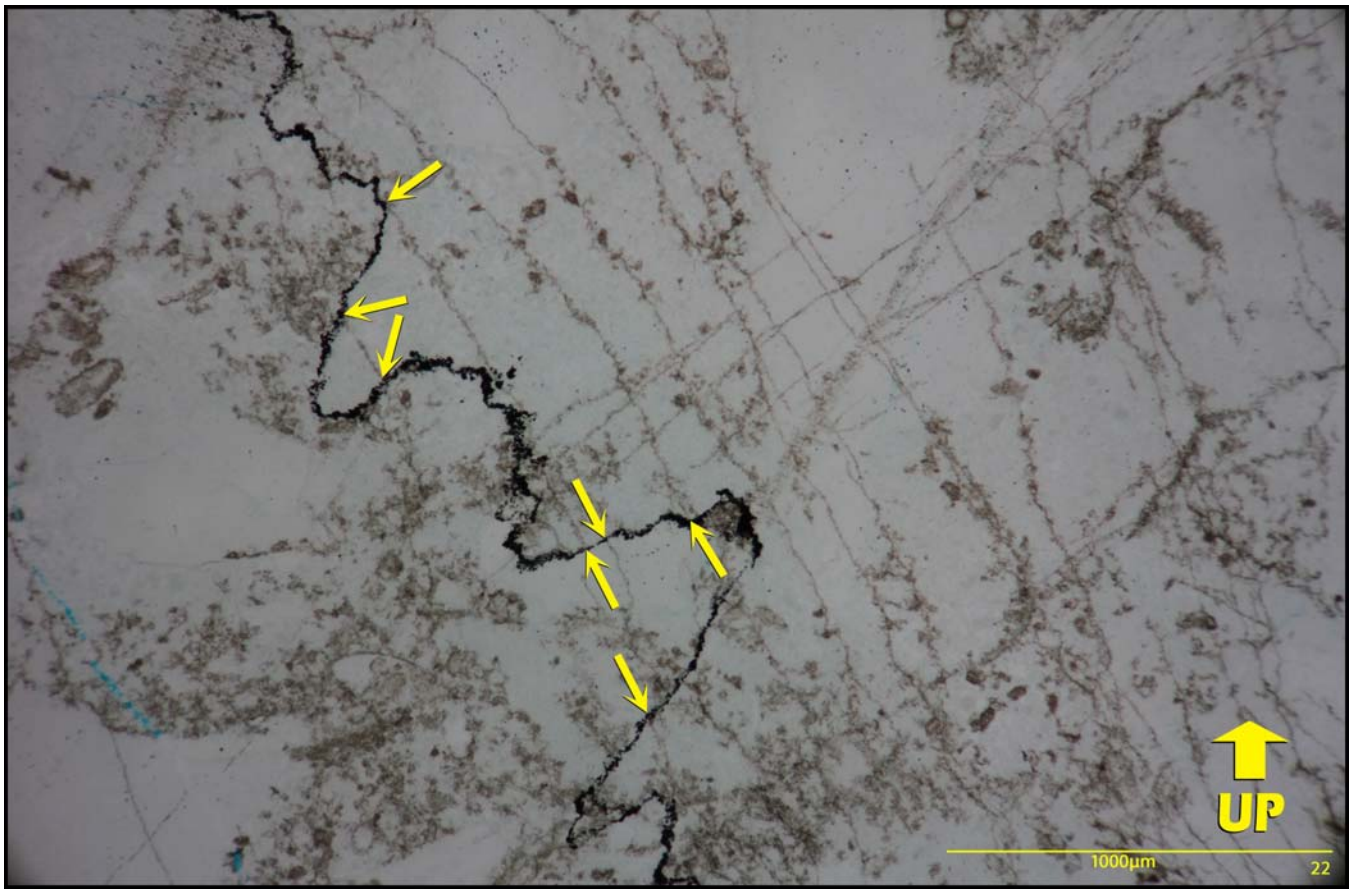

Photomicrograph showing the truncation of hairline micro-fractures along a bitumen-infilled, steeply inclined stylolite (arrows). Thus, the last phase of compression during stylolite formation followed that of the formation of the micro-fractures. Therefore, the formation of these micro-fractures is attributed to the preceding part of the phase of thrust faulting. Photomicrograph taken using diffused plane-polarized light. Bent Horn F-72, 10320.33 ft.

Figure A32

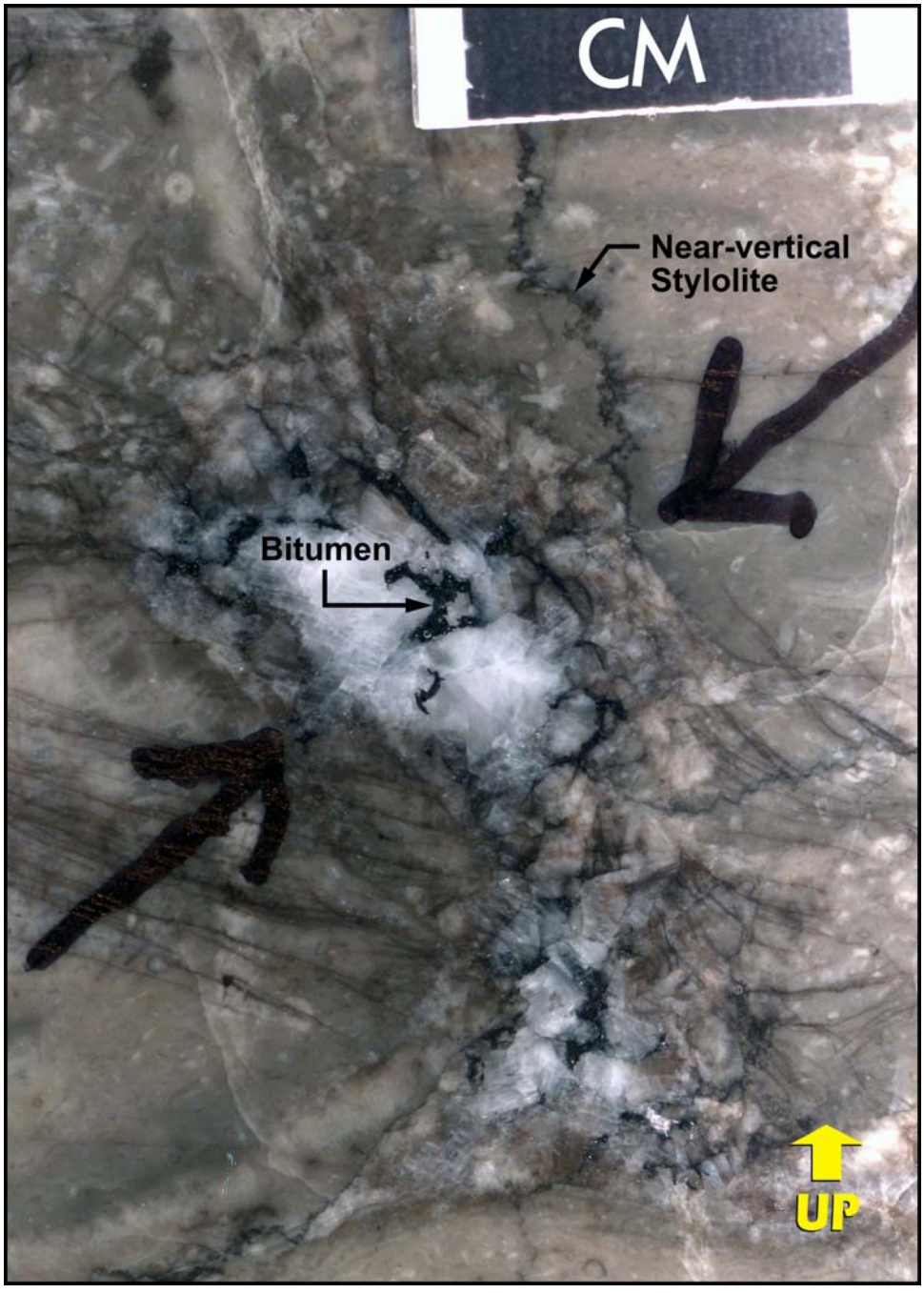

Bitumen overgrowing very coarse white calcite crystals in an irregular fracture. Also note the bitumen-infilled near-vertical stylolite, indicative of compression. Photograph taken of a wetted core surface. Bent Horn A-57, 10989.00 ft.

SECTION B: SUMMARY OF CORES AND THIN SECTIONS OF THE BLUE FIORD FORMATION FROM MELVILLE AND VANIER ISLANDS

This section summarizes the Blue Fiord Formation from cores and thin sections taken from wells on Melville and Vanier Islands. This includes cores from two wells on Melville Island, Richardson Point G-12, and King Point West B-53, and core from one well on Vanier Island, Key Point O-51. Both wells on Melville Island penetrate limestones that are interpreted to be an extension of the Bent Horn isolated reef complex on Cameron Island. The well on Vanier Island penetrates limestones that are interpreted either to be an extension of the Bent Horn isolated reef complex on Cameron Island or from another isolated reef complex.

The depositional facies encountered in cores from these three wells are similar to those described from Cameron Island. All lithofacies in these cores are interpreted to have been deposited on a reefal foreslope. These lithofacies include both tabulate coral and stromatoporoid dominated rudstones and floatstone debris (Figures B1 and B2), branching dendroid tabulate coral rudstones (Figure B3), laminar coral-bearing rudstones and floatstones (Figure B4) and peloidal foreslope sands (grainstones and packstones) (Figure B5).

The limestones in cores from these three wells have undergone a similar diagenetic evolution as those limestones of the Blue Fiord Formation on Cameron Island, albeit different in one key aspect. The dominant diagenetic process was the precipitation of equant non-ferroan calcite, infilling all the primary pores and aragonic mollusc molds (Figure B6). Replacive dolomite occurs only in minor concentrations (Figure B7). Barite occurs in even lower concentrations. Micropores and small vugs, both of dissolution origin, are present (Figure B8), but most are infilled by bitumen (Figure B9). Bitumen also infills micro-fractures cutting tabulate coral bioclasts (Figure B10). As a result of the precipitation of equant calcite cement and the plugging by bitumen, limestones in cores from these three wells have measured porosities of one percent or less and K_{max}'s less than 0.01 mD, similar to limestones of the Blue Fiord Formation on Cameron Island (refer to Appendix).

The one notable difference between the cores from these three wells and the cores of the Blue Fiord Formation on Cameron Island is the paucity of compressional (vertical or steeply inclined) stylolites and the total absence of a granulated matrix. Compressional stylolites were only noted from one occurrence in both core and a thin section of a core sample from the King Point West B-53 well. A granulated matrix was not observed in any of the thin sections. This reflects much less compressional tectonics (thrusting) in these locations than on the southern coast of Cameron Island.

Also, oil staining was not apparent in the core from the King Point West B-53 well, even though bitumen was present in low concentrations. The reason for the apparent lack of oil staining is not known. In addition, neither sphalerite nor fluorite were noted from either the cores, or from thin sections taken from these cores, from the three wells on Melville and Vanier Islands.

Figure B1

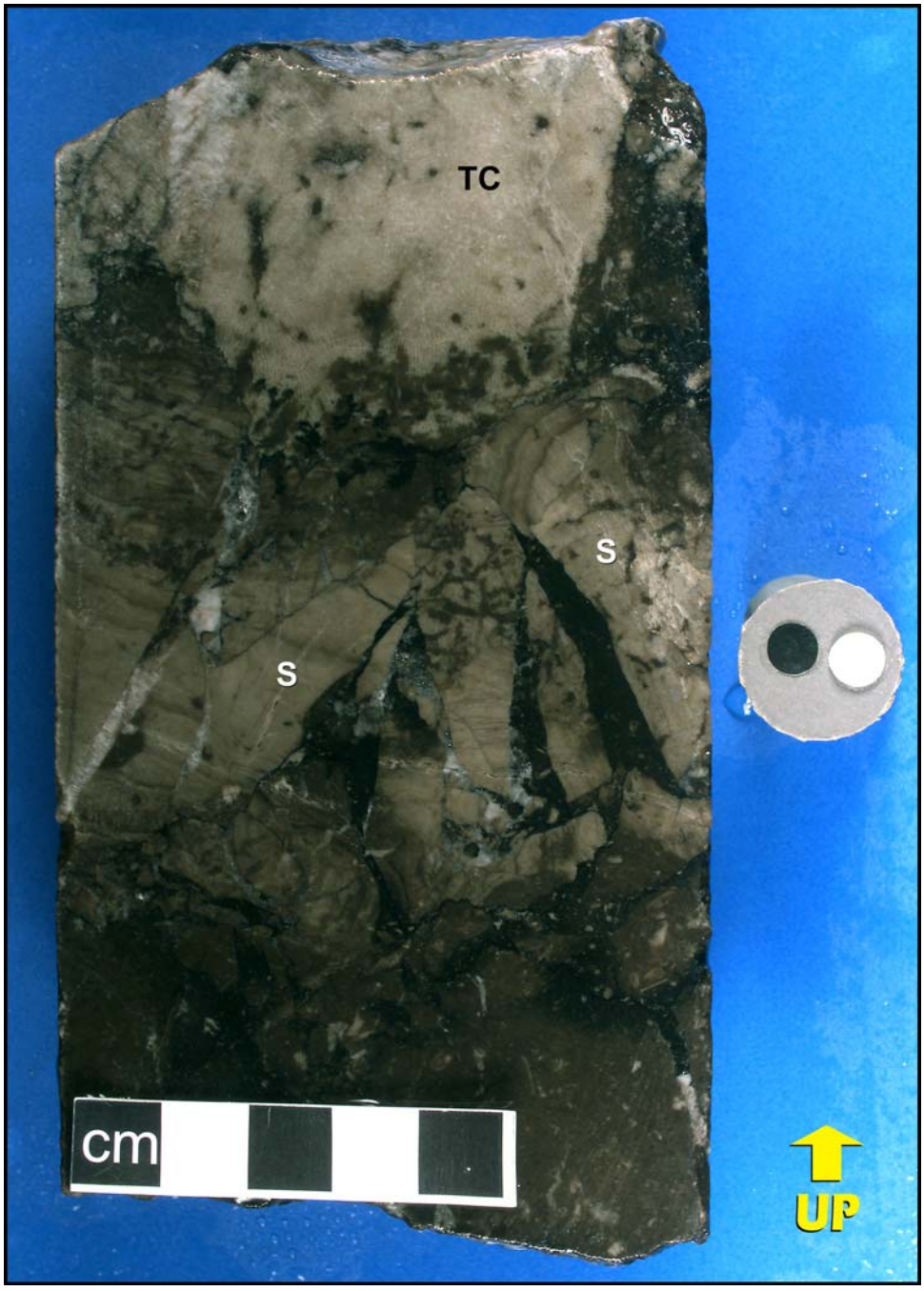

Rudstone/floatstone containing large clasts of massive tabulate corals (TC) and stromatoporoids (S). Bitumen occurs within micropores of dissolution origin in the skeletal-peloidal packstone matrix. Photograph taken of a wetted core surface. Foreslope debris facies, Key Point O-51, 7364.46 ft.

Figure B2

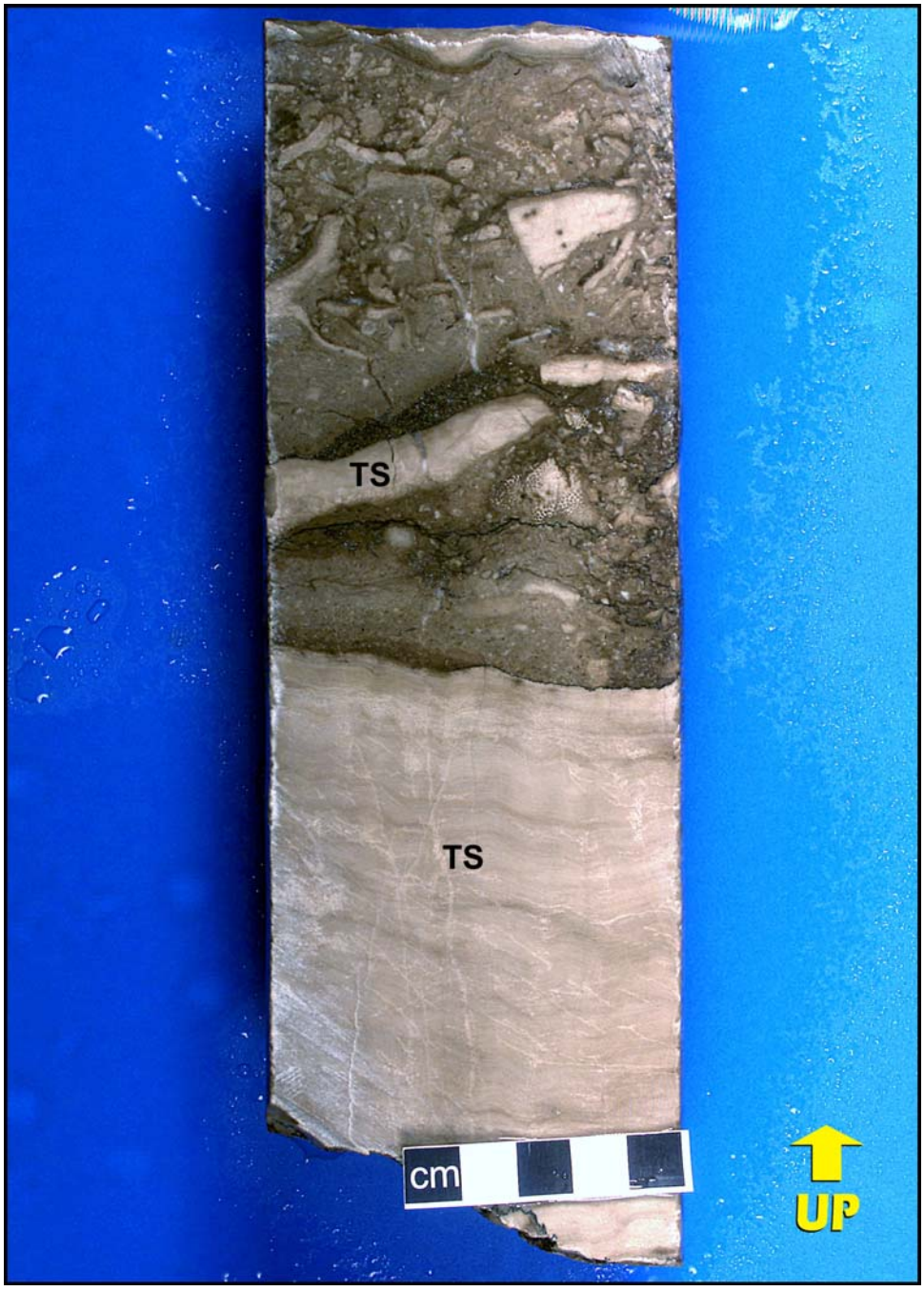

Floatstone containing clasts of both thick and thin tabular stromatoporoids (TS) in 1.5-foot-thick debris bed within a finer foreslope sand succession. The matrix is predominantly a light brown wackestone. Photograph taken of a wetted core surface. Foreslope debris facies, King Point West B-53, 3615.10 ft.

Figure B3

Rudstone containing abundant branches of dendroid tabulate corals and a bitumen-bearing skeletal-peloidal packstone matrix. Photograph taken of a wetted core surface. Branching tabulate coral facies, Key Point O-51, 7393.00 ft.

Figure B4

Laminar coral (LC)-bearing floatstone with a medium grayish brown, pyritic mottled, lime wackestone matrix. Photograph taken of a wetted core surface. Laminar coral facies, Richardson Point G-12, 7949.50 ft.

Figure B5

Medium to dark brown peloidal packstone containing crinoid columnals and molluscan debris. Photograph taken of a wetted core surface. Foreslope sand facies, King Point West B-53, 3618.90 ft.

Figure B6

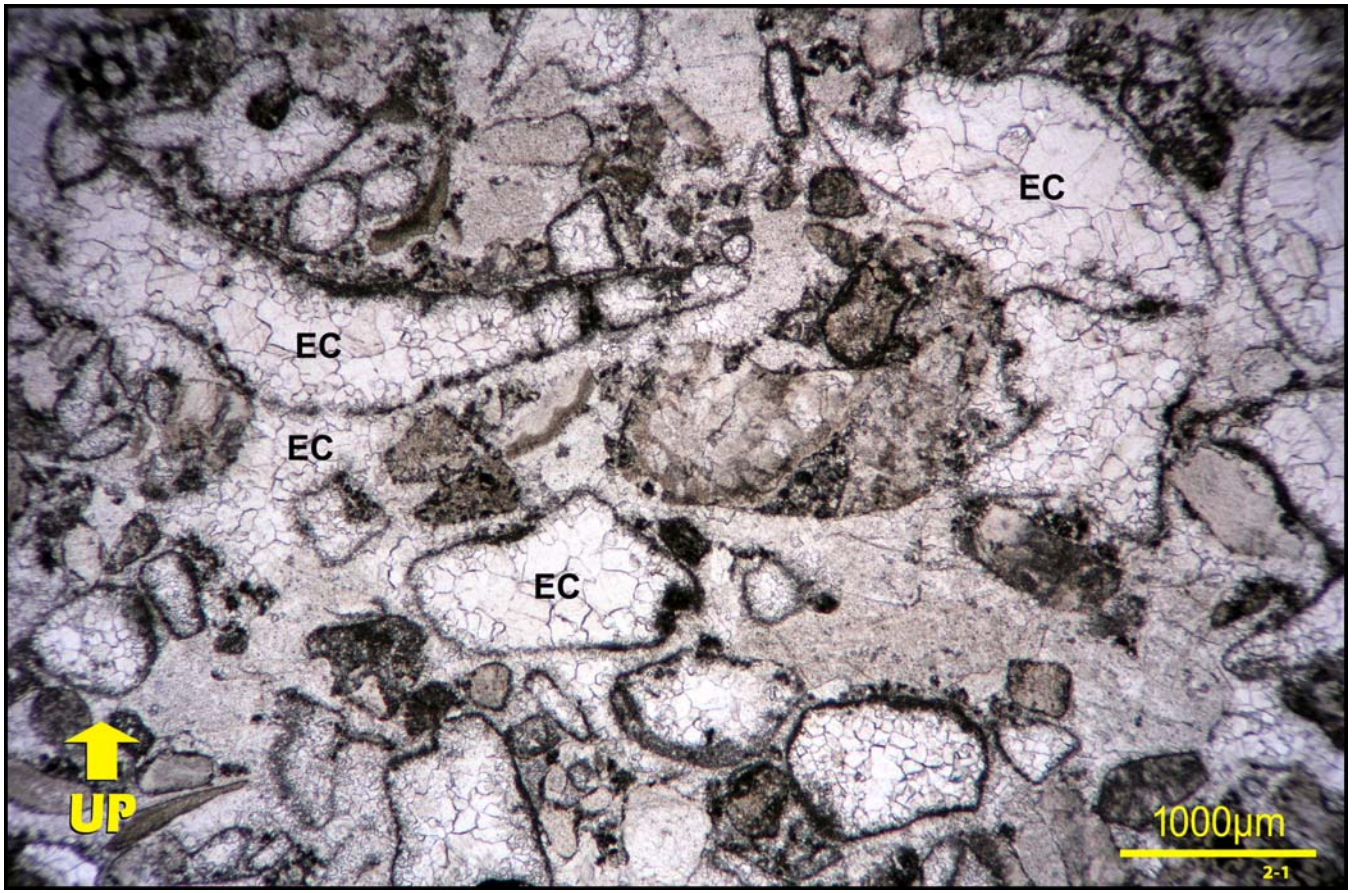

Skeletal lime grainstone with abundant mollusc particles rimmed by micritic envelopes. Equant crystals of non-ferroan calcite (EC) have completely infilled the mollusc molds, formed by the dissolution of the original aragonite, as well as all the interparticle pores. This has reduced the measured porosity to a value less than one percent (0.7%). Photomicrograph taken using plane-polarized light. Grainstone matrix within a foreslope debris interval, Richardson Point G-12, 7962.00 ft.

Figure B7

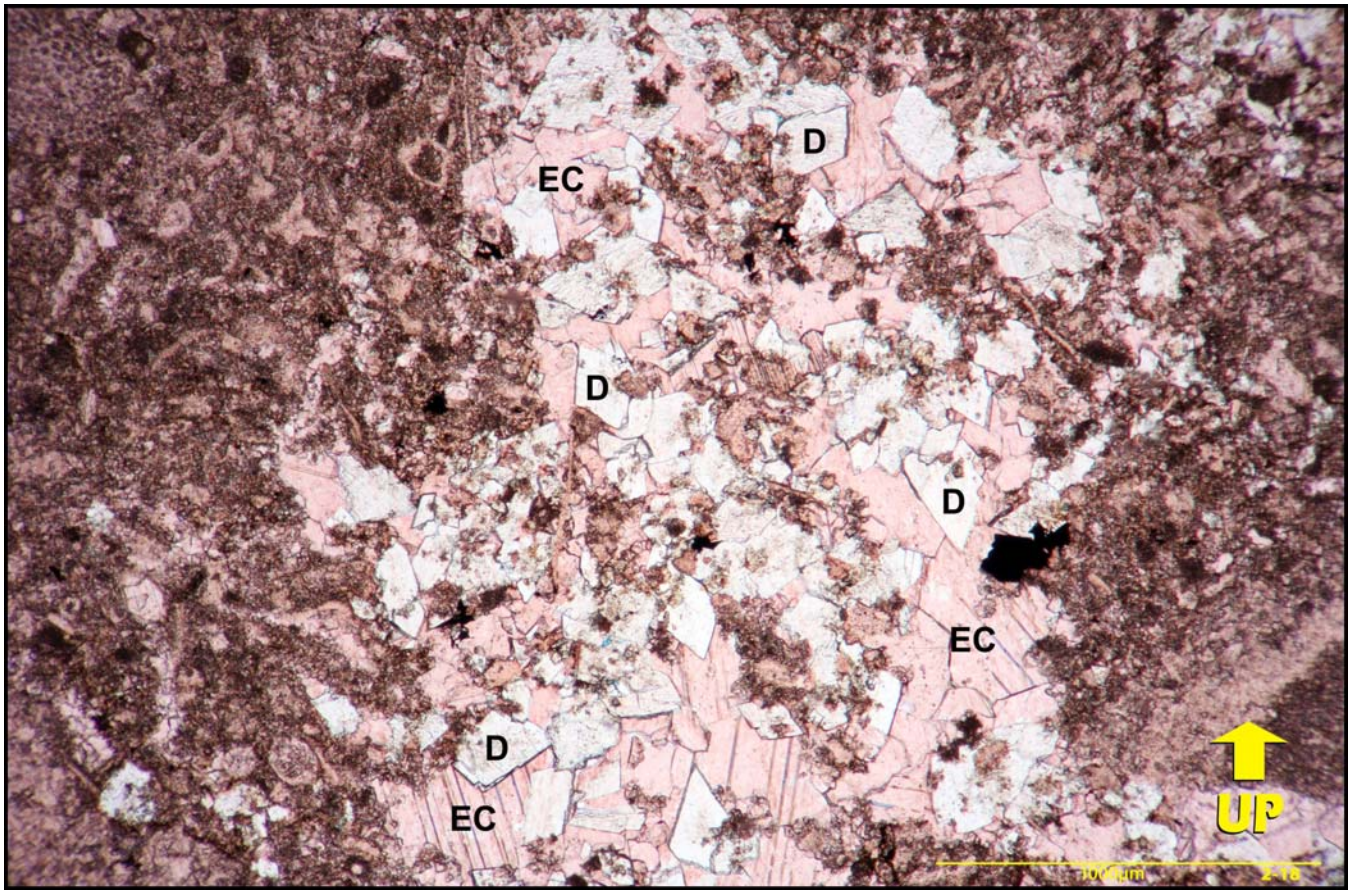

Enlarged view of cemented interparticle pores in a skeletal-bearing peloidal lime packstone sheltered by larger bioclasts. Rhombic dolomite crystals (D) replace parts of the peloids and skeletal particles and extend into the interparticle pores. The dolomite crystals are overgrown by coarse equant crystals of non-ferroan calcite (EC), which infill the macropores, reducing the measured porosity to a value less than one percent (0.5%). Photomicrograph taken using plane-polarized light. Distal foreslope sand facies, King Point West B-53, 3612.00 ft.

Figure B8

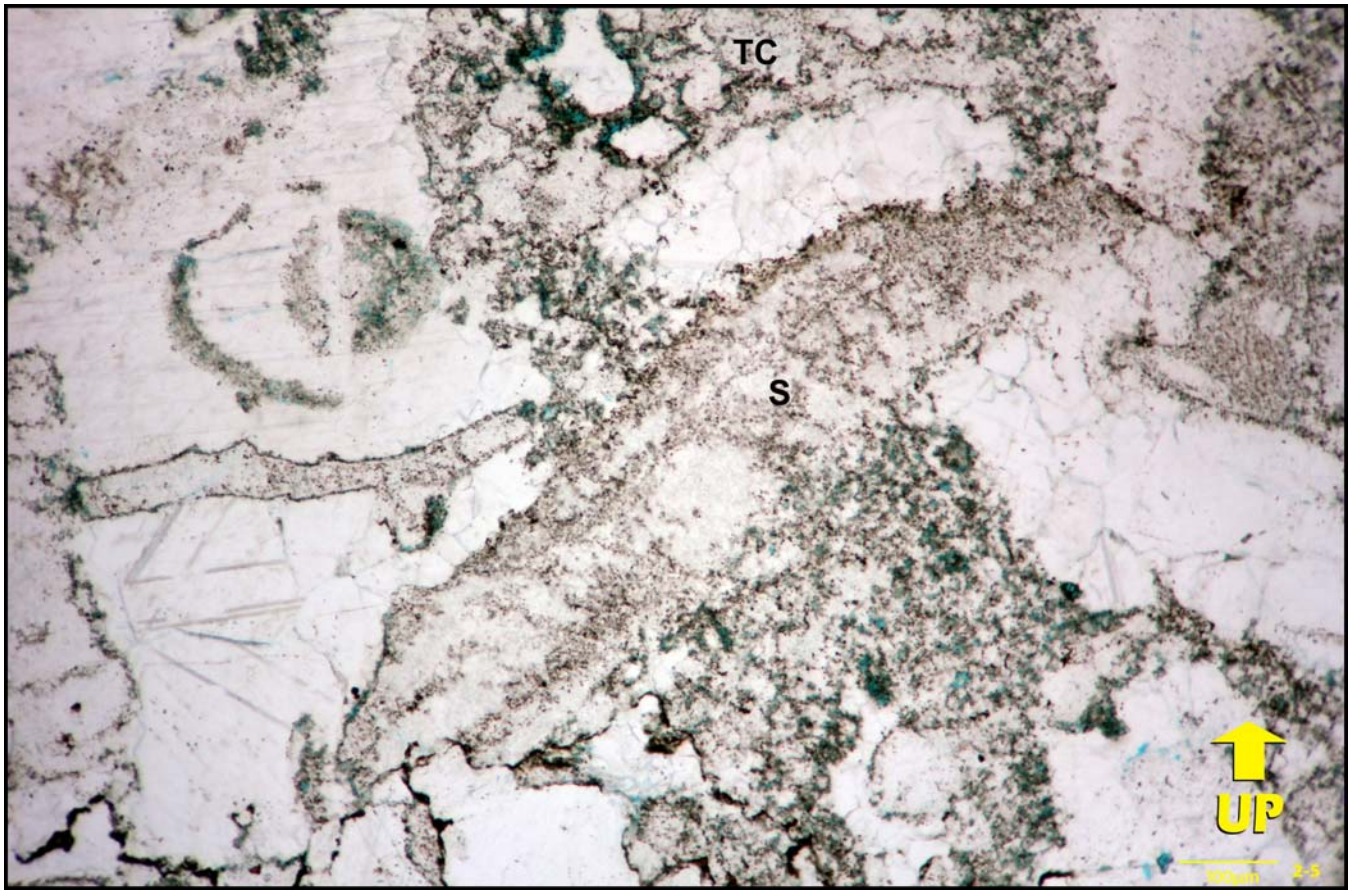

Open micropores of dissolution origin, impregnated by blue epoxy, within skeletal particles in a tabulate coral (TC)- and stromatoporoid (S)-clast lime floatstone with a skeletal packstone matrix. Equant calcite infills all macropores. This sample has a measured porosity of 1.0%, all micropores of dissolution origin. Photomicrograph taken using diffused plane-polarized light. Foreslope debris facies, Richardson Point G-12, 7916.90 ft.

Figure B9

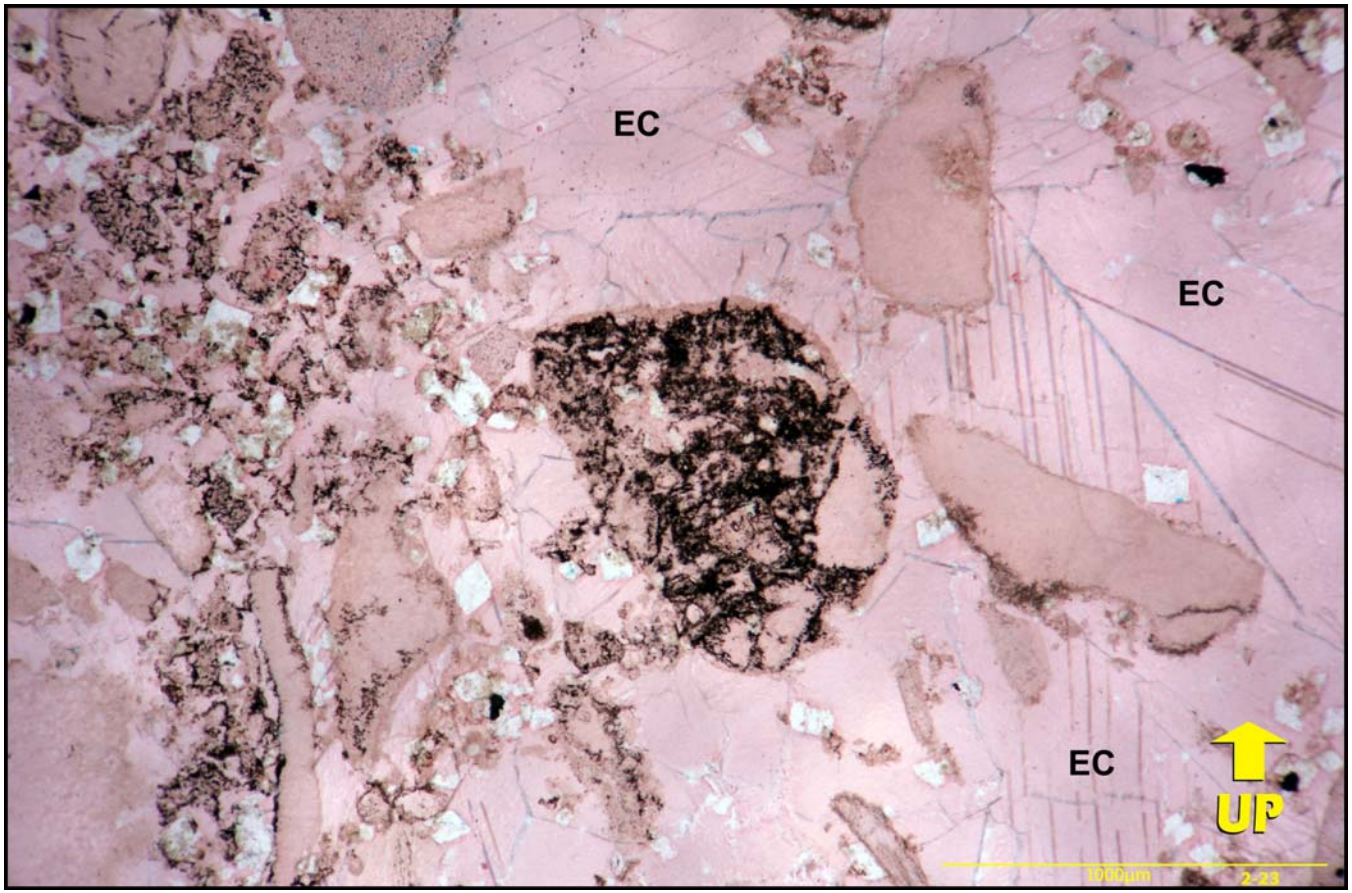

Bitumen plugging of micropores of dissolution origin in skeletal particles and the micritic portion of one intraclast (centre) within a skeletal lime grainstone. Coarse equant crystals of non-ferroan calcite (EC) infill the macropores. Measured porosity is 0.5%. Photomicrograph taken using diffused plane-polarized light. Foreslope sand facies, Key Point O-51, 7409.35 ft.

Figure B10

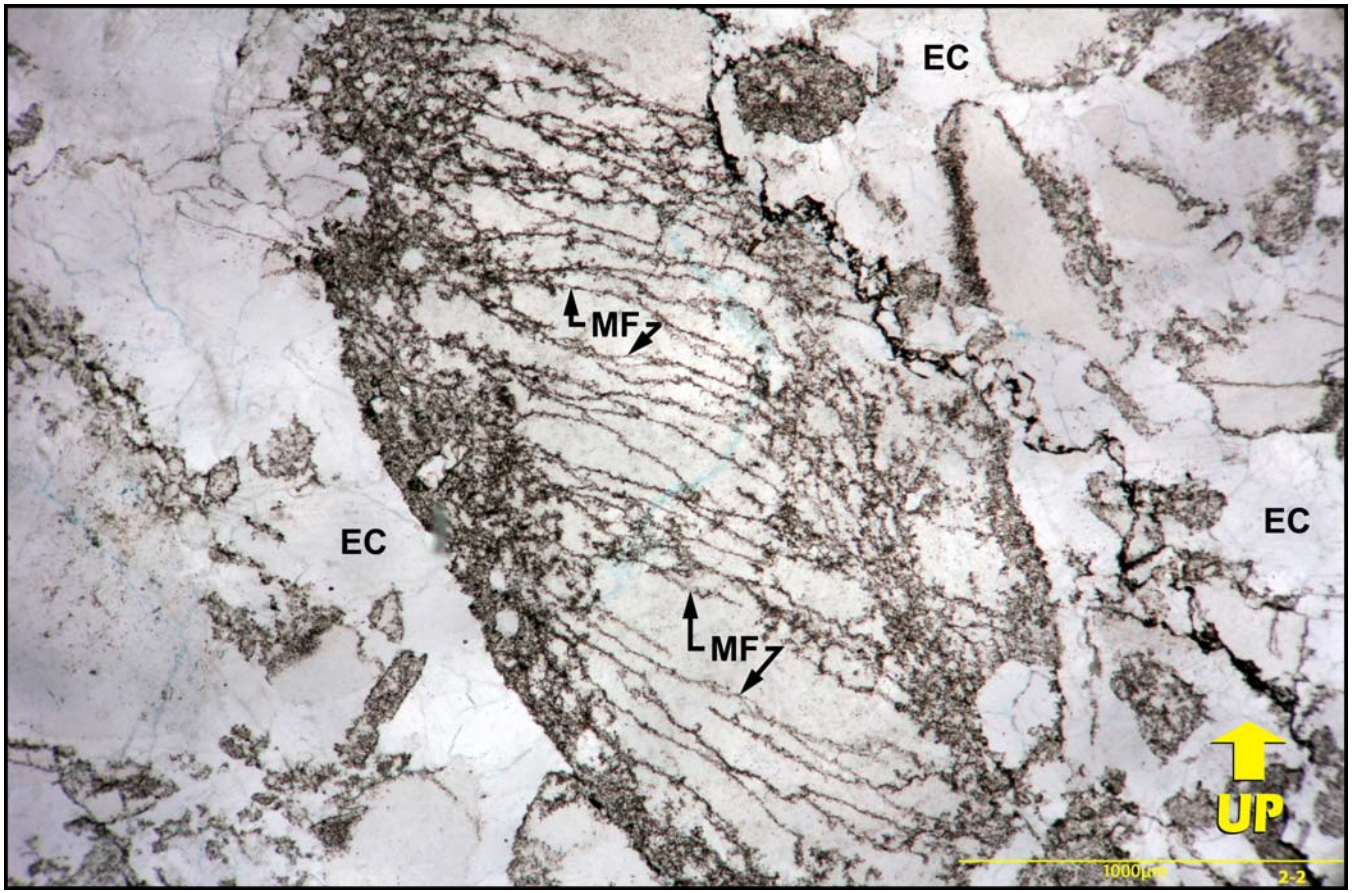

Bitumen plugging narrow micro-fractures (MF) in a branch of a dendroid tabulate coral within a lime floatstone containing a skeletal packstone matrix with a low micrite content. Bitumen also infills micropores of dissolution origin in the peripheral parts of the dendroid coral particle as well as in the associated finer skeletal particles. Equant calcite (EC) infills all macropores. The sample has a measured porosity of 0.9%. Photomicrograph taken using diffused plane-polarized light. Foreslope debris facies, Richardson Point G-12, 7960.00 ft.

SECTION C: SUMMARY OF CORES AND THIN SECTIONS FROM THE "BLUE FIORD" FORMATION ON PRINCE PATRICK ISLAND

Cores of the "Blue Fiord" Formation from two wells on Prince Patrick Island (Dyer Bay L-49 and Wilkie Point J-51) were examined. The intervals from both wells consist of limestone. Only one sample was taken for thin section examination, from Dyer Bay L-49. The age of the carbonates from these cores is uncertain. According to Harrison, the carbonates appear to be of undivided Late Silurian to Early Devonian age, generally older than the upper portion of the Blue Fiord Formation on Cameron Island, which ranges in age from Late Silurian to earliest Middle Devonian.

The core from Wilkie Point J-51 well consists of stromatoporoid and, to a much lesser extent, coral-bearing floatstones and minor rudstones. The stromatoporoids and corals have tabular and, to a lesser extent, laminar growth forms. The matrix consists of a very finely bioturbated mudstone to wackestone, containing some brachiopods but only rare crinoid columnals. The depositional environment is interpreted to be a low-energy, mid ramp. There is no observable porosity, although the core is moderately oil stained.

The core from the Dyer Bay L-49 well consists of lime mudstones containing a variety of fenestrae, including those of the laminar, irregular laminar and irregular forms (Figure C1). These limestones are interpreted to have been deposited in a subtidal algal marsh setting. The fenestrae are completely infilled by non-ferroan calcites of two generations (Figure C2). Firstly, inclusion-rich, dusty brown radiaxial calcites line the fenestrae. By analogy with numerous other examples, these cements are interpreted to have precipitated from marine pore waters. These cements have an isopachous distribution around the periphery of the fenestrae. This distribution implies precipitation of calcite from pore waters that completely infilled the fenestrae. This indicates precipitation of calcite from pore waters below the marine water table, supporting the interpretation of deposition of these limestones in a subtidal algal marsh environment as opposed to an intertidal environment where the cements would likely have a pendent distribution. Secondly, clear equant calcite crystals infill the remainder of the pore. As a result of calcite cementation, the limestones from this core have no observable porosity. Oil staining is lacking.

Figure C1

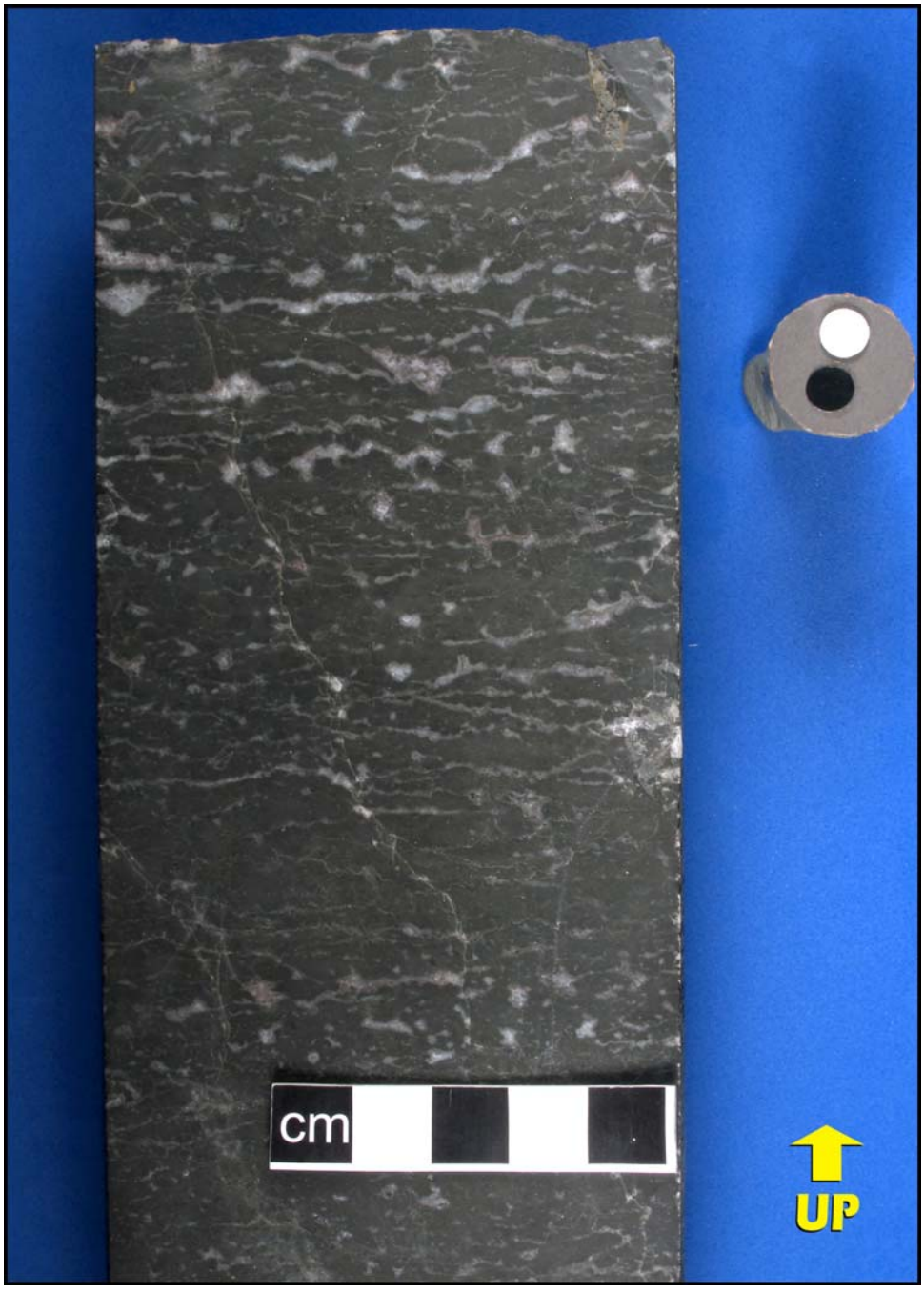

Core photograph of a lime mudstone containing abundant laminar and irregular laminar fenestrae. The fenestrae are completely infilled by the calcite cements illustrated in Figure C2. Photograph taken of a dry core surface. Dyer Bay L-49, 10382.50 ft.

Figure C2

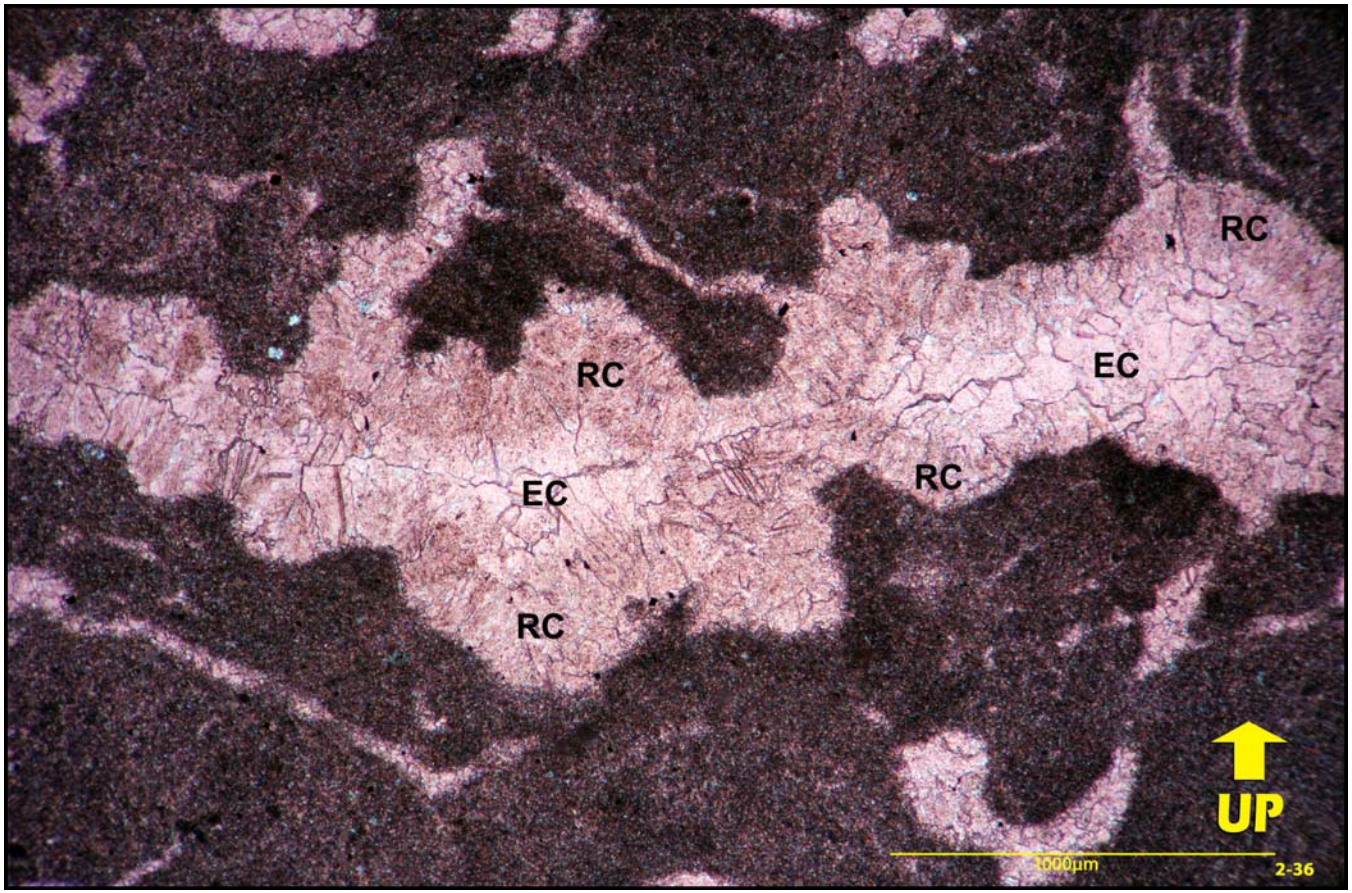

Photomicrograph showing the non-ferroan calcite cements that infill the fenestrae from the core piece illustrated in Figure C1. Two generations of calcite cement are present. Firstly, inclusion-rich crystals of dusty brown radiaxial calcite (RC) form an isopachous rind around the periphery of the fenestrae. Secondly, clear crystals of equant calcite (EC) infill the remainder of the fenestrae. Photomicrograph taken using plane-polarized light. Dyer Bay L-49, 10382.38 ft.

SECTION D: SUMMARY OF CORES AND THIN SECTIONS FROM THE"BLUE FIORD" FORMATION FROM WELLS ON BANKS ISLAND

General

Cores from intervals of the "Blue Fiord" Formation in 5 wells were examined. Thin sections were made from samples taken from cores in three of these wells (Parker River J-72, Muskox D-87 and Kusrhaak D-16). No samples for thin sections were taken from Tiritchik M-48 or Storkerson Bay A-15. Photographs were taken from all cores except for the one in Tiritchik M-48.

Tiritchik M-48 (Central Banks Island)

One core was taken from the upper part of the "Blue Fiord" Formation (4631-4640 ft., uncorrected to log depths). The log-defined top of the "Blue Fiord" Formation is 4633 ft. The presence of an overlying Kitson Formation suggests that the "Blue Fiord" from this core is older than at least the upper part of the Blue Fiord Formation on Cameron Island.

The core consists of very dark grey, finely bioturbated, slightly to moderately argillaceous lime mudstones to sparsely fossiliferous wackestones with a few cm-scale crinoid-skeletal packstone interbeds. The fauna includes common crinoid columnals, bivalve and brachiopod fragments, stylolinids and tentaculitids; and a few gastropod, ostracode and trilobite fragments.

These limestones are interpreted to have been deposited in a downslope ramp environment below fair weather wave base but above storm wave base. These limestones are more argillaceous than the limestones in the underlying interval from this well and are interpreted to be part of a deepening phase leading to the onset of deposition of organic-rich deposits of the Kitson Formation in a deep basinal environment.

The limestones from this core have no visible porosity or permeability.

Storkerson Bay A-15 (Western Banks Island)

The stratigraphic position of the core (6446-6473.5 ft.) is uncertain because no logs were run below a depth of 5916 ft. The well report submitted to the National Energy Board lists the top of the "Blue Fiord" Formation at 6394 ft. and describes limestones from well cuttings to the base of the well (6710 ft.).

The core consists of repeated limestone successions grading upward from floatstones of variable content up into finely bioturbated mudstones and wackestones with a restrictive fauna, and then into overlying mudstones and wackestones with irregular laminar and tubular fenestrae. The floatstones contain small branching tabulate corals (*Coenites* and *Thamnopora*) as well as *Amphipora* and have a wackestone to mudstone matrix. The branching tabulate corals and *Amphipora* commonly, but not always, occur together.

The limestone successions are interpreted to comprise repeated subtidal to intertidal cycles. Branching tabulate coral-dominated floatstones occur in the basal portions of some cycles and are interpreted to have been deposited in an open subtidal environment, the most basinward position of any facies in this core. *Amphipora*-dominated floatstones overlie the tabulate coral-dominated floatstones in some cycles and are interpreted to have been deposited in a slightly shallower subtidal environment. The bioturbated mudstones and wackestones are interpreted to have been deposited in a very restricted and shallow subtidal environment. The fenestral-bearing mudstones and wackestones at the top of the cycles are interpreted to have been deposited in an intertidal environment.

The common occurrence of branching tabulate corals with *Amphipora* suggests deposition on a carbonate ramp rather than on a platform fringed with a barrier reef. These fauna normally do not occur together. On a barrier reef fringed carbonate platform, branching tabulate corals normally occur in positions basinward of the barrier reef crest, whereas *Amphipora* most commonly occur in positions behind the reef margin. The mixing of these two faunal elements indicates the lack of a barrier reef and

therefore suggests deposition on a gently basinward-sloping ramp where wave dampening is much more gradual. Mixing of distinct and normally separated faunal elements is more likely in this setting.

The matrix of these limestones has no visible porosity and permeability. Only very minor fracture porosity is present. Calcite and minor fluorite cements infill fractures wider than those with hairline dimensions (Figure D1). Bitumen occurs in hairline fractures and follows calcite as the final infiller of wider fractures (Figure D2).

Parker River J-72 (Easternmost Banks Island)

Introduction

Two cores of the "Blue Fiord" Formation were taken (949-960 m and 1002-1005 m). The "Blue Fiord" top is 919.00 m. In this well, the "Blue Fiord" Formation is overlain by the Kitson Formation. This suggests that the "Blue Fiord" in this well is older than the upper part of the Blue Fiord Formation on Cameron Island.

Upper core (949-960 m)

This core consists of limestone with only minor dolomite. The lower approximate 1m of the core consists of common floatstones containing various stromatoporoids and corals, and one interval of *Euryamphipora* rudstone (Figure D3). Both these lithologies have a micritic-dominated matrix. The stromatoporoid and coral-bearing floatstones and rudstones grade up into a succession of bioturbated wackestones with a restricted fauna and wackestones containing irregular laminar and tubular fenestrae, capped by a well-developed paleosoil. The paleosoil contains rhizoliths (root traces) lined by cutans (Figure D4). The remainder of the core, above the paleosoil, consists of interbedded bioturbated mudstones and wackestones with a restrictive fauna (Figure D5) and micritic intervals containing irregular laminar, laminar and tubular fenestrae (Figure D6).

An unusual aspect of the upper succession, above the paleosoil, is the occurrence of irregular to horseshoe-shaped cm-scale cavities (Figure D7). The cavities are mainly filled by a variety of very fine sand to granule-size particles consisting of single crystals of sparry calcite and very coarse sand to granule-size bodies with subspherical and elongate shapes consisting of an outer wall and an interior of a mosaic of sparry calcite crystals (Figures D8, D9, and D10). Micron-scale (mud to fine silt size) crystals of replacive dolomite occur in the intertices between the coarser particles and bodies. Higher magnification views of the infill of a horseshoe-shaped cavity are illustrated in Figures D11, D12, and D13. The bodies with subspherical and elongate shapes are interpreted to be the intact remains of a calcium carbonate secreting organism of unknown affinity that lived in the burrow cavities. The particles consisting of single crystals of sparry calcite are interpreted to have formed from the decomposition and disaggregation or breakup of this organism.

The limestones in this core have no observable porosity or permeability.

Lower core (1002-1005 m)

This core consists of medium to dark brown-coloured dolostones. The lower approximate 1 m of the core varies from dolorudstones to dolofloatstones containing tabular and laminar stromatoporoids, as well as fragments of stromatoporoids of uncertain or unknown growth forms (Figure D14). The upper approximate 2 m of the core is mainly a fabric destructive dolomite containing only a few identifiable tabular and laminar stromatoporoids. The rocks in this core interval are interpreted to have been deposited in either a mid-ramp or a foreslope environment.

The dolomite consists of very fine to fine sand-size crystals with planar-s and subordinate nonplanar-a textures (Figure D15). Rhombic dolomite crystals and somewhat later crystals of saddle dolomite occur in some vugs (Figure D16). Speculatively, the dolomite is interpreted to be of hydrothermal origin.

Eight full-diameter samples and one small-diameter core plug were analyzed from this interval. The full-diameter samples have measured porosities that range from 4.5 to 13.8% (7.46% average) and K_{max}'s that range from 0.80 mD to 50.40 mD. The dominant pores are intercrystalline (Figure D17) supplemented by some solution vugs that range in extent from mm's to 5 cm across. High porosity samples generally correspond to those with good to excellent intercrystalline porosity (Figure D18). Full-diameter sample 1, with a K_{max} of 50.40 mD, has large solution vugs which contribute significantly to the permeability (Figure D19).

Muskox D-87 (2073-2091 m) (Eastern Banks Island)

The core interval occurs in the upper part of the "Blue Fiord" Formation, approximately 5.5 m below the top of the Formation. The core interval is characterized by an intermediate radioactive response on the gamma ray log and occurs only 15 m above an interval with a very radioactive gamma ray log signature, typical of basinal strata. The presence of an overlying Kitson Formation suggests that the "Blue Fiord" Formation interval in this well is older than the upper part of the Blue Fiord Formation on Cameron Island.

The core interval consists of fine to coarse sand-size crystalline dolomite and contains both zebroid fabrics and vugs of dissolution origin. The dolomite is fabric destructive, with only minor vestiges of recognizable bioclasts. Bioclasts include massive and stick forms of uncertain affinity, "massive" tabulate corals and crinoid columnals, and rare clasts of "massive" stromatoporoids. Samples from this interval are interpreted to have been deposited in either a downslope mid-ramp or foreslope environment.

The diagnostic element in this core is the occurrence of zebroid fabrics. The zebroid fabrics consist of alternate bands of matrix dolomite and white saddle dolomite crystals that grew into elongate zebroid pores. The most common zebroids are patches containing horizontal to sub-horizontal internal orientations or less commonly inclined internal orientations (Figure D20). Other zebroids consist of more laterally extensive bed-parallel forms, with horizontal and sub-horizontal internal orientations or, less commonly, slightly inclined internal orientations (Figure D21).

The matrix dolomite consists of fine to coarse sand-size crystals with nonplanar-a textures (Figures D22 and D23). Dolomite crystal sizes are commonly controlled by the size of the particle being replaced. Crinoid columnals are replaced by unusually coarse solitary dolomite crystals (Figure D24). Dolomite crystals facing open pores commonly consist of an inclusion-rich core and an inclusion-lean outer rim (Figure D25).

Solution vugs are of two varieties. The first are apparently discrete vugs with dimensions from less than 1 cm to a few cm's across (Figure D26). The second type of vug, which occurs much more commonly than the first, consists of a network of "channels" with dominantly horizontal or sub-horizontal orientations, but with oblique channels that join the more horizontal channels (Figure D27). Wider portions of the channels remain open and likely connect in some manner to an open three-dimensional framework.

White crystals of saddle dolomite occur as linings and extensive infills of both the zebroid pores and solution vugs, as well as in the wider fractures (Figures D20, D21, D26, and D27). When viewed in thin section, crystals of saddle dolomite can be seen to have curved and commonly stepped faces (Figure D28). When facing open vugs or zebroid pores, some saddle dolomite crystals have an inclusion-rich core and a clear inclusion-lean outer rim (Figure D29). Smaller more translucent crystals of rhombic dolomite commonly overgrow crystals of saddle dolomite and face open vugs or zebroid pores (Figure D26).

The matrix, saddle and rhombic dolomites are interpreted to have formed as part of a hydrothermal system, at temperatures higher than the ambient formation temperature. Elevated temperatures are indicated by both the nonplanar textures of the matrix dolomite crystals and by the occurrence of saddle dolomite cements. The evolution from saddle to rhombic dolomite cement may reflect the change in

formation from higher temperature more concentrated brines to cooler, less concentrated fluids. Furthermore, the presence of zebroid fabrics in these dolostones suggests that hydrothermal dolomitization occurred along fault conduits (Davies and Smith, 2006).

Vugs in these dolostones also contain minor concentrations of authigenic quartz crystals. These crystals are the final infiller of the vugs, as they overgrow both crystals of saddle and rhombic dolomite (Figure D30). Davies and Smith (2006) interpret quartz as one of the final products in a hydrothermal system.

Petrographic relationships provide insights on the timing of matrix dolomitization and saddle dolomite cementation. Two relationships are worth noting. Firstly, crystals of saddle dolomite from the same phase infill both zebroid pores and fractures cutting the zebroids and host replacement dolomites (Figures D31 and D32). From this relationship, the following paragenetic succession is deduced: hydrothermal dolomite replacement of the limestone matrix→ fracturing→ saddle dolomite cementation. Thus, the phases of hydrothermal matrix dolomitization and saddle dolomite cementation are separated by a hiatus (of probable short duration) corresponding to the interval of fracturing. Because the fractures cut matrix replacement dolomites and are infilled by saddle dolomite, fracturing is interpreted to be part of the hydrothermal phase. Secondly, horizontal stylolites truncate both the matrix replacement dolomites and saddle dolomite cements infilling zebroid pores (Figure D33). From this relationship it can be inferred that the final phase of stylolitization followed both matrix dolomitization and saddle dolomite cementation. Regional studies in this area conclude that there is little or no burial of strata following Ellesmerian loading in Late Devonian time (Ashton Embry and Keith Dewing, personal communications). Thus, it is likely that the final phase of stylolitization occurred in Late Devonian time. If these interpretations are correct, hydrothermal dolomitization is constrained to Devonian time.

The core contains a moderate degree of fractures. Fractures vary from short cm-scale to longer ones that can be traced several cm's. They also vary in width. Wide fractures vary from those completely or almost completely infilled by saddle dolomite crystals and some rhombic dolomite crystals to those that are dominantly open (Figures D31 and D32). Very narrow fractures have steeply inclined to vertical orientations and are infilled by bitumen (Figure D21).

Forty-five full-diameter pieces were analyzed for porosity. Porosity in these full-diameter pieces range from 0.09 to 8.5%, with an average of 3.94%. Pores include common dissolution vugs (Figures D26 and D28), intercrystalline voids (Figure D34), and partially open to open zebroid pores (Figures D20, D21 and D29). Finger-shaped molds occur less commonly (Figure D35).

Forty-three of the full-diameter samples were analyzed for permeability. K_{max}'s of these intervals range from 0.01 mD to 2530 mD, with an average of 68.31 mD.

Thirty-eight of the 43 full-diameter pieces have K_{max}'s less than 10 mD. K_{max}'s of these samples range from 0.01 mD to 8.80 mD with an average K_{max} of 1.41 mD. Twenty-nine of these samples have K_{max}'s less than 1 mD.

Five of the 43 full-diameter pieces have K_{max}'s that range from 24.3 mD to 2530 mD with an average K_{max} of 576.38 mD. High permeability in four of these samples is attributed to a combination of open fractures, dissolution vugs and zebroid pores. The high permeability in the other sample appears to be due to a combination of intercrystalline pores and solution vugs.

A drill stem test within an interval including the core shows a good pressure buildup, indicative of overall high permeability. It is concluded that the overall high permeability is due to high permeabilities in only selected intervals.

Kusrhaak D-16 (East-Central Banks Island)

Two cores were taken from the "Blue Fiord" Formation (11995-12025 ft. and 12450-12477.5 ft.). The top of the upper core is approximately 100 ft. below the top of the "Blue Fiord" Formation (11900 ft.). The "Blue Fiord" interval is overlain by radioactive shales of the Blackley Formation, suggesting that the

"Blue Fiord" Formation in this well is older than the upper part of the Blue Fiord interval on Cameron Island.

Both cores consist of primarily dolobreccias with lesser degrees of extensively fractured dolostones in the lower core. Following the classification of breccias presented by Loucks (1999), the upper core interval consists primarily of matrix-rich clast-supported chaotic breccias with some mosaic and crackle breccias (Figures D36 and D37). The dolobreccias in the lower core are dominantly clast-supported but matrix-supported chaotic breccias do occur. The clast-supported breccias in this core interval vary from crackle and mosaic breccias to matrix-rich clast-supported chaotic breccias. Pore-filling cements in both breccia intervals are restricted in occurrence to some sheltered pores that occur beneath mainly breccia clasts as well as to some fractures.

The matrix between the breccia clasts consists of detrital dolomite particles. These particles are most commonly silt-sized, but range in size from mud- to sand-sized (Figures D38 and D39).

The dolomite in the breccia clasts and that replacing the allochems varies from very fine to fine sand-sized crystals. Despite the fine crystal size the dolomite is primarily fabric destructive. Only minor occurrences of tabular stromatoporoids and *Amphipora* could be identified in either core or in thin section. At relatively high power magnification, the replacive dolomite can be seen to consist of nonplanar-a textures, with curved crystal interfaces (Figure D40).

Unusual cm-scale vertical growths, of uncertain original composition, occur beneath the tabular stromatoporoid clast illustrated in Figure D40. They are interpreted to have tubular geometries (Figure D41). These growths are interpreted to be discrete tubes, but may coalesce to form wider masses and even have cross-partitions that connect the individual tubes. Detrital dolomite internal sediment occurs above the cross-partitions. The intervening areas between the tubes are infilled by crystals of saddle dolomite and by even later coarser crystals of non-ferroan calcite. At higher magnification, the tubes can be seen to consist of an outer narrow wall, replaced by saddle dolomite, and a hollow interior infilled by saddle dolomite (Figure D42). These growths are speculated to be pendent microbial growths that grew down into a primary pore that was sheltered by an overlying tabular stromatoporoid clast.

A major question is the nature of the process involved in the brecciation and in the formation of the detrital dolomite matrix that occurs between the breccia clasts. Two types of processes are possible: physical tectonic forces and dissolution of dolomite. The photographs of cores and thin sections in Figures D43, D44, D45, D46, D47, and D48 are pertinent to discriminating between these two processes.

Overall, physical tectonic forces appear to have been dominant. The following observations support this interpretation:

1) There is a strong association between fracturing and the formation of some breccias, especially of the crackle and mosaic varieties (Figures D43, D45, and D46). It is hard to envisage any other process than a physical tectonic force to form crackle and mosaic breccias, where displacement between breccia clasts is low.
2) In some dolobreccias, there is a gradual continuum from large cm-scale clasts to smaller coarse sand-size clasts to even finer sand to mud size matrix particles (Figure D43). This observation strongly supports the interpretation that both the breccias and the detrital dolomite matrix formed from the same process. The continuum of particle size is most easily explained by the physical breakdown of the host dolostone into discrete particles.
3) Some of the core intervals containing breccias have steeply inclined stylolites (Figures D43 and D44), indicative of compressive tectonic forces. This observation strongly supports the interpretation that brecciation and formation of the detrital dolomite matrix formed from fault-associated tectonic forces.

However, dissolution cannot be dismissed as contributing to the formation of the detrital dolomite matrix. The dolomite within portions of some breccia clasts in both crackle or mosaic breccias (Figures D45 and D46) and in some clast-supported chaotic breccias (Figures D47 and D48) has broken down to a fine particulate dolomite, identical to that of the detrital dolomite matrix. This breakdown is

more prevalent in the outer portion of breccia clasts and diminishes inward (Figures D46 and D48). This fabric can be interpreted to be of dissolution origin, by chemical breakdown from fluids that flowed from the fractures into the host rock dolomite. The presence of this fine particulate dolomite within portions of dolomite breccia clasts in crackle or mosaic breccias, where displacement of breccia clasts is minimal, indicates that the process of breakdown to form finer particles occurred *in situ*. Potentially, this fine *in situ* particulate dolomite is a possible source of the detrital dolomite matrix.

Nevertheless, fracturing plays an important role in breccia formation. Bitumen-infilled narrow fractures commonly occur within dolobreccia clasts (Figures D37 and D43) but in a few cases cut across both the dolobreccia clasts and the detrital dolomite matrix (Figure D49). Although these fractures clearly follow breccia formation, they are interpreted to be part of a related, albeit somewhat later, fault-related process.

Cements almost completely infill the sheltered pores that occur beneath the dolobreccia clasts as well as infilling the wide fractures. These pores are lined by crystals of saddle dolomite (Figures D50, D51, and D52). These crystals commonly have an inclusion-rich core and an inclusion-lean outer rim. Some saddle dolomite crystals have interbanded inclusion-rich and inclusion-lean zones (Figure D52). Crystal lengths of saddle dolomite most commonly range from 500 µm to 1000 µm, but crystals with lengths up to 6000 µm are present.

Crystals of saddle dolomite are overgrown by both quartz crystals (Figures D51 and D52) and, more commonly, by crystals of non-ferroan calcite (Figures D50 and D51). Quartz cement crystals were only observed in the lower core interval, although minor patches of quartz were observed replacing matrix dolomite in the upper core interval. Lengths of quartz cement crystals range up to 8000 µm. The quartz cement crystals have euhedral crystal faces that either face open pores (Figure D52) or are later overgrown by macro crystals (lengths exceeding 1 cm) of non-ferroan calcite (Figure D51). Measured crystal lengths of non-ferroan calcite vary from coarse sand size (500 µm - 1000 µm) to, more commonly, that exceeding 1000 µm (1000-8000 µm). These crystals are the main filler of sheltered pores beneath dolobreccia clasts.

Bitumen is present in both core intervals, most commonly infilling pores of dissolution origin. The most abundant occurrence of bitumen is as an infiller of solution vugs that occur in coarse sand- to macro-size crystals of non-ferroan calcite. Bitumen commonly infills vugs in macrocalcite crystals at positions along the periphery of saddle dolomite crystals (Figure D53). These positions would have been preferential flow paths of fluids that dissolved the more soluble calcite. Less commonly, bitumen occurs in pores of dissolution origin within crystals of saddle dolomite, both in micropores and in larger vugs. In one sample, bitumen occurs in micropores of dissolution origin that occur in bands within the outer part of saddle dolomite crystals that line the sheltered pores between dolobreccia clasts (Figure D54). In this sample these bands can be traced virtually completely around the periphery of these pores. Rarely, bitumen infills vugs of dissolution origin that occur in replacement dolomite.

In some sheltered pores between dolobreccia clasts, fractures cross-cut bitumen that infills vugs of dissolution origin in the macrocalcite cement (Figure D55). Significantly, the fractures do not extend into the surrounding dolobreccia clasts. These fractures are interpreted as having formed from shrinkage due to de-gassing during the transformation of oil to bitumen. These fractures are infilled by a later phase of both saddle dolomite and non-ferroan calcite cements.

From this analysis, the following paragenetic succession is postulated:

1) Hydrothermal dolomitization of limestone, as evidenced by nonplanar dolomite crystal textures. The occurrence of steeply inclined stylolites of compressional origin is suggestive that dolomitization occurred along fault conduits. Davies and Smith (2006) point out hydrothermal dolomites commonly occur along wrench faults, which may have compressional features such as positive flower structures and folds.

2) Interval of fracturing, brecciation and fine breakdown of dolomite into fine detrital dolomite. Detrital dolomite infills most pores between dolobreccia clasts, except those effectively sheltered by overlying dolobreccia clasts.
3) Saddle dolomite cementation in wide fractures and along the periphery of the pores sheltered beneath dolobreccia clasts.
4) Quartz cementation in some of the pores sheltered beneath dolobreccia clasts.
5) Infilling of most of the remaining pores sheltered beneath dolobreccia clasts by coarsely crystalline and macro-crystalline calcite.
6) Late stage dissolution of calcite cements and less commonly saddle dolomite, creating vugs and micropores.
7) Migration of oil into vugs, micropores and fractures.
8) Formation of shrinkage fractures in the bitumen, due to de-gassing during the transformation of oil to bitumen.
9) Later cementation of the shrinkage fractures by saddle dolomite and calcite.

Twenty-eight full-diameter core segments from the lower core interval were analyzed for porosity and permeability. Porosity values range from 0.8 to 4.1% and average 2.10%. K_{max} values range from 0.04 mD to 11.10 mD and average 2.13 mD. The pores occur as unfilled parts of pores sheltered beneath dolobreccia clasts and as unfilled parts of some fractures.

The upper core interval was not analyzed but visually shows low porosity and permeability.

Speculated Scenario of Dolomitization of "Blue Fiord" Limestones on Banks Island

Reservoir quality required for either gas or oil production is restricted to dolostones. All limestone intervals are tight.

Dolomite intervals occur in three wells on Banks Island: Muskox D-87, Kusrhaak D-16 and Parker River J-72. All three wells occur in the eastern part of the island. The dolomites in Muskox D-87 are characterized by nonplanar crystal textures and by the presence of zebroid fabrics and vugs of dissolution origin. The dolomitized intervals in the Kusrhaak D-16 well consist of dolobreccias with clasts containing dolomites with nonplanar crystal textures. Some steeply inclined stylolites of compressional origin are present. The dolomites in the Parker River J-72 well have a mixture of planar-s and subordinate nonplanar-a crystal textures.

Dolomitization is interpreted to be from hydrothermal fluids at elevated temperatures significantly higher than the ambient formation temperatures. Hydrothermal dolomitization at the sites of the Muskox D-87 and Kusrhaak D-16 wells are interpreted to have formed along wrench faults. Davies and Smith (2006) concluded that there is a strong preference for hydrothermal dolomitization along these types of faults. The zebroid-bearing dolostones from the Muskox D-87 well are interpreted as having formed in transtensional pull-aparts, such as negative flower structures (refer to figure 6 of Davies and Smith, 2006). The dolobreccias from the Kusrhaak D-16 well are interpreted to have formed in a more compressive position along a wrench fault. The dolomites from the Parker River J-72 are interpreted as having formed from lower-temperature hydrothermal fluids more distant from a wrench fault.

References

Davies, G.R. and Smith, L.B., 2006. Structurally controlled hydrothermal dolomite reservoir facies: An overview; Bulletin of American Association of Petroleum Geologists, v. 90, p. 1641-1690.

Loucks, R.G., 1999. Paleocave carbonate reservoirs: Origins, burial-depth modifications, spatial complexity, and reservoir implications; Bulletin of American Association of Petroleum Geologists, v. 83, p. 1795-1834.

Figure D1

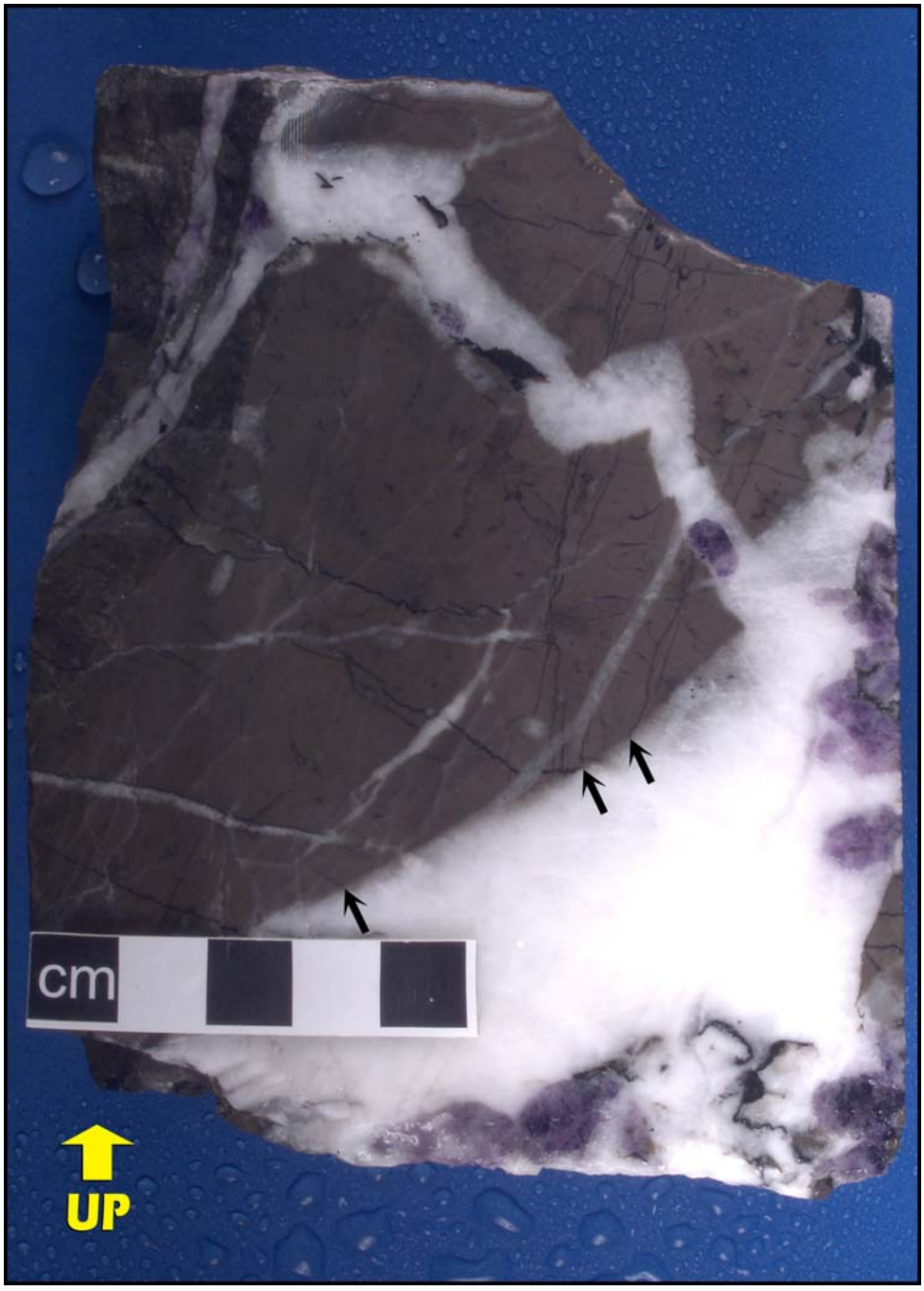

Core photograph showing purple-coloured crystals of fluorite and later very coarse crystalline crystals of white-coloured calcite infilling wide fractures that cut a tight lime mudstone/wackestone. Bitumen infills hairline fractures that terminate along the margin of the wide fractures (arrows). Photograph taken of a wetted core surface. Storkerson Bay A-15, 6453.24 ft.

Figure D2

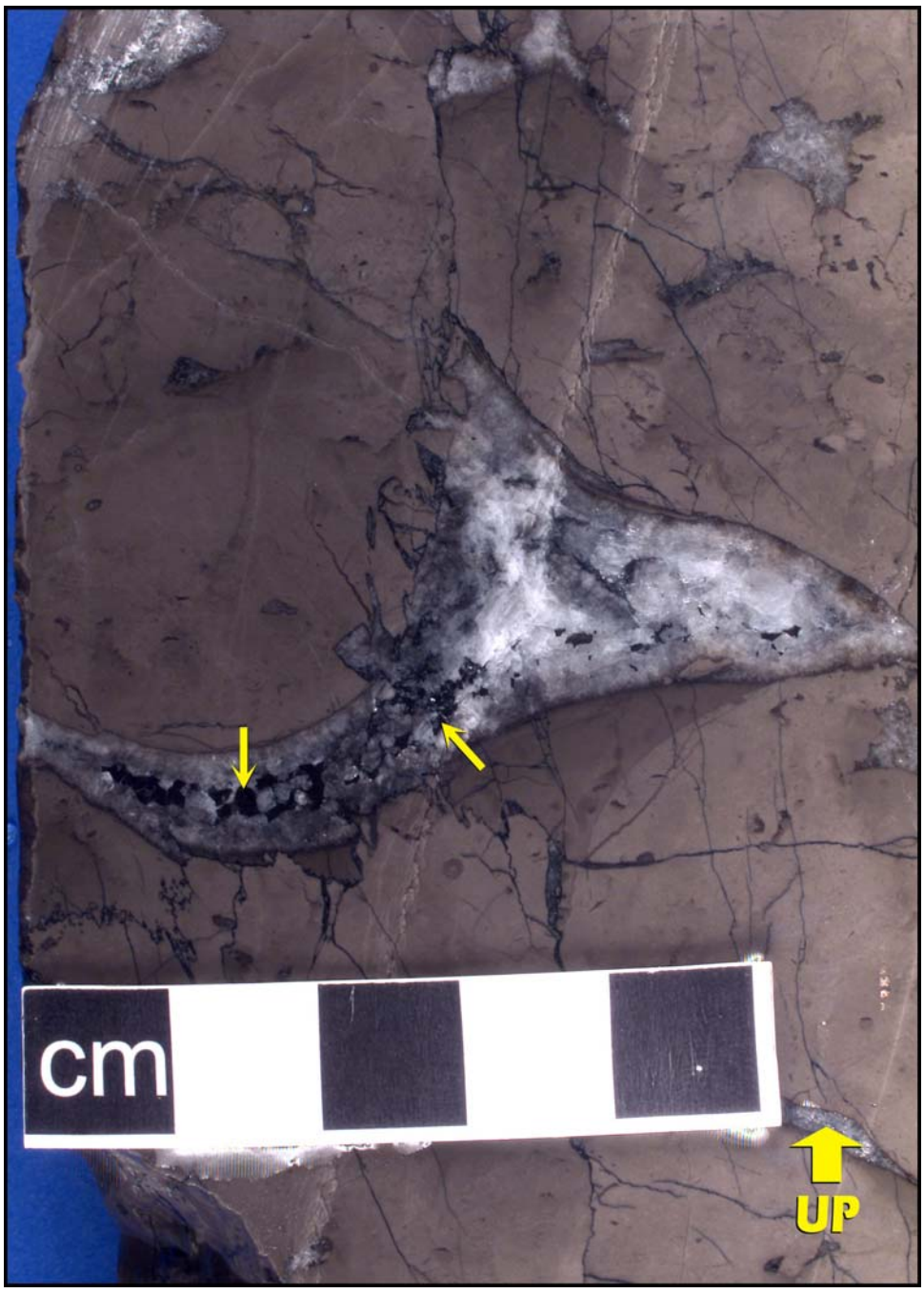

Core photograph showing bitumen (arrows) as the final infiller of a wide fracture that cuts a tight lime mudstone/wackestone. The bitumen is preceded by the precipitation of bladed and equant calcite cements. Bitumen also infills hairline fractures that terminate along the margins of the wide fracture (arrows). Photograph taken of a wetted core surface. Storkerson Bay A-15, 6448.53 ft.

Figure D3

Core photograph of a *Euryamphipora* lime rudstone with a dark-coloured micritic matrix. Photograph taken of a wetted core surface. Parker River J-72, 959.33 m.

Figure D4

Core photograph illustrating the rooted zone in a paleosoil that caps the lower succession of the upper core interval in the Parker River J-72 well. In ascending order, this photograph shows a thin interval of illuviated green clay (above the scale bar), a 4.5-cm interval containing rhizoliths (root traces) lined with dark-coloured cutans, and a 1.5-cm homogenized interval above a diconformable surface in the paleosoil. The transgressive surface caps a 10-cm-thick green clay aerosoil that overlies this core piece. Photograph taken of a wetted core surface. Parker River J-72, 957.35 m.

Figure D5

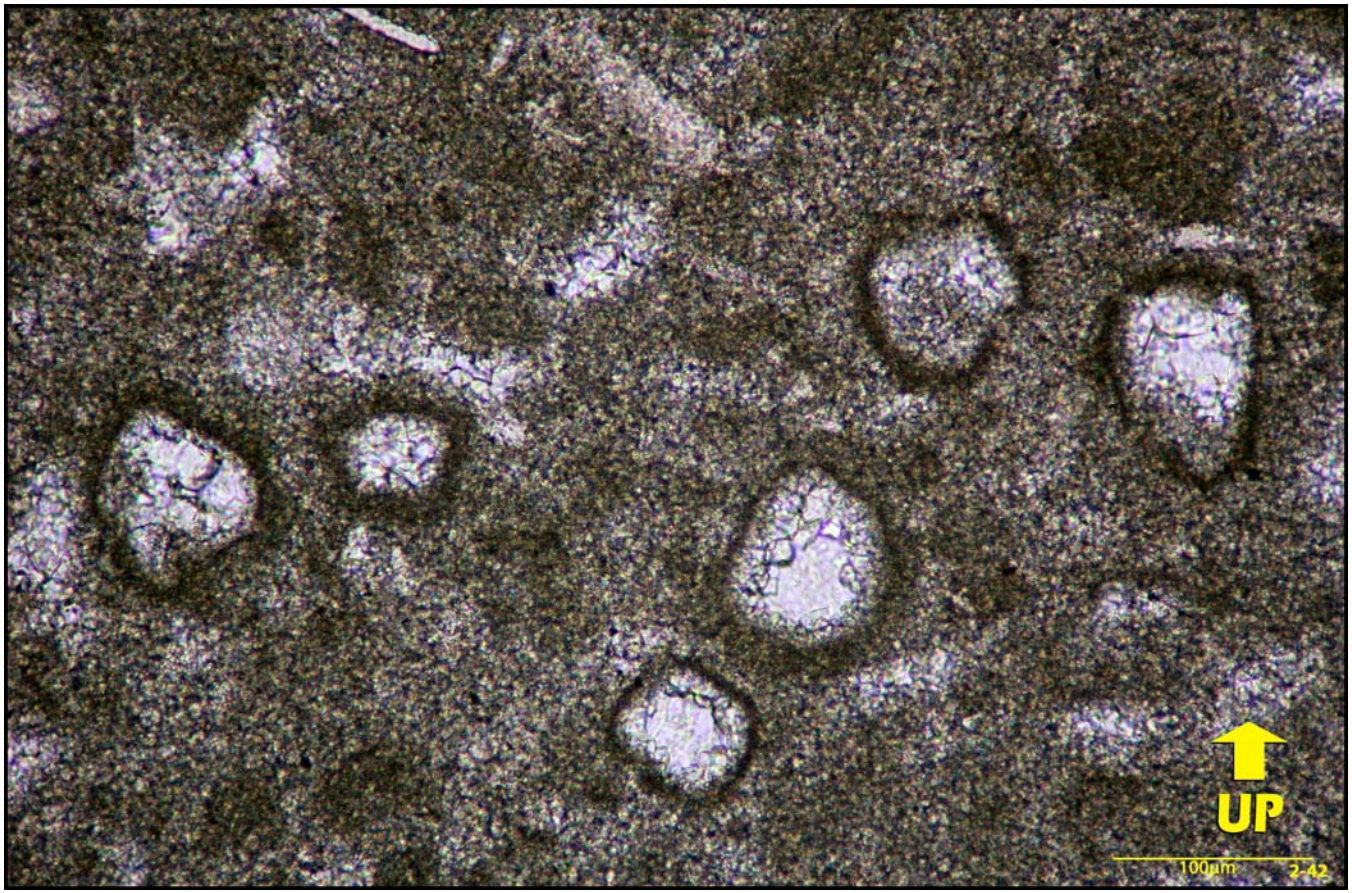

Photomicrograph of subspherical shaped benthic foraminera (?) in a pelletal lime wackestone. Photomicrograph taken using plane-polarized light. Parker River J-72, 955.05 m.

Figure D6

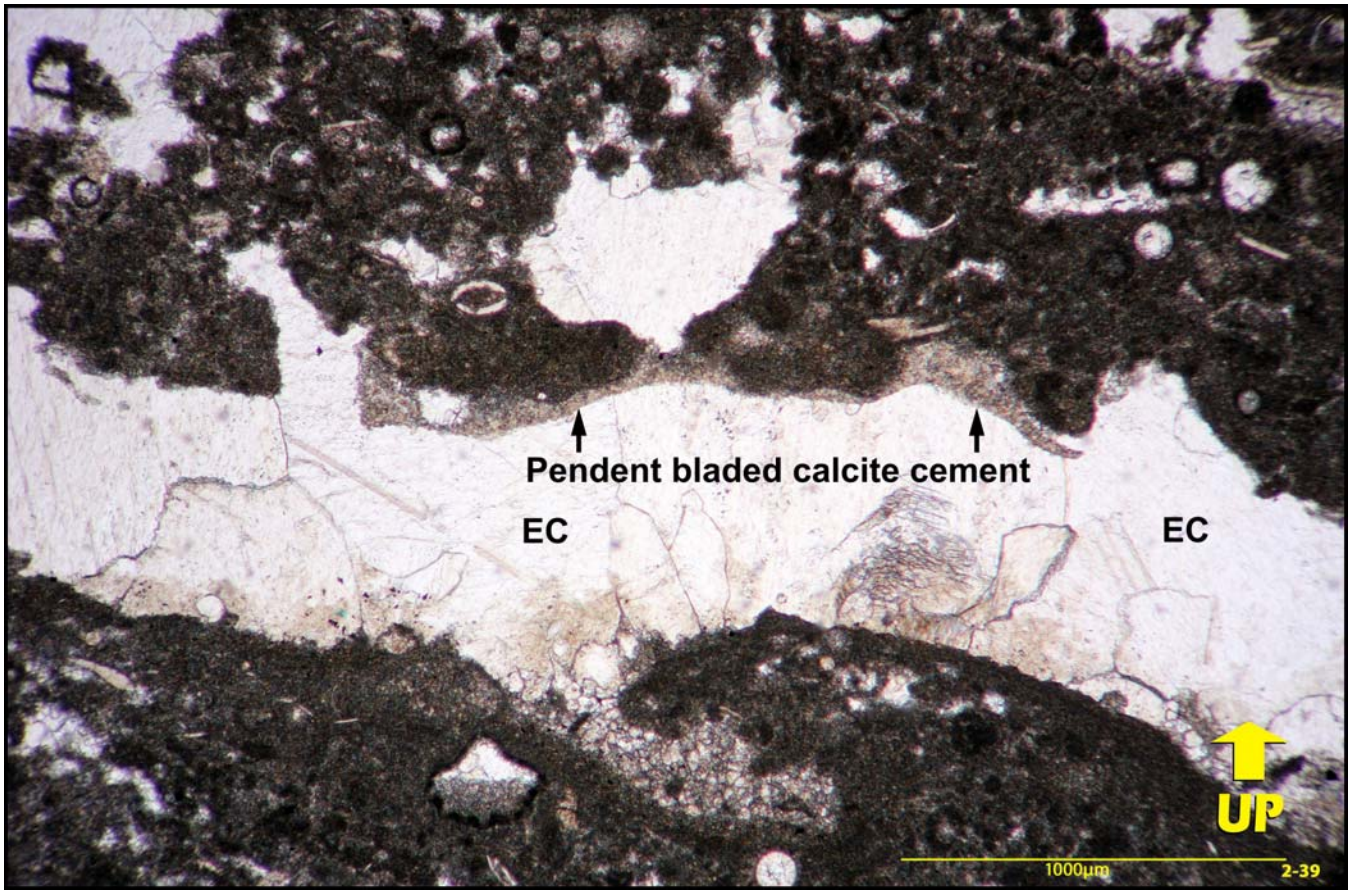

Photomicrograph of a pendent crust consisting of inclusion-rich bladed calcite cement at the top of a laminar fenestrae. Equant crystals of inclusion-lean, clear calcite (EC) infill the remaining fenestral pore. The adjacent limestone matrix is a wackestone containing benthic foraminifera (?), ostracodes and calcispheres. Photomicrograph taken using plane-polarized light. Parker River J-72, 955.05 m.

Figure D7

Core photograph of the cm-scale irregular and horseshoe cavities in a lime mudstone to wackestone. The cavities are infilled by very fine sand to granule-size particles consisting of single crystals of sparry calcite; very coarse sand to granule size bodies of subspherical and elongate shapes consisting of an outer rim and an interior consisting of a mosaic of sparry calcite crystals; and a very fine (mud to fine silt-size) replacive dolomite. Photograph taken of a wetted core surface. Parker River J-72, 954.20 m.

Figure D8

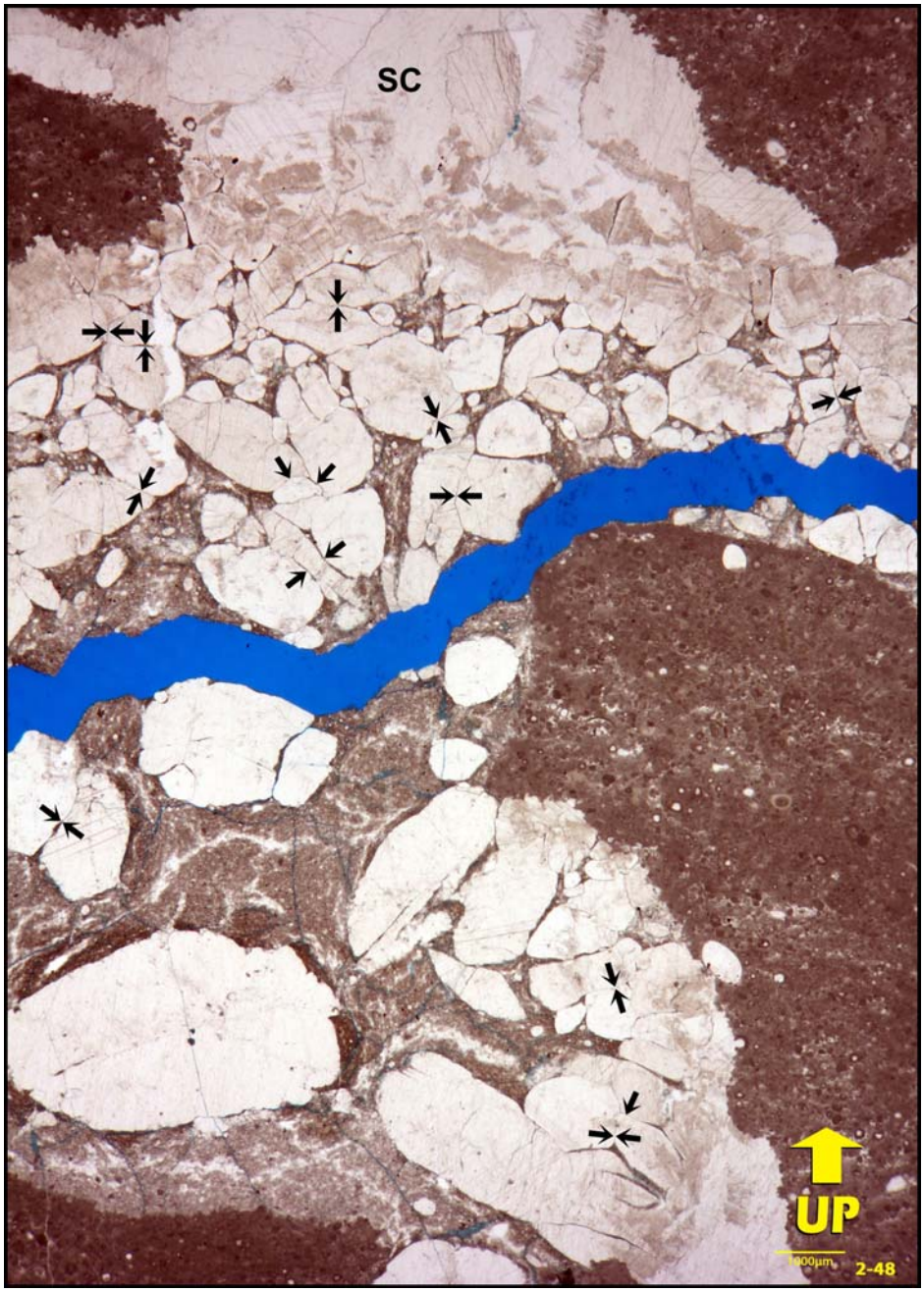

Photomicrograph, taken using a binocular microscope, of an irregular-shaped cavity approximately 0.5 m below the horseshoe-shaped cavity illustrated in Figure D7. The infill of the lower to intermediate part of the cavity consists of coarse sand to granule-size particles that consist of a single crystal of sparry calcite and intervening mud to fine silt-size replacive dolomite. Note that many of these particles occur in clumps where the individual particles fit very closely together (arrows). This suggests the formation is from the partial break-up of an organism whose bodies or walls consisted of a crystalline mosaic of odd-shaped crystals of sparry calcite of variable sizes. Sparry calcite cement (SC) infills the upper portion of the cavity and replaces portions of adjacent particles. Transmitted plane-polarized light. Parker River J-72, 954.74 m.

Figure D9

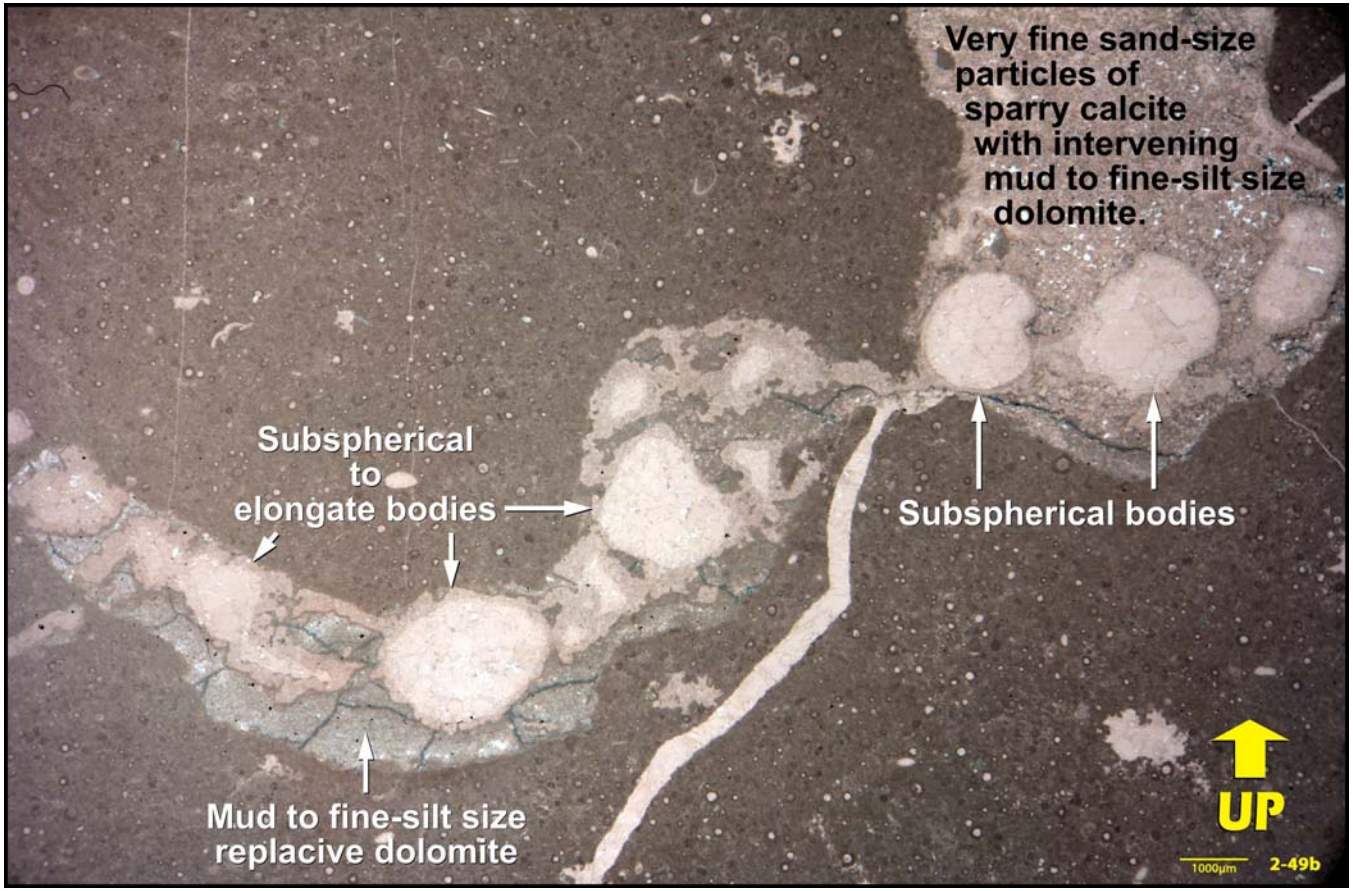

Photomicrograph, taken using a binocular microscope, of the lower portion of the horseshoe-shaped cavity illustrated in the core photograph in Figure D7. The left and right sides of the cavity are reversed from that shown in Figure D7. The lower two-thirds of the portion of the cavity shown in this figure contain mainly very coarse sand to granule-size, subspherical to elongate bodies with an outer calcite wall and an interior consisting of a mosaic of sparry calcite crystals. The upper one-third of the portion of the cavity shown in this figure contains very coarse sand-size bodies of subspherical shapes with an outer calcitic wall and an interior consisting of a mosaic of sparry calcite crystals. Very fine sand-size particles consisting of single crystals of sparry calcite occur between and overlie these coarser subspherical bodies. Very fine (mud to fine-silt size) replacive dolomite occurs adjacent to and between all the coarser particles and bodies illustrated in this photomicrograph. Transmitted plane-polarized light. Parker River J-72, 954.24 m.

Figure D10

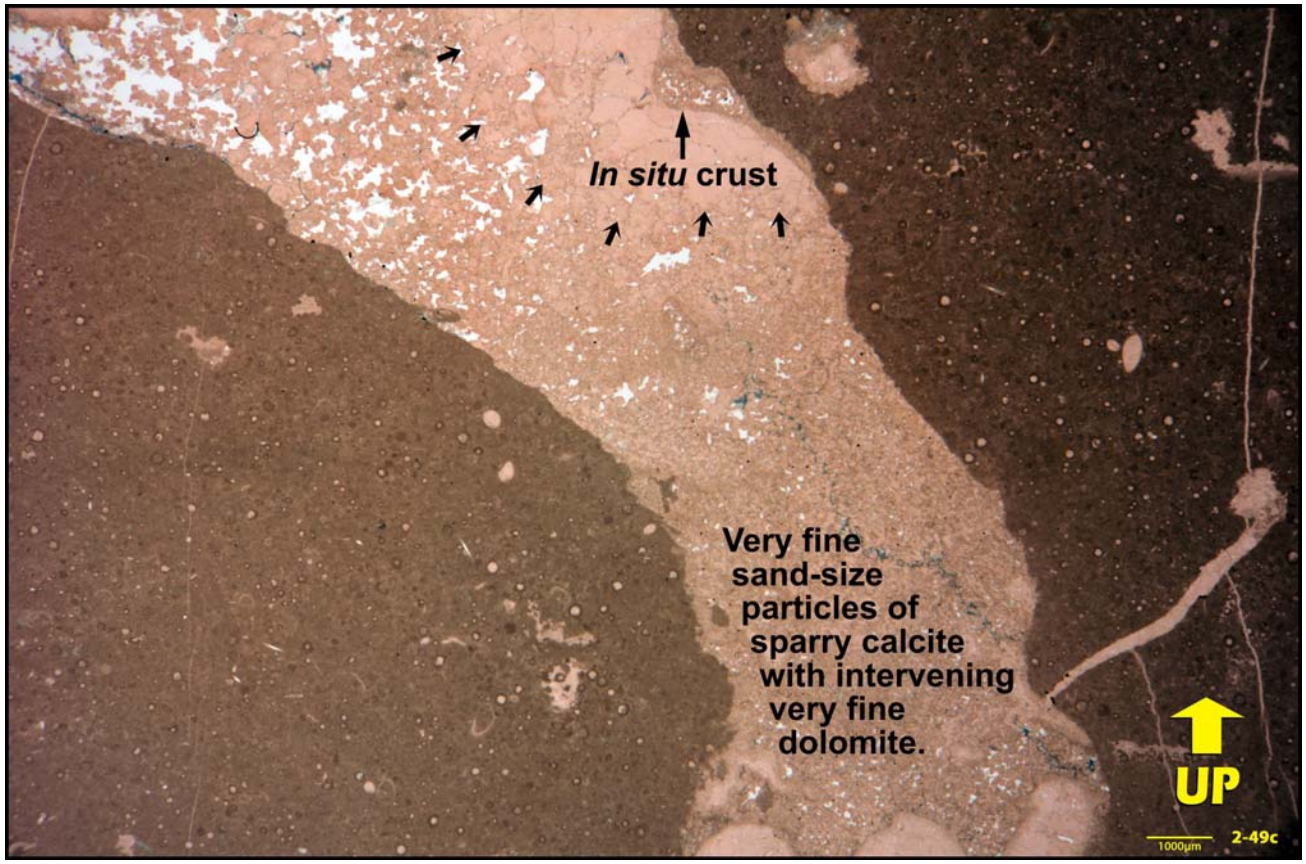

Photomicrograph, taken using a binocular microscope, of the intermediate and some of the upper portion of the horseshoe-shaped cavity illustrated in the core photograph in Figure D7. The left and right sides of the cavity are reversed from that shown in Figure D7. The basal portion of the photomicrograph overlaps the upper portion of the photomicrograph shown in Figure D9. The intermediate portion of the cavity consists of very fine sand-size particles of single crystals of sparry calcite and intervening very fine (mud to fine-silt size) replacive dolomite. The upper right side of the cavity consists of a mosaic of crystals of sparry calcite (arrows) which appears to have been partly broken apart and an *in situ* crust consisting of finer sparry calcite crystals. Both these elements are interpreted to be largely intact portions of an organism of unknown affinity that has mainly decomposed and undergone various stages of break-up within a dwelling burrow. The break-up of the mosaic of sparry calcite crystals may be the source of the coarse particles of sparry calcite within the burrow cavity illustrated in Figure D8. White patches in the upper left portion of the photomicrograph are due to plucking during thin-section preparation. Transmitted plane-polarized light. Parker River J-72, 954.24 m.

Figure D11

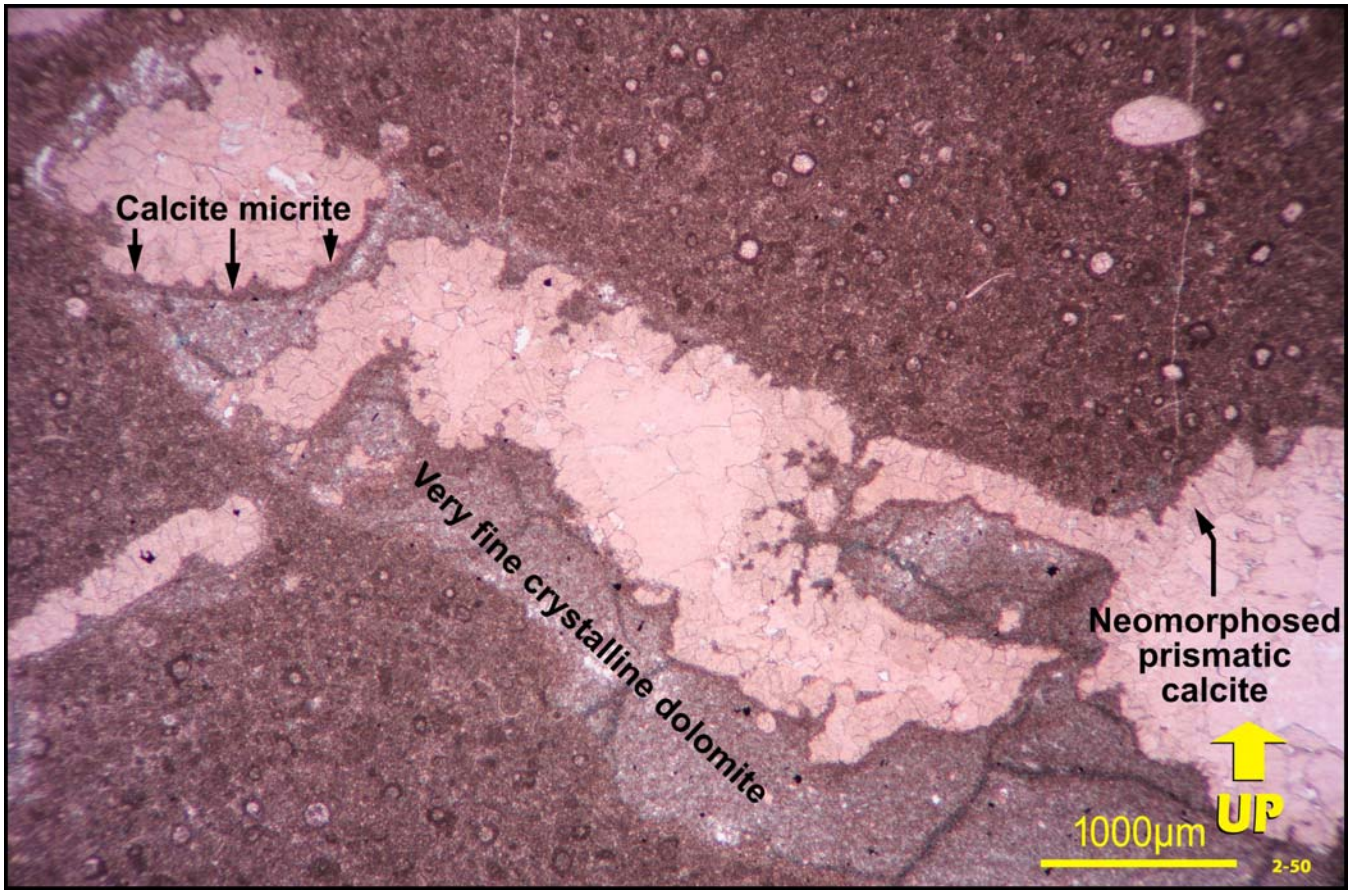

Photomicrograph of a higher magnification view of the lower part of the horseshoe-shaped cavity illustrated in Figure D9. The subspherical and elongate bodies have serrated margins consisting of both neomorphosed prismatic (bladed) calcite and calcitic micrite. The interior of the bodies consist of a mosaic of sparry calcite crystals. These bodies are interpreted to be the intact remains of an organism of unknown affinity that lived in the burrow. The associated micritic internal sediment in the burrow has been replaced by a very fine (mud to fine-silt size) crystalline dolomite. Photomicrograph taken using plane-polarized light. Parker River J-72, 954.24 m.

Figure D12

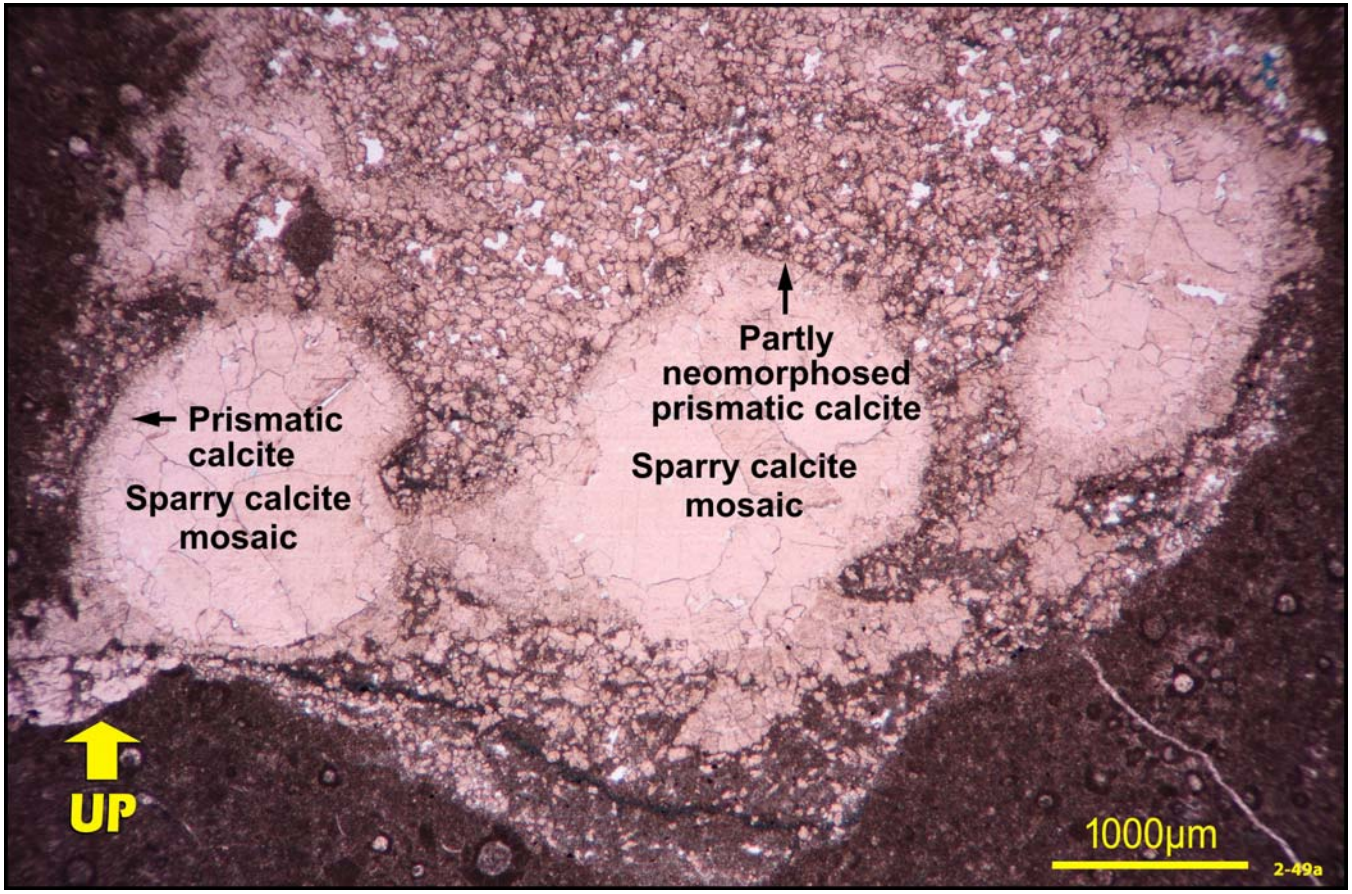

Photomicrograph of a higher magnification view of the portion of the cavity illustrated in the upper right portion of Figure D9. The subspherical bodies on the left side of the photomicrograph appear to be joined through a narrow connection. All three subspherical bodies have an outer wall consisting of prismatic calcite or partly neomorphosed prismatic calcite. The interior of these bodies consist of a mosaic of sparry calcite crystals. These bodies are also interpreted to be the intact remains of the organism of unknown affinity that lived in the burrow. The associated and overlying very fine sand-size particles, consisting of single crystals of sparry calcite, have a clastic texture. The matrix between these particles and at the base of the burrow cavity consists of very fine (mud to fine-silt size) crystalline dolomite. Photomicrograph taken using plane-polarized light. Parker River J-72, 954.24 m.

Figure D13

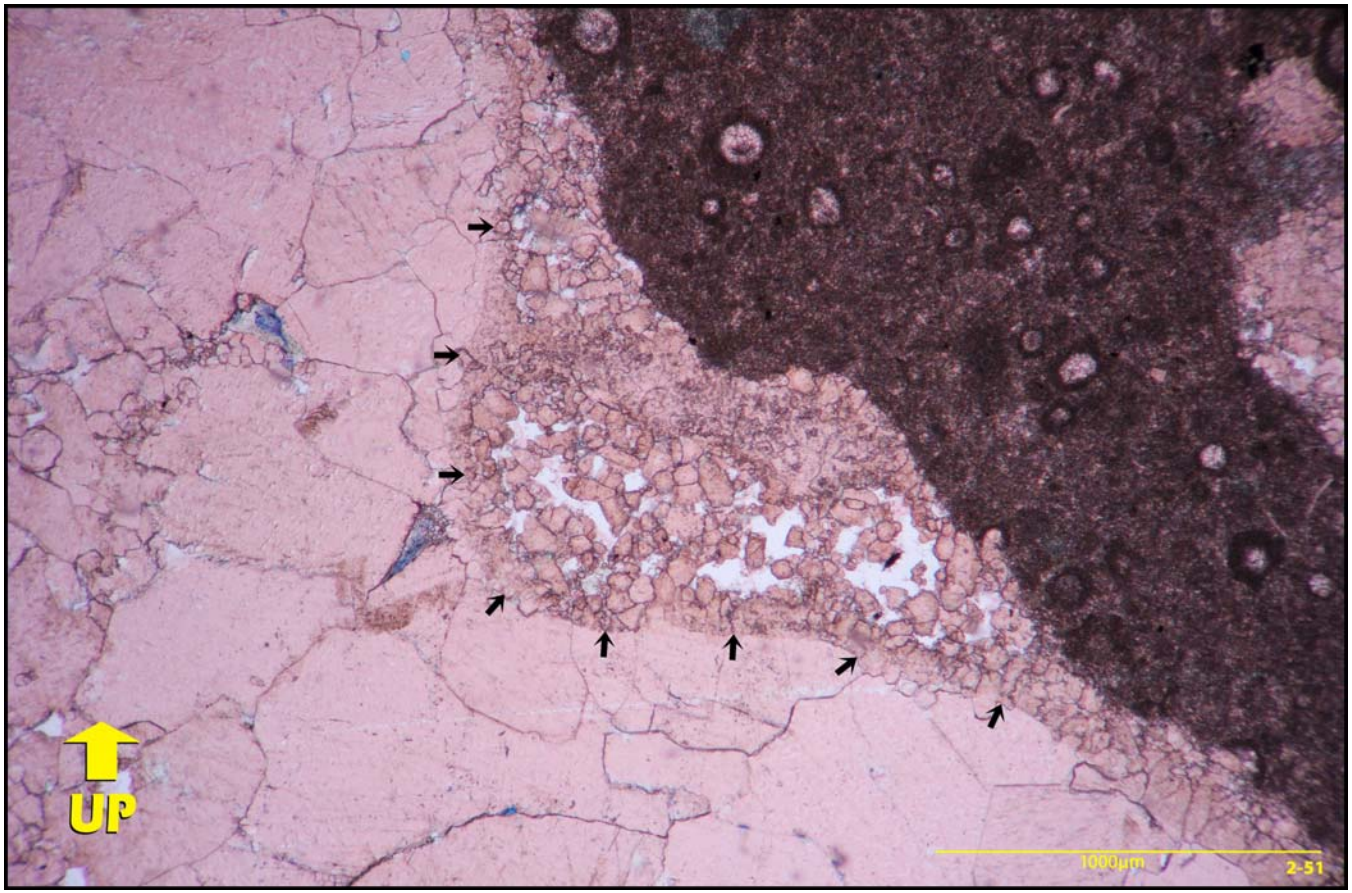

Photomicrograph showing a higher magnification view of the in situ crust (arrows) along the wall of the burrow cavity illustrated in Figure D10. The crust consists of a mosaic of very fine sand-size crystals of sparry calcite with curved margins. The breakdown of crusts like this may be the source of the dominantly clastic accumulation of very fine sand-size particles of sparry calcite lower in the cavity (Figures D10 and D12). White patches are from plucking during the preparation of the thin section. Photomicrograph taken using plane-polarized light.
Parker River J-72, 954.24 m.

Figure D14

Core photograph of a dolorudstone consisting of laminar stromatoporoids (LS) and thicker tabular stromatoporoids (TS), as well as fragments of stromatoporoids with either uncertain or unknown growth forms. This sample has a measured porosity of 9.3% and a K_{max} of 1.37 mD. Photograph taken of a wetted core surface. Parker River J-72, 1004.81 m (Full Diameter Piece 9).

Figure D15

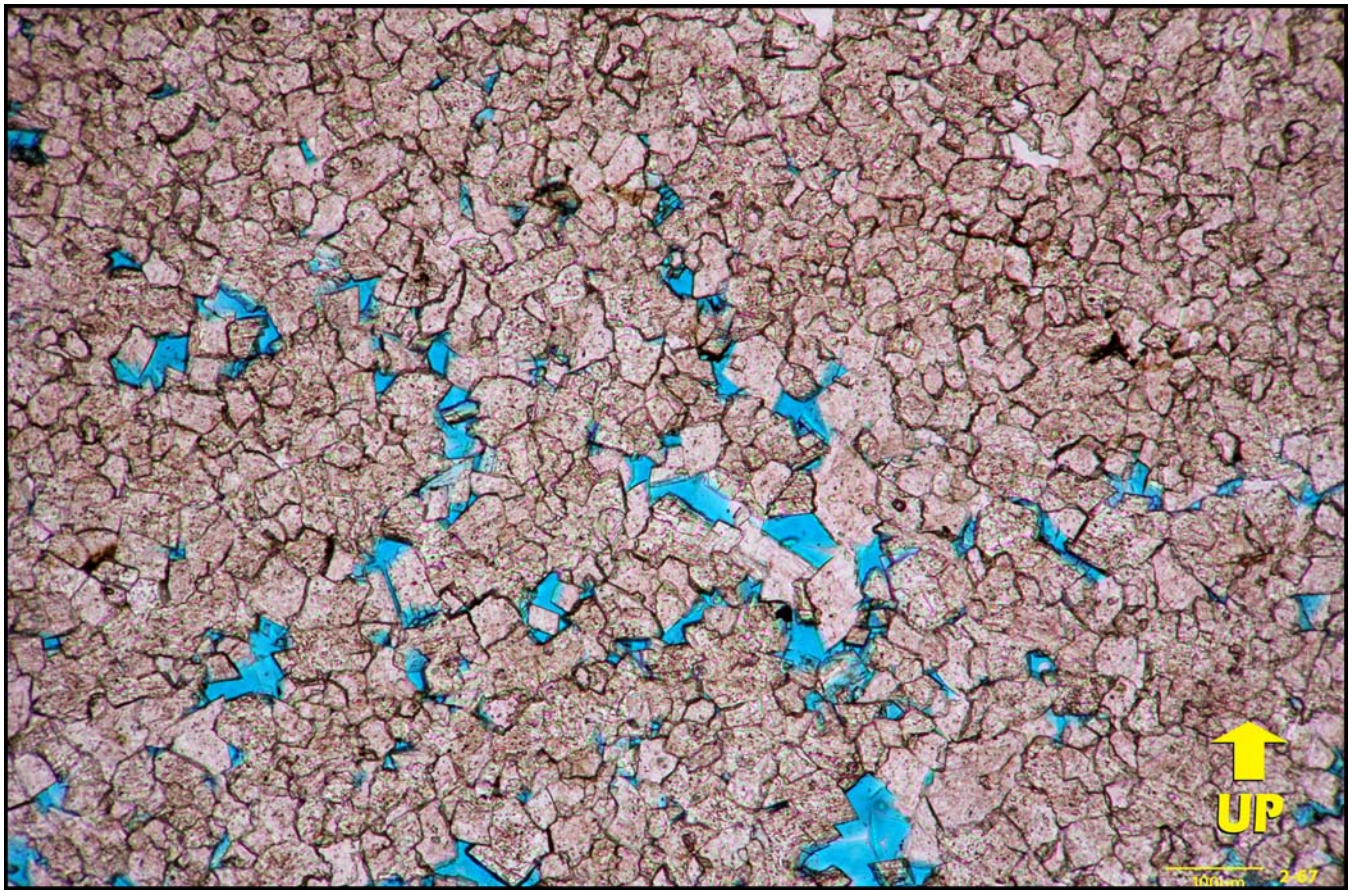

Photomicrograph of the high-porosity interval in a full diameter segment which has a measured porosity of 5.7% and a K_{max} of 0.83 mD. The dolomite consists of very fine sand-size crystals with textures ranging from planar-s to nonplanar-a. Intercrystalline pores, impregnated by blue epoxy, occur between the dolomite crystals. Photomicrograph taken using plane-polarized light. Parker River J-72, 1002.89 m (Full Diameter Piece 3).

Figure D16

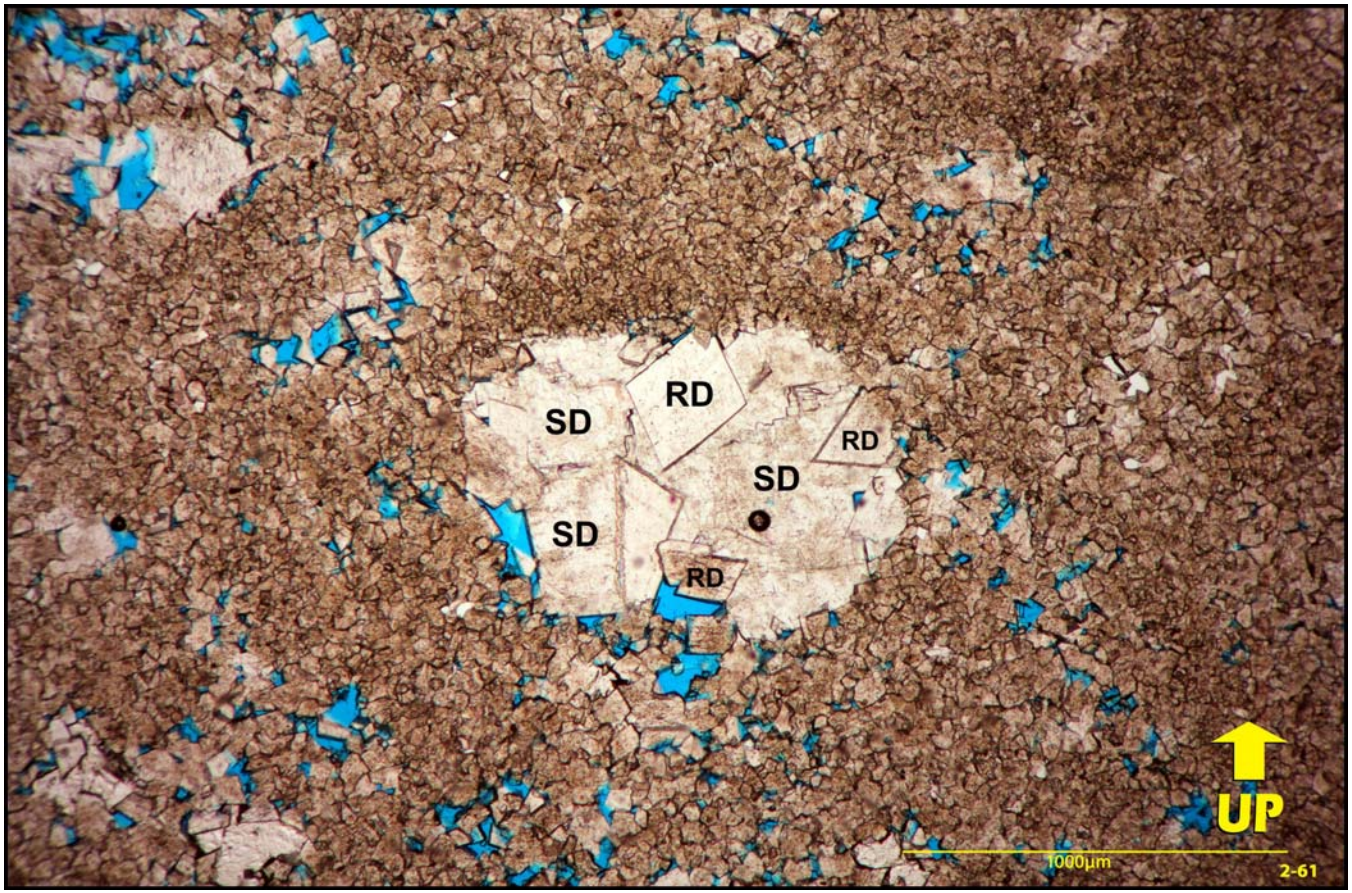

Photomicrograph illustrating a small vug in a very fine sand-size dolomite with planar-s to nonplanar-a textures. The vug is appreciably infilled by rhombic dolomite crystals (RD) followed by coarser crystals of saddle dolomite (SD). The full-diameter segment from which this sample was taken has a measured porosity of 5.5% and a K_{max} of 0.36 mD. Photomicrograph taken using plane-polarized light. Parker River J-72, 1003.96 m (Full Diameter Piece 6).

Figure D17

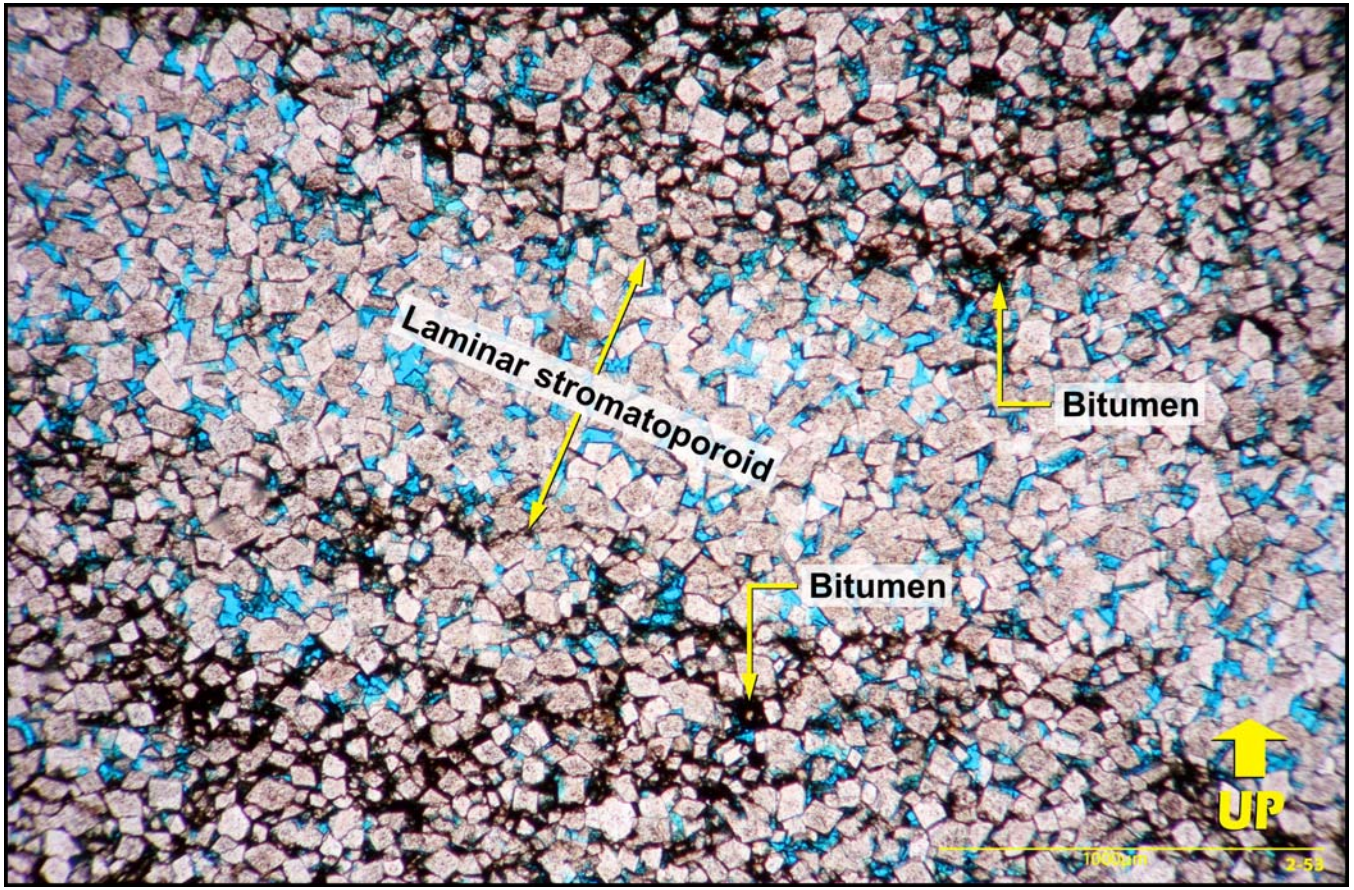

Photomicrograph illustrating good intercrystalline porosity between dolomite crystals, within a dolomite replacing a laminar stromatoporoid. Bitumen commonly infills intercrystalline pores in the dolomite both above and beneath the replaced stromatoporoid. The dolomite illustrated in this photomicrograph consists of very fine to fine sand-size crystals with planar-s textures (approaching planar-e in certain positions). The full-diameter segment from which this sample was taken has a measured porosity of 9.3% and a K_{max} of 1.37 mD. Photomicrograph taken using plane-polarized light. Parker River J-72, 1004.78 m (Full Diameter Piece 9).

Figure D18

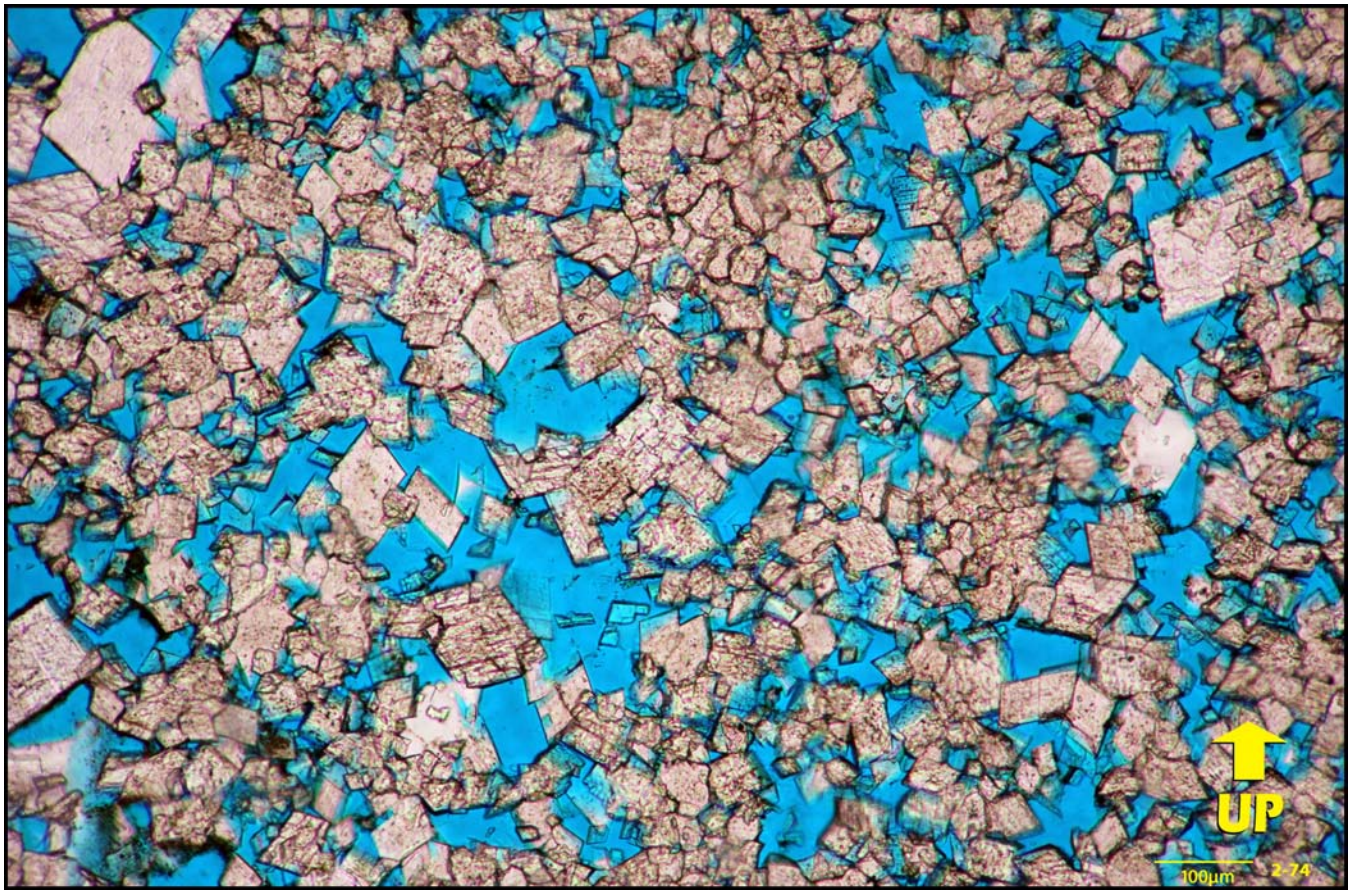

Photomicrograph of the dolomite in the full-diameter core piece with the highest measured porosity (13.8%) and K_{max} (50.40 mD) in this core interval. The sample contains excellent intercrystalline porosity between the dolomite rhombs. The dolomite consists of very fine to fine sand-size crystals with planar-s textures (approaching planar-e in certain positions). Photomicrograph taken using plane-polarized light. Parker River J-72, 1002.29 m (Full Diameter Piece 1).

Figure D19

Core photograph illustrating large vugs of dissolution origin, partly infilled by crystals of saddle dolomite (SD), in a dolostone. This core core piece is from the full-diameter segment that has the highest measured porosity (13.8%) and K_{max} (50.40 mD) of any interval in the well. The large vugs are interpreted to be a major contributor to the high permeability. Photograph taken of a wetted core surface.
Parker River J-72, 1002.16 m (Full Diameter Piece 1).

Figure D20

Core photograph illustrating patchy zebroids with horizontal to subhorizontal internal orientations. The core contains some open zebroid pores, partially infilled by crystals of white saddle dolomite, as well as some open dissolution vugs (V). This core interval has a measured porosity of 5.7% and a K_{max} of 0.83 mD. Photograph taken of a wetted core surface. Muskox D-87, 2087.15 m (Full Diameter Piece 37).

Figure D21

Core photograph of bed parallel zebroids, with some open pores in the zebroids. Note bitumen infilling a narrow subvertical fracture. Photograph taken of a wetted core surface. Muskox D-87, 2084.50 m.

Figure D22

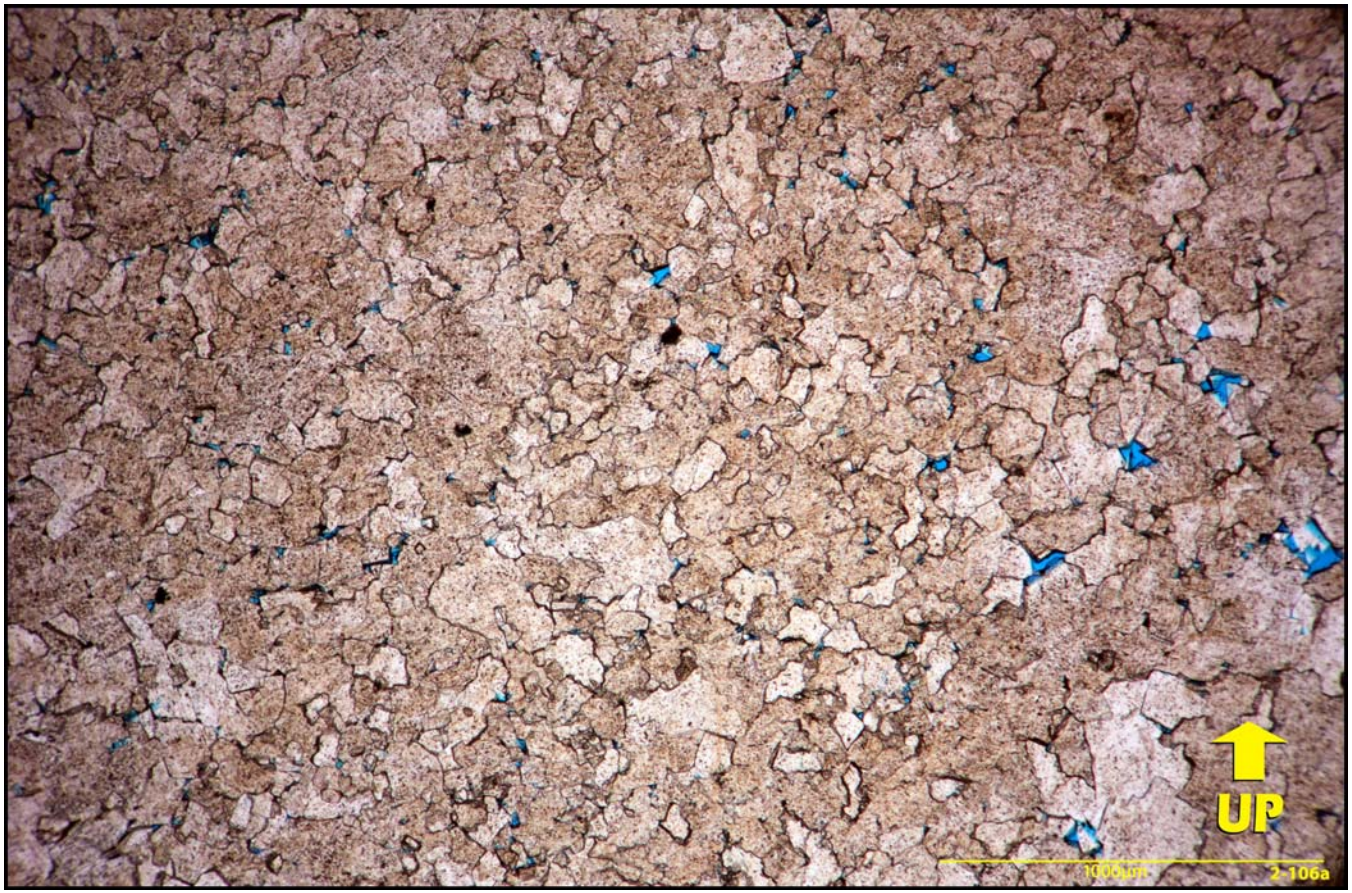

Photomicrograph illustrating a dolomite with fine to medium sand-size crystals and nonplanar-a textures. This sample has only minor intercrystalline porosity. Photomicrograph taken using plane-polarized light. Muskox D-87, 2075.70 m.

Figure D23

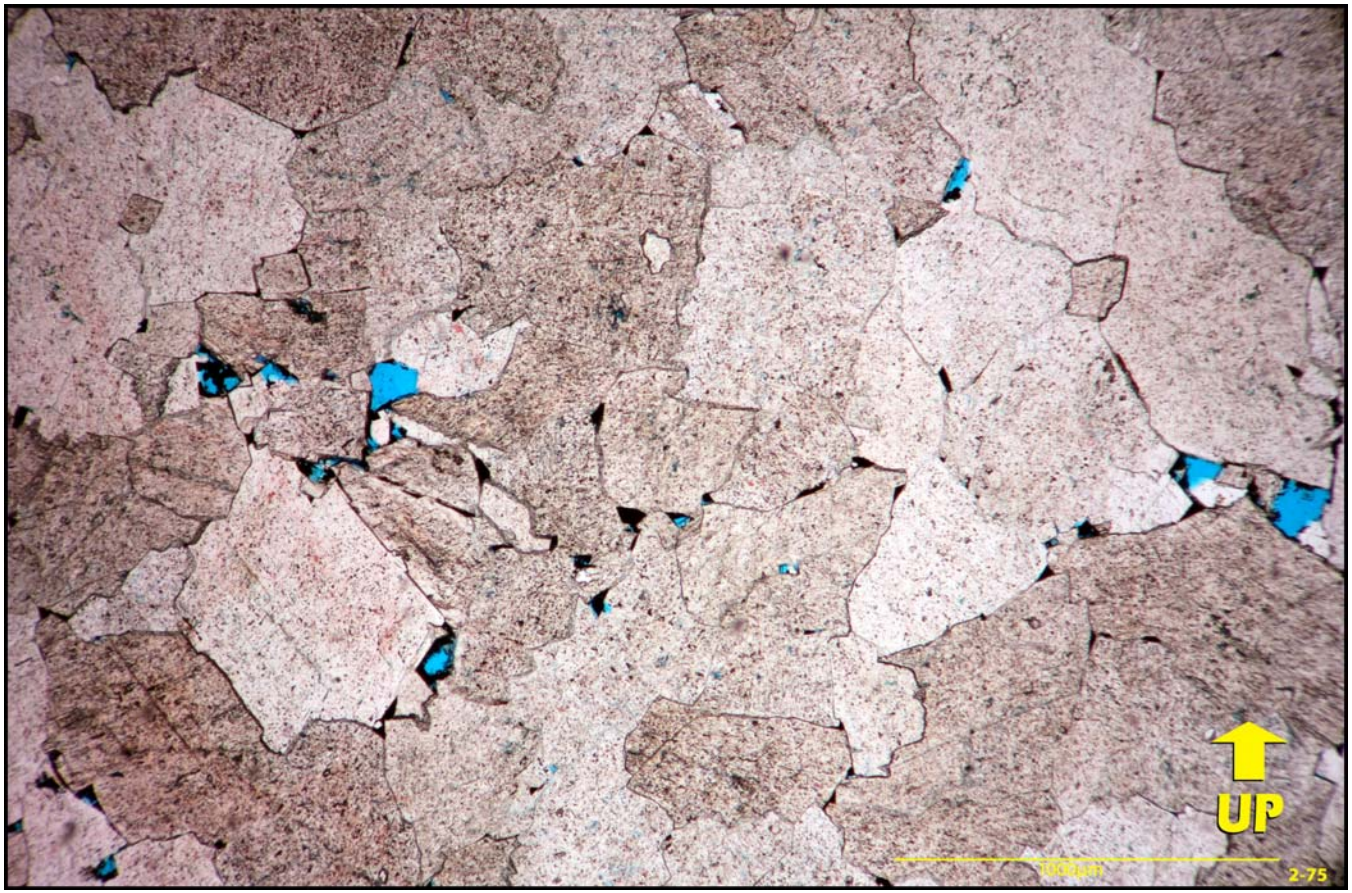

Photomicrograph of a coarse sand-size crystalline dolomite with nonplanar-a crystal textures. The sample has only minor intercrystalline porosity. Photomicrograph taken using plane-polarized light. Muskox D-87, 2090.88 m.

Figure D24

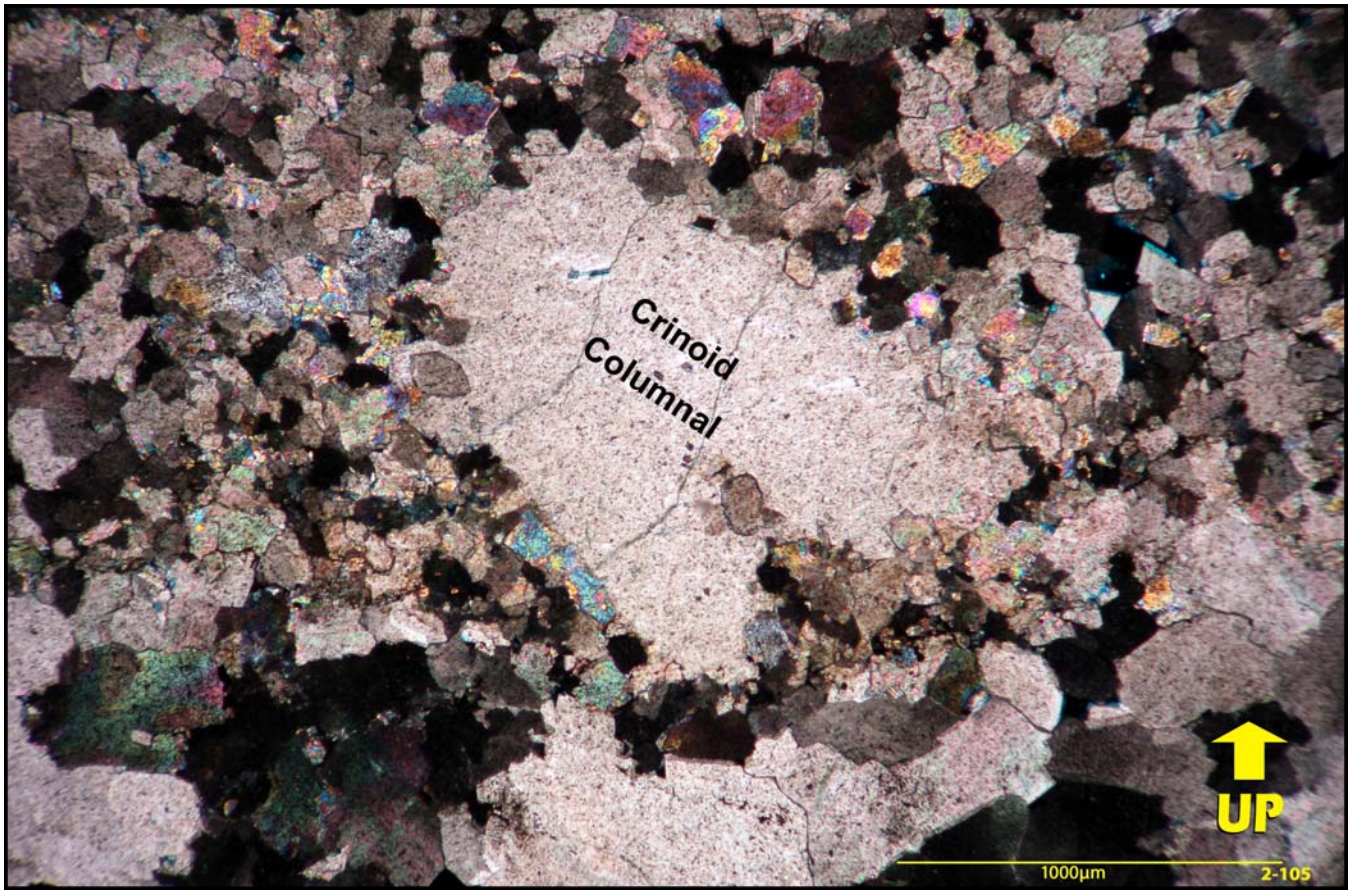

Photomicrograph of a solitary, very coarse sand-size dolomite crystal replacing a crinoid columnal. Photomicrograph taken using cross-polarized light. Muskox D-87, 2075.70 m.

Figure D25

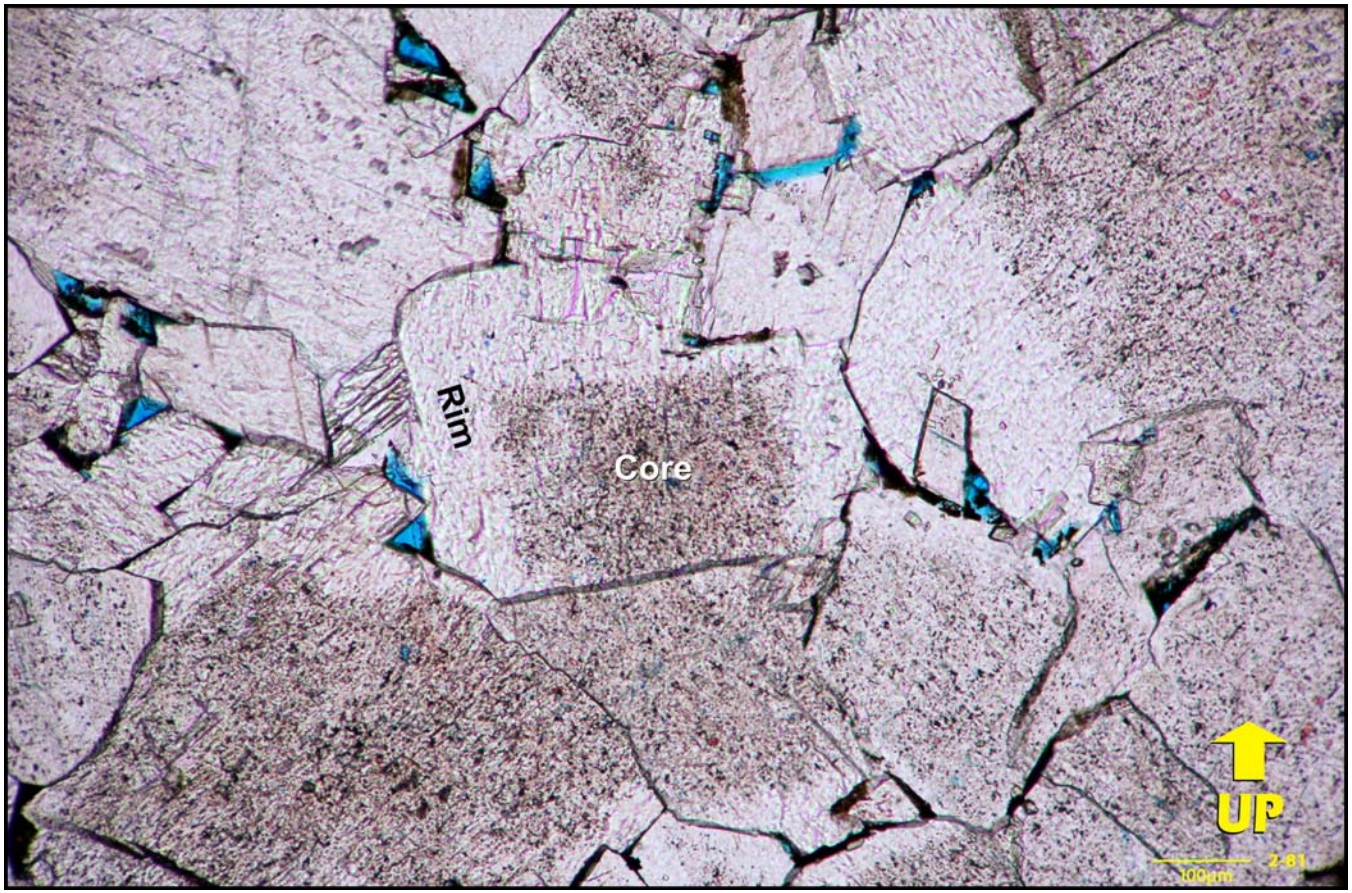

Photomicrograph of matrix dolomite crystals with an inclusion-rich core and a clear inclusion-lean outer rim. The inclusion-lean rims face open intercrystalline pores. Photomicrograph taken using plane-polarized light. Muskox D-87, 2089.75 m.

Figure D26

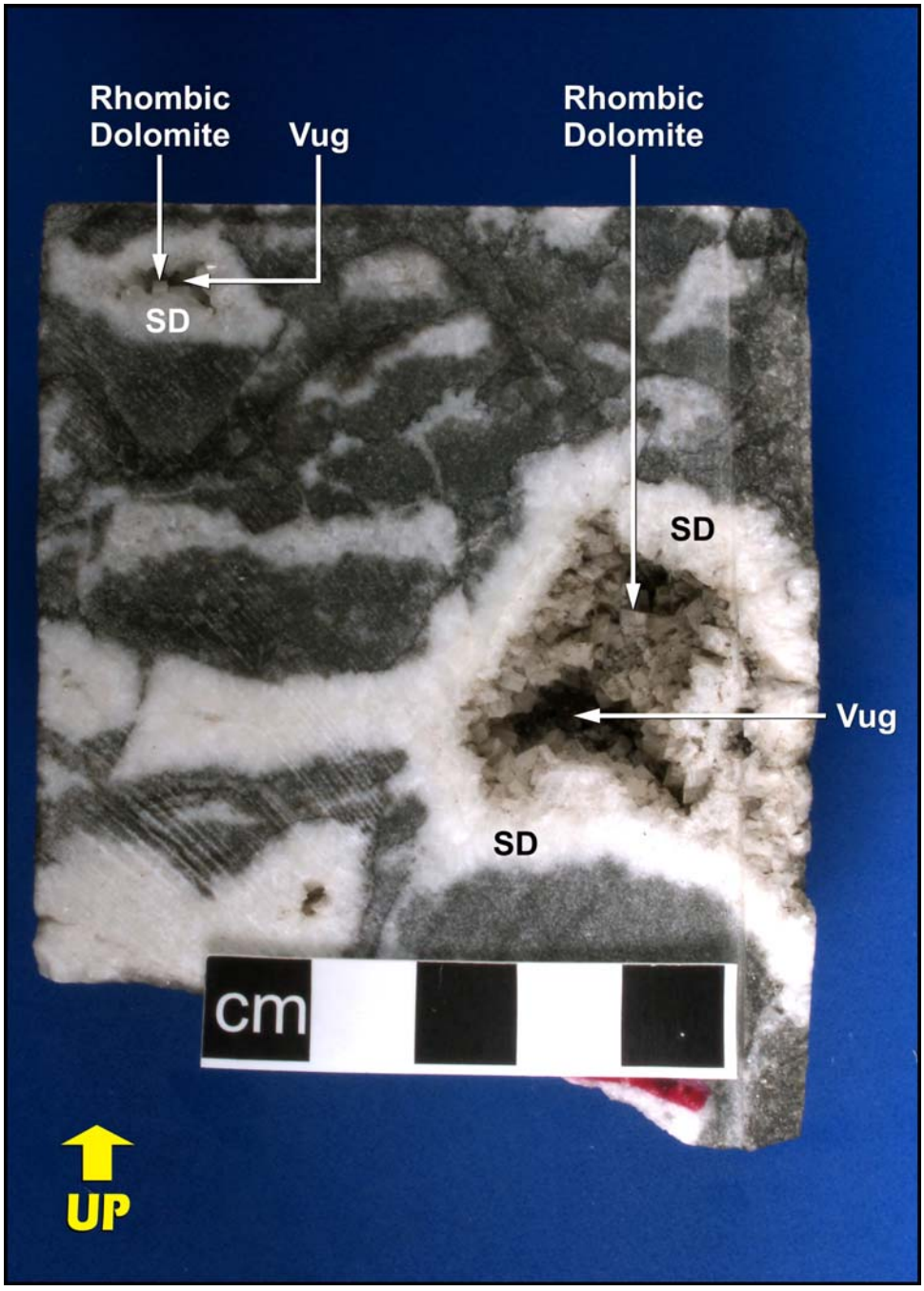

Core photograph of discrete vugs of dissolution origin. The vugs are lined by white saddle dolomite crystals (SD), which are overgrown by smaller translucent crystals of rhombic dolomite. The interior of the vugs remain open. Photograph taken of a dry core surface. Muskox D-87, 2081.17 m.

Figure D27

Core photograph of channel-form solution vugs with horizontal and oblique orientations. The peripheral portions of the vugs are infilled by white crystals of saddle dolomite, but the interior portions remain open. This full-diameter core segment has a porosity of 2.2% and a K_{max} of 0.26 mD. Photograph taken of a wetted core surface. Muskox D-87, 2081.60 m.

Figure D28

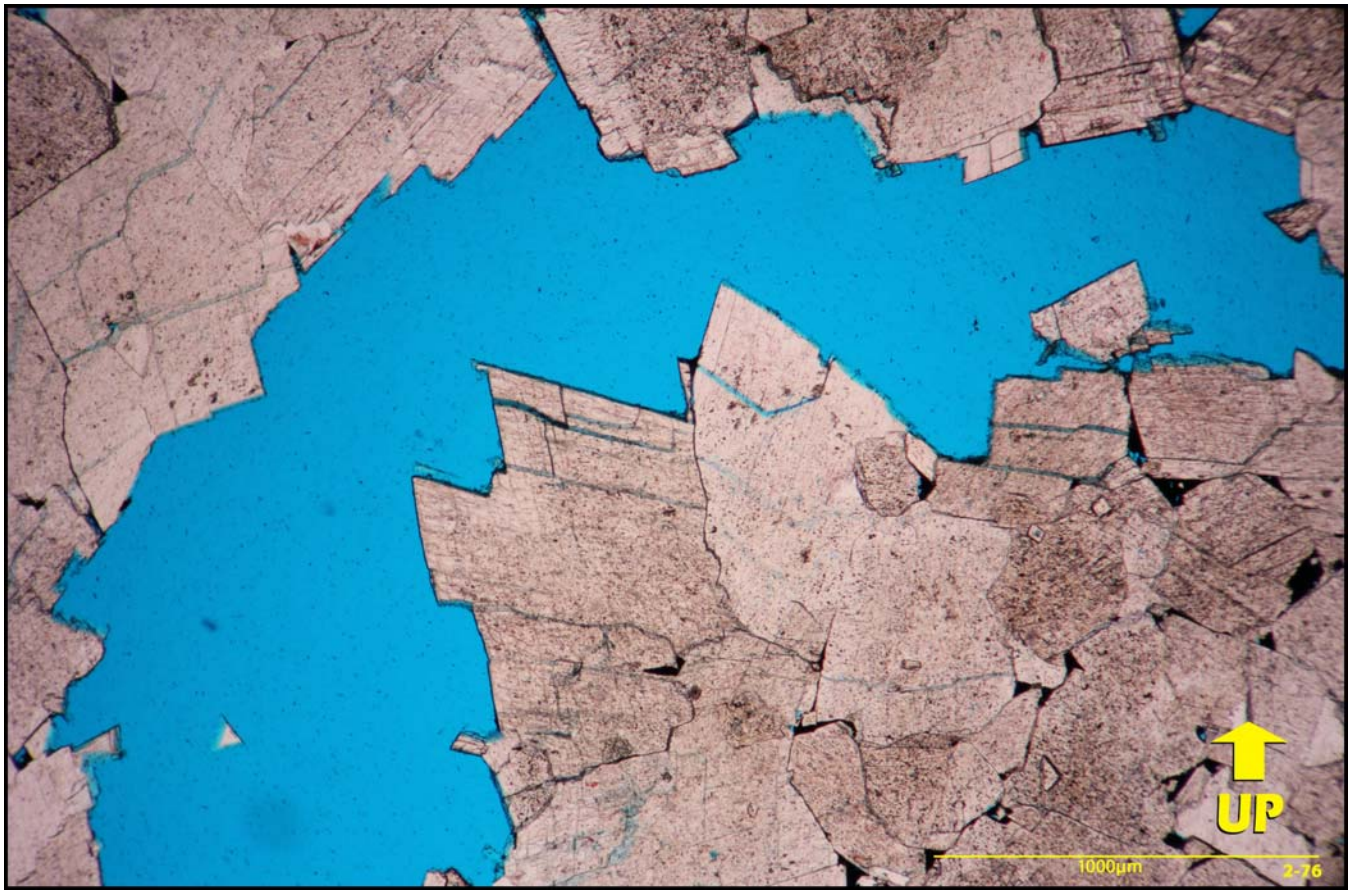

Photomicrograph showing crystals of saddle dolomite partially infilling a solution vug. The crystals have stepped curved faces. Photomicrograph taken using plane-polarized light. Muskox D-87, 2090.88 m.

Figure D29

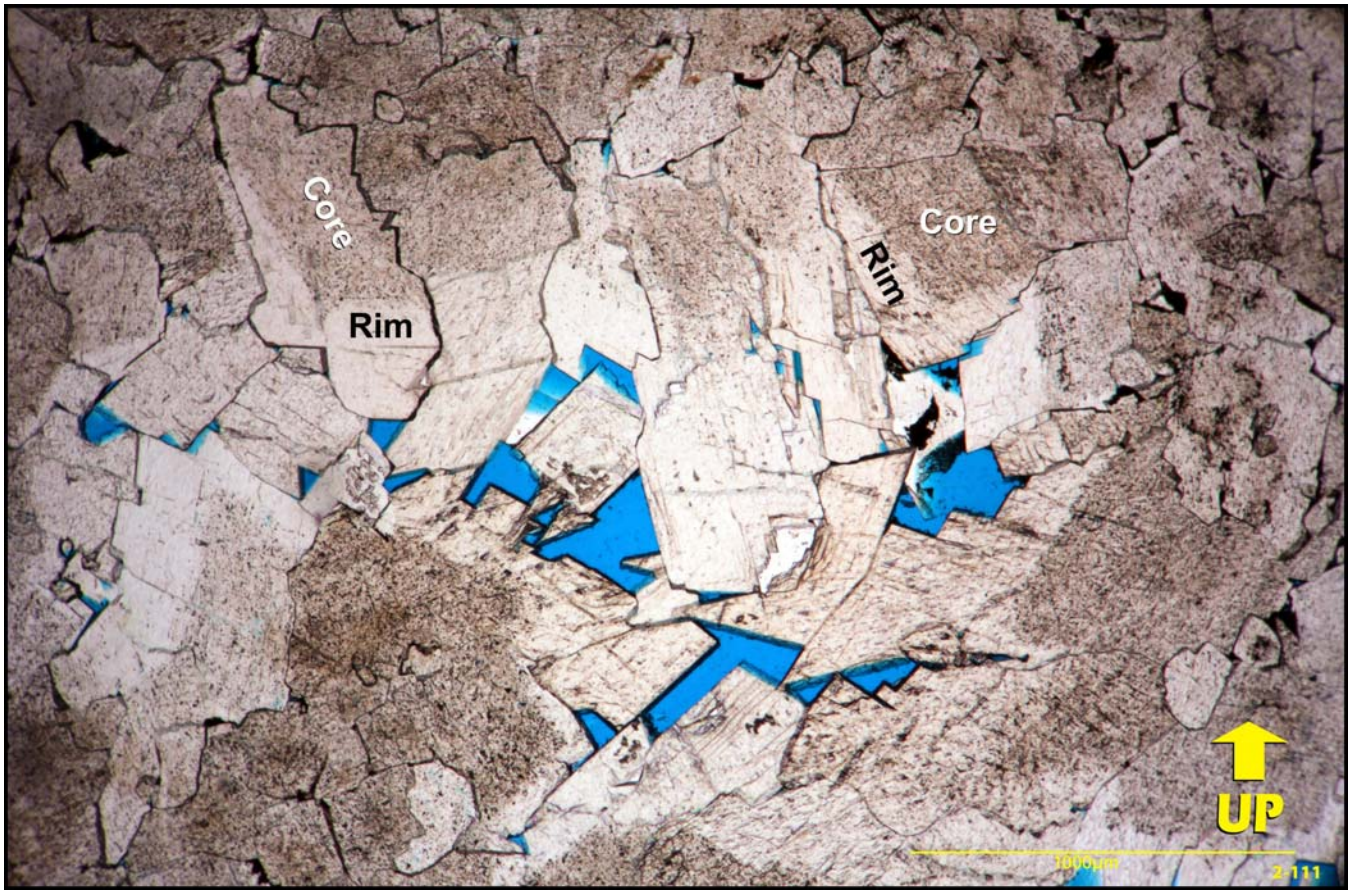

Photomicrograph of crystals of saddle dolomite growing into a zebroid pore. The crystals have an inclusion-rich core and an outer inclusion-lean clear rim. Photomicrograph taken using plane-polarized light. Muskox D-87, 2073.76 m.

Figure D30

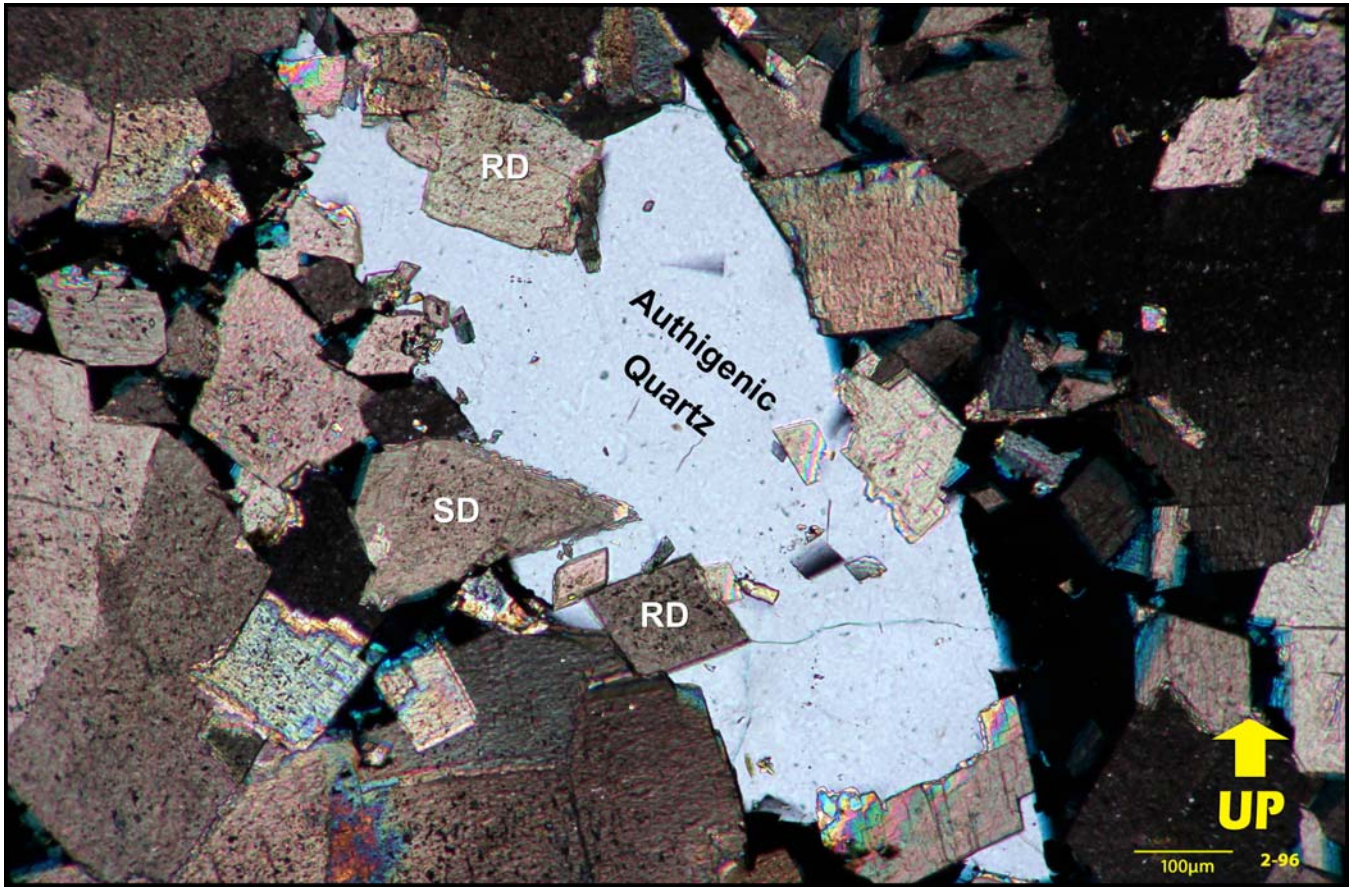

Photomicrograph of an authigenic quartz crystal overgrowing crystals of both saddle dolomite (SD) and rhombic dolomite (RD) in a small solution vug. Photomicrograph taken using cross-polarized light. Muskox D-87, 2083.91 m.

Figure D31

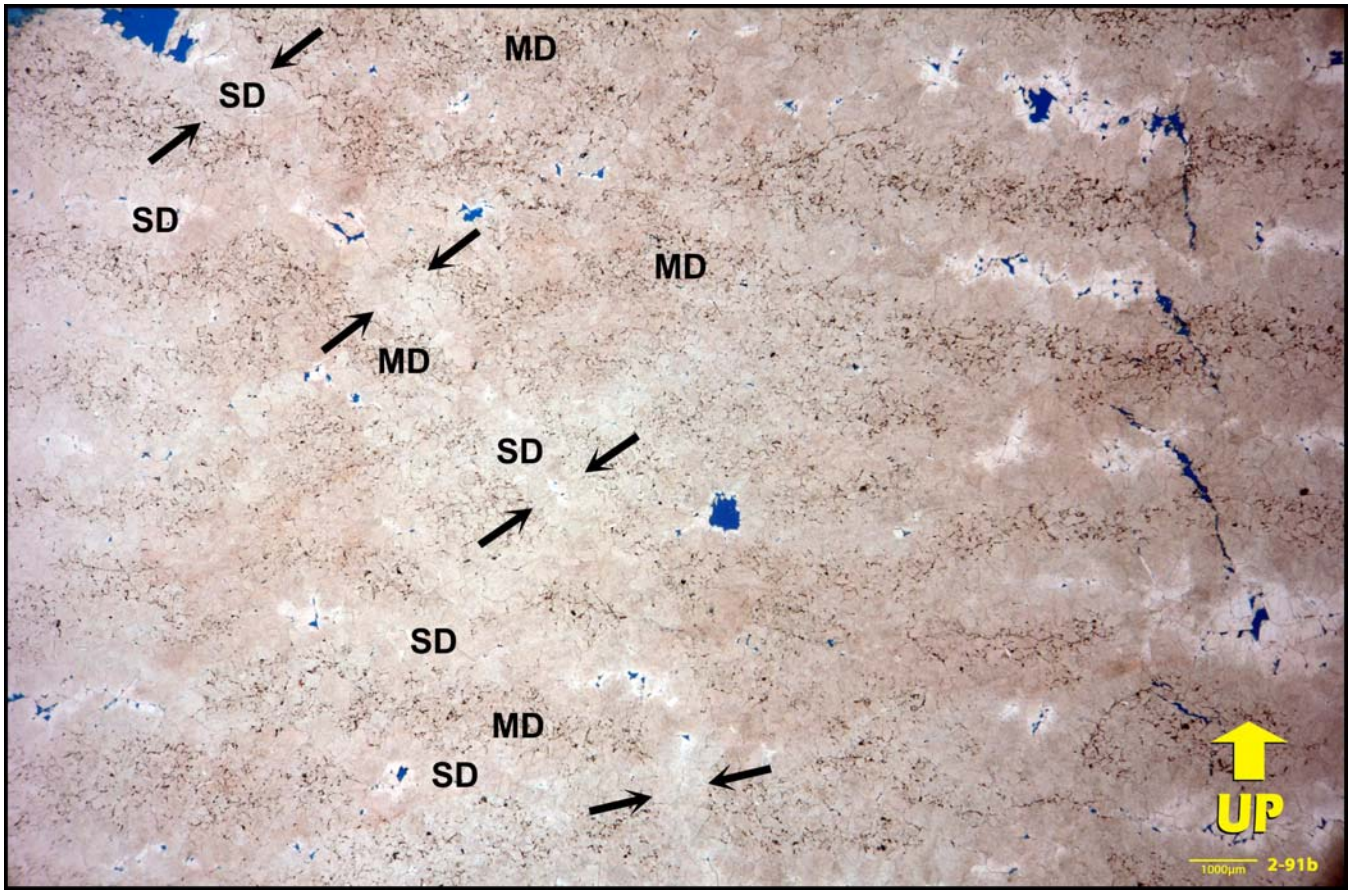

Photomicrograph, taken using a binocular microscope, showing an overview of the relationship between matrix dolomites, bed parallel zebroids, an oblique fracture and saddle dolomite cements. Saddle dolomite (SD) infills both the zebroid pores and the oblique fracture (arrows) cutting both the matrix dolomites (MD) and the zebroids. Transmitted plane-polarized light. Muskox D-87, 2086.38 m.

Figure D32

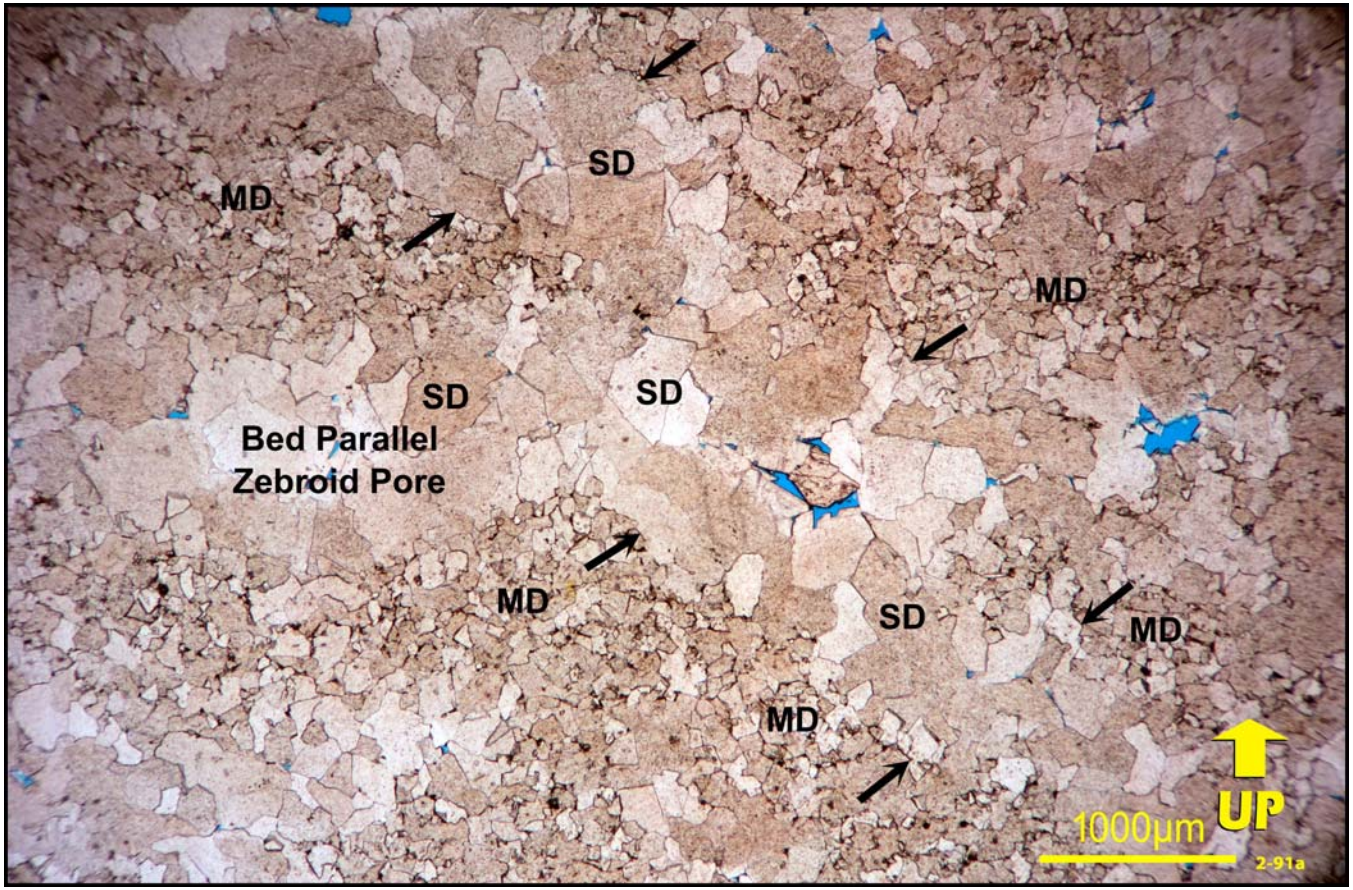

Photomicrograph showing a higher magnification shot of the uppermost left portion of the photo from Figure D31. Saddle dolomite (SD) of the same phase infills both the zebroid pores and the diagonal fracture (arrows) that cuts both the matrix dolomites (MD) and the zebroids. Thus, a hiatus, corresponding to the interval of fracturing, separates the phases of matrix dolomitization and saddle dolomite cementation. Photomicrograph taken using plane-polarized light. Muskox D-87, 2086.38 m.

Figure D33

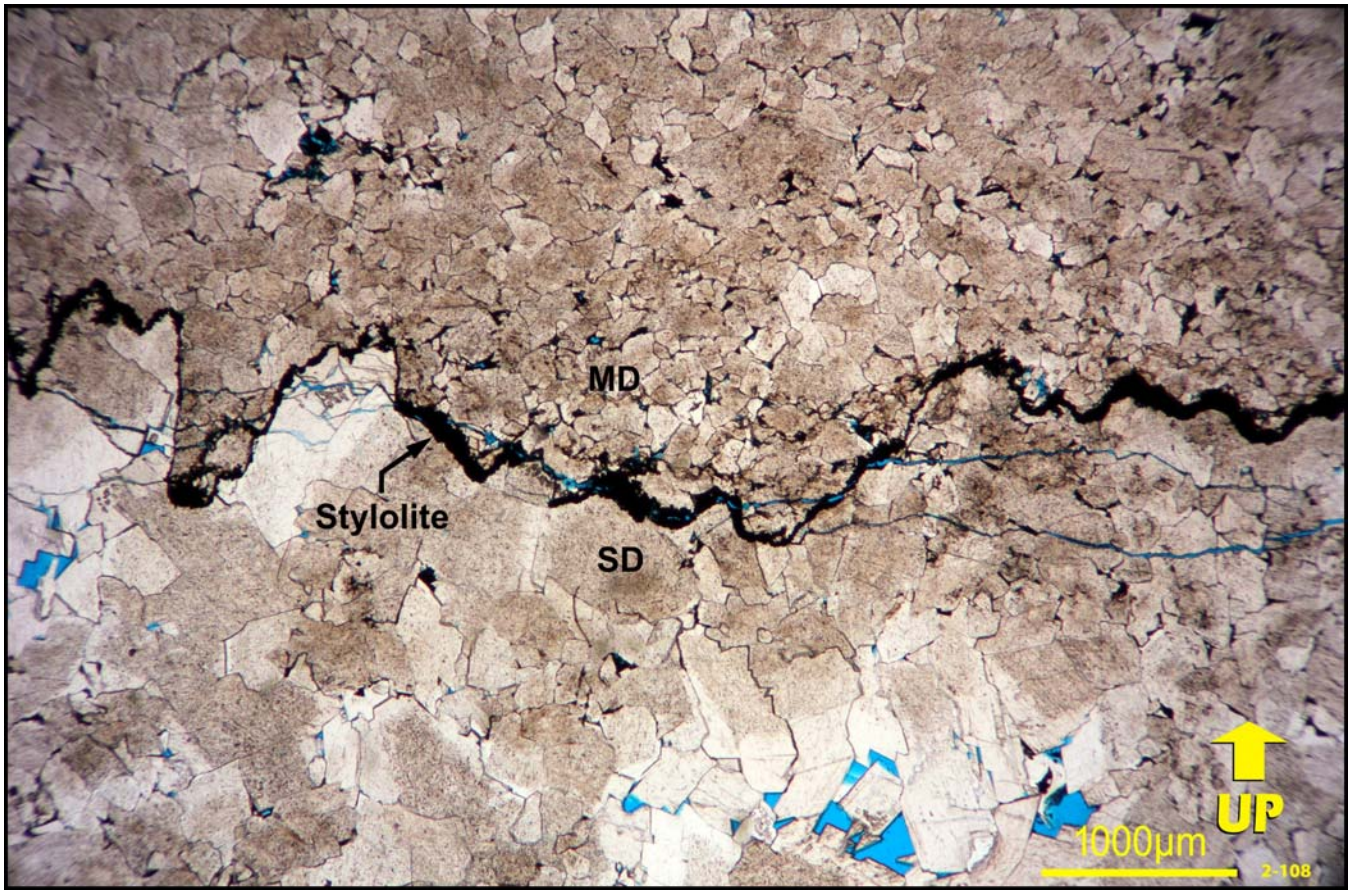

Photomicrograph of a horizontal stylolite cutting both matrix replacement dolomites (MD) and saddle dolomite (SD) infilling a zebroid pore This relationship indicates that the final phase of stylolitization followed both matrix replacement dolomitization and saddle dolomite cementation. Photomicrograph taken using plane-polarized light. Muskox D-87, 2073.76 m.

Figure D34

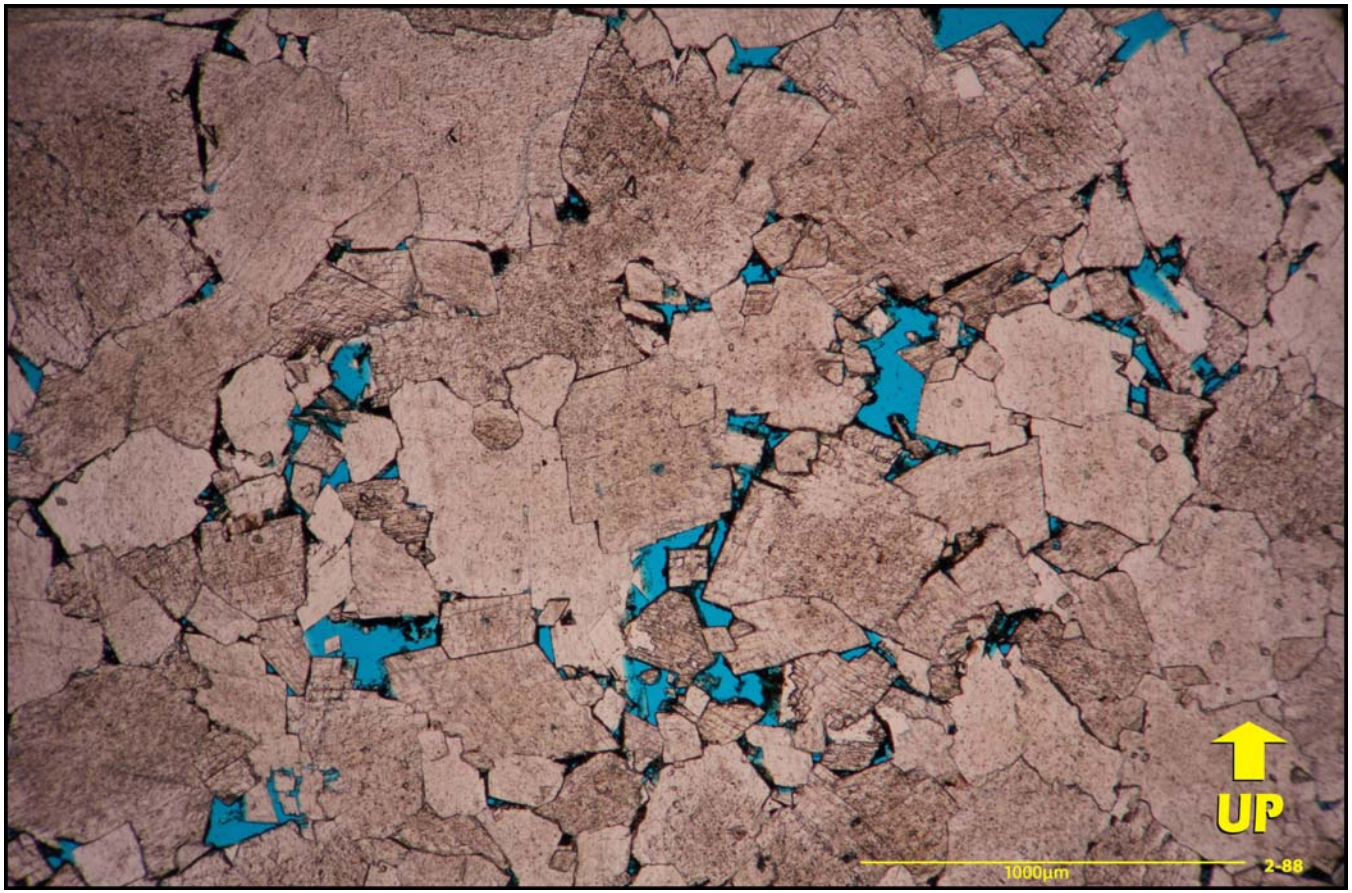

Photomicrograph illustrating intercrystalline pores in a medium to coarse (sand-size) crystalline dolomite. The sample was taken from a full-diameter piece with a measured porosity of 8.5%. Photomicrograph taken using plane-polarized light. Muskox D-87, 2088.61 m.

Figure D35

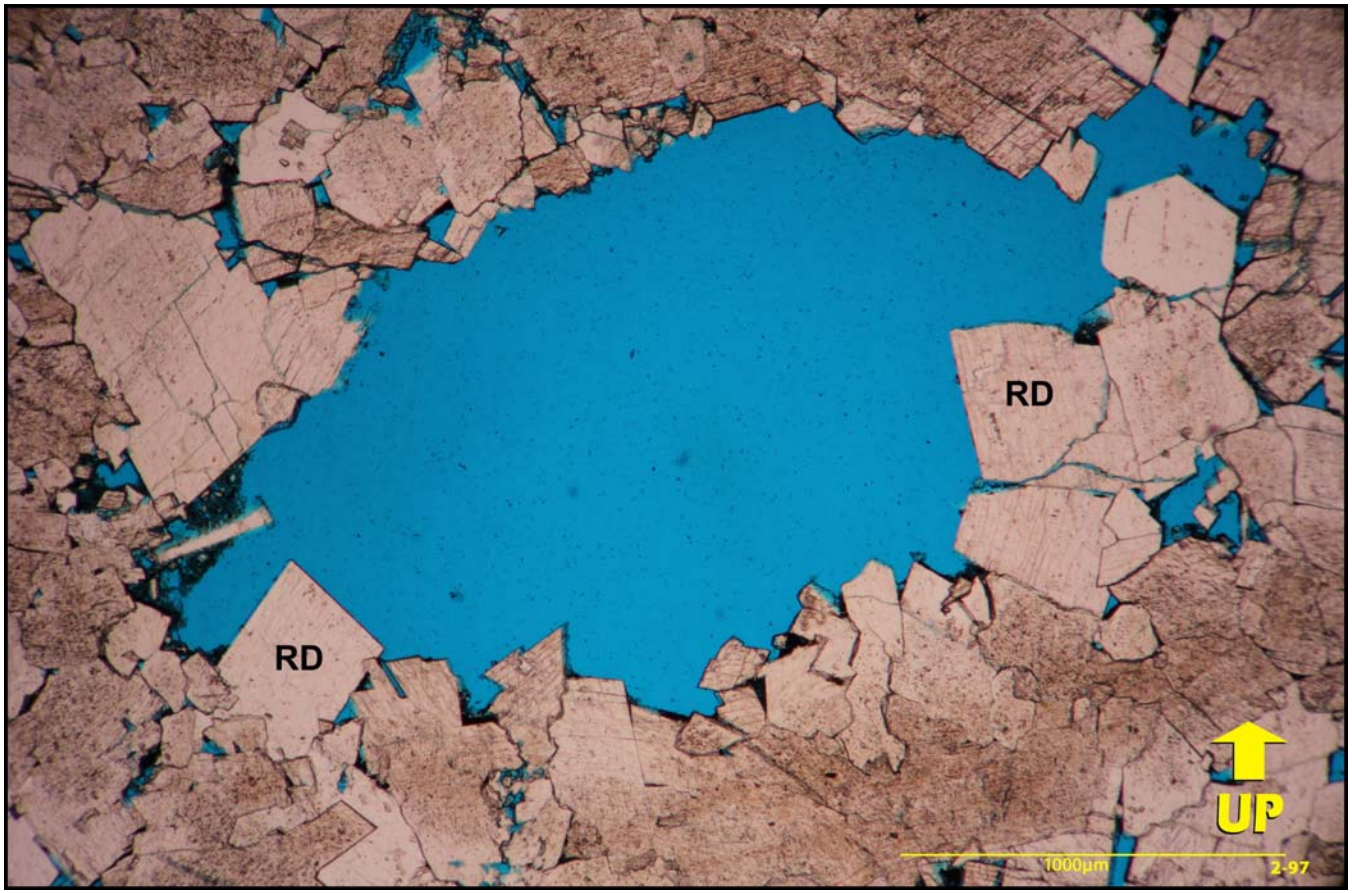

Photomicrograph illustrating an open finger-shaped biomold of uncertain affinity. Crystals of rhombic dolomite (RD) partially infill the biomold. Photomicrograph taken using plane-polarized light. Muskox D-87, 2083.91 m.

Figure D36

Core photograph of a matrix-rich clast-supported chaotic dolobreccia, but with some aspects of crackle and mosaic breccias. White coloured dolomite and calcite cements infill some sheltered pores that occur beneath breccia clasts. Bitumen infills narrow fractures (arrows) confined to the breccia clasts. Photograph taken of a wetted core surface. Kusrhaak D-16, 12007.5 ft.

Figure D37

Core photograph of a matrix-rich clast-supported chaotic dolobreccia, but with some aspect of crackle and mosaic breccias. The pore sheltered beneath breccia clasts near the centre of the photograph is fringed by fine unstained white saddle dolomite cement crystals and is infilled by later Alizarin-Red S stained calcite cements. Bitumen infills narrow fractures (arrows) confined to the breccia clasts. The general lower-left to upper-right alignment of the more elongated narrow fractures in the breccia clasts suggests that fracturing followed brecciation. Photograph taken of a wetted core surface. Kusrhaak D-16, 12020.05 ft.

Figure D38

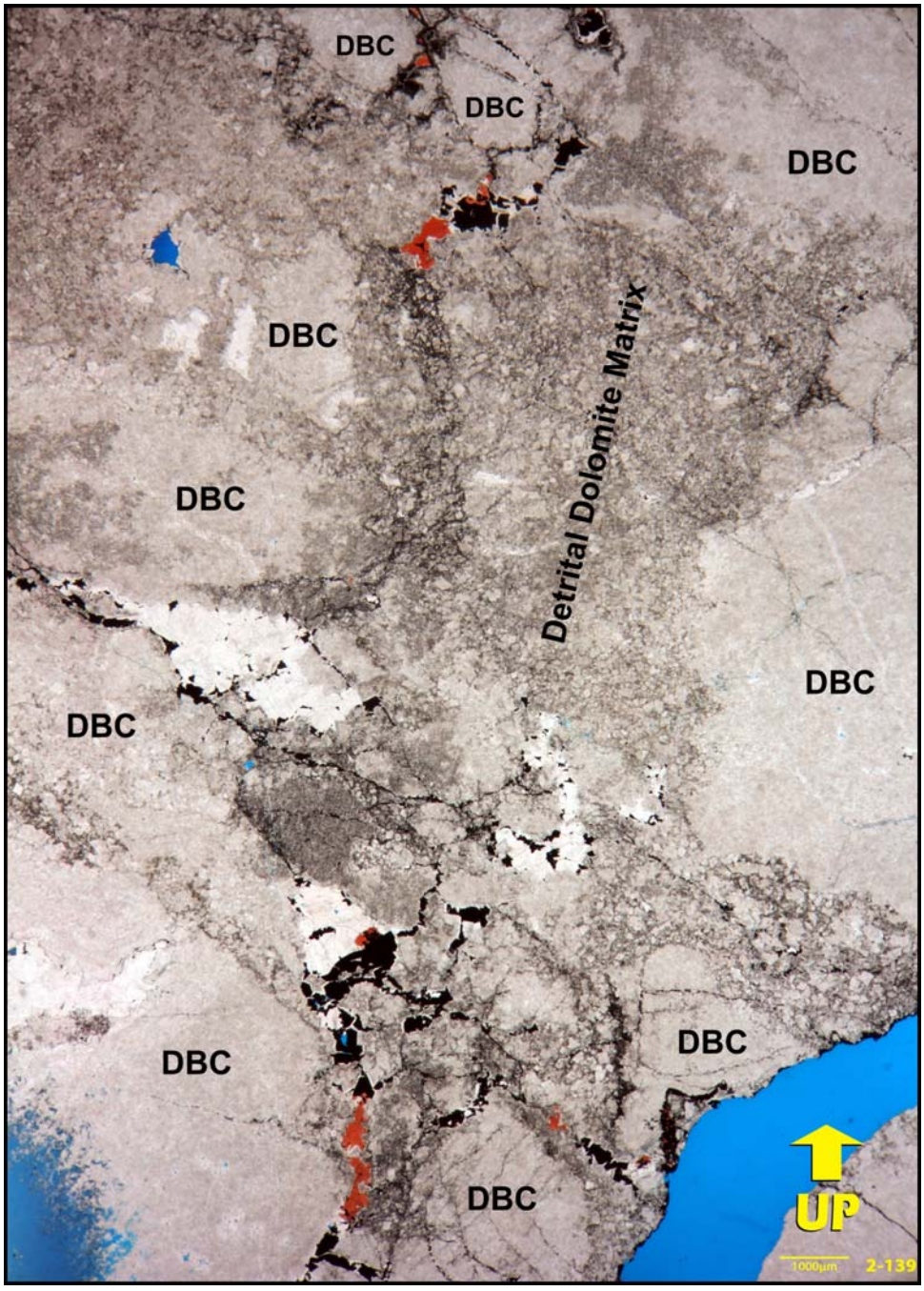

Overview showing the fine detrital dolomite matrix between the coarser dolobreccia clasts (DBC). Saddle dolomite and calcite cements, as well as some bitumen, infill fractures and some sheltered pores, unfilled by the detrital dolomite matrix, between the breccia clasts. Photomicrograph taken with transmitted plane-polarized light using a binocular microscope. Kusrhaak D-16, 12000.25 ft.

Figure D39

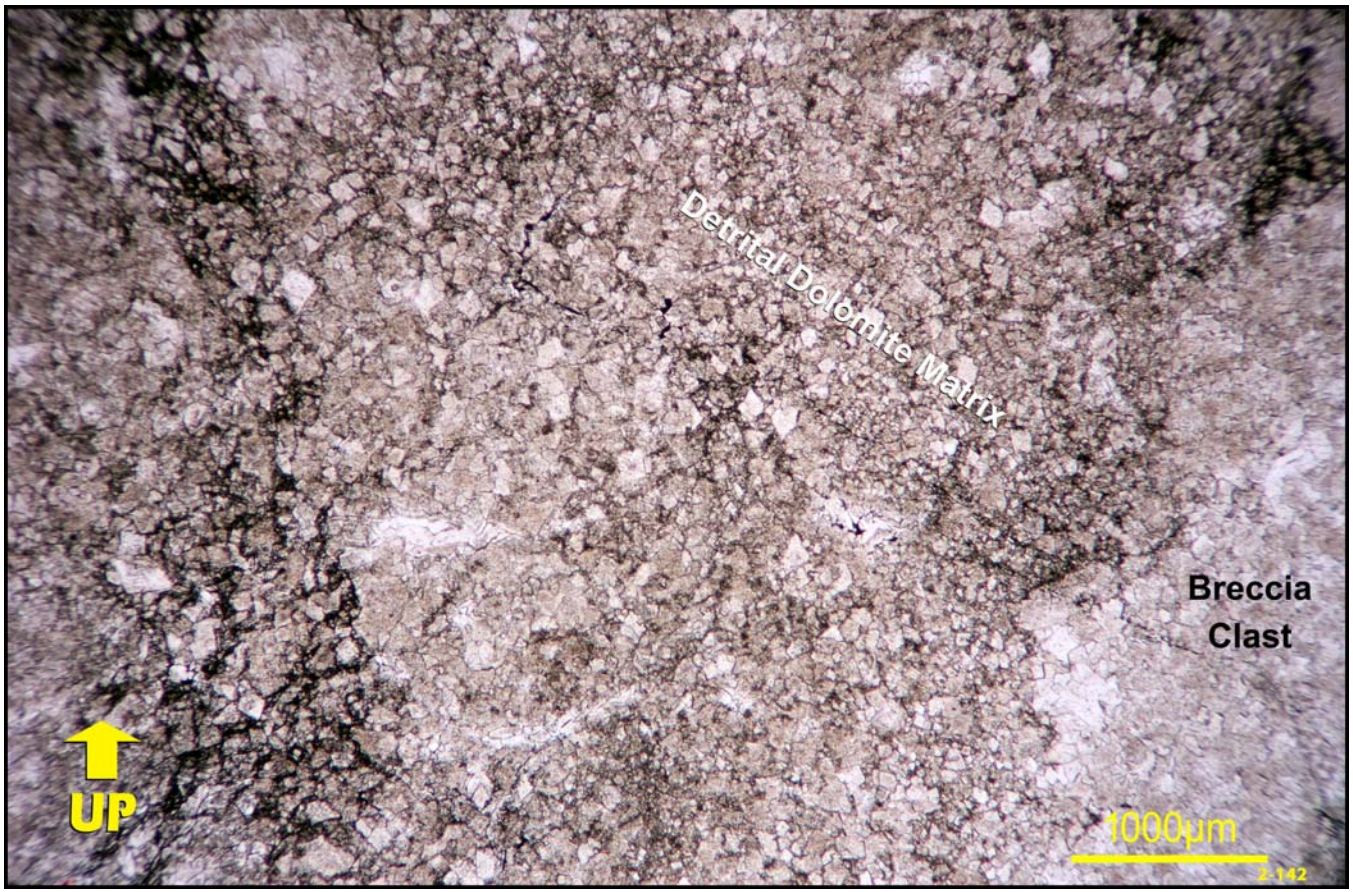

Photomicrograph at a higher magnification of the detrital dolomite matrix in the dolobreccia illustrated in the previous photomicrograph. The matrix consists of mud (micron scale) to fine sand-sized dolomite particles. Photomicrograph taken using plane-polarized light. Kusrhaak D-16, 12000.25 ft.

Figure D40

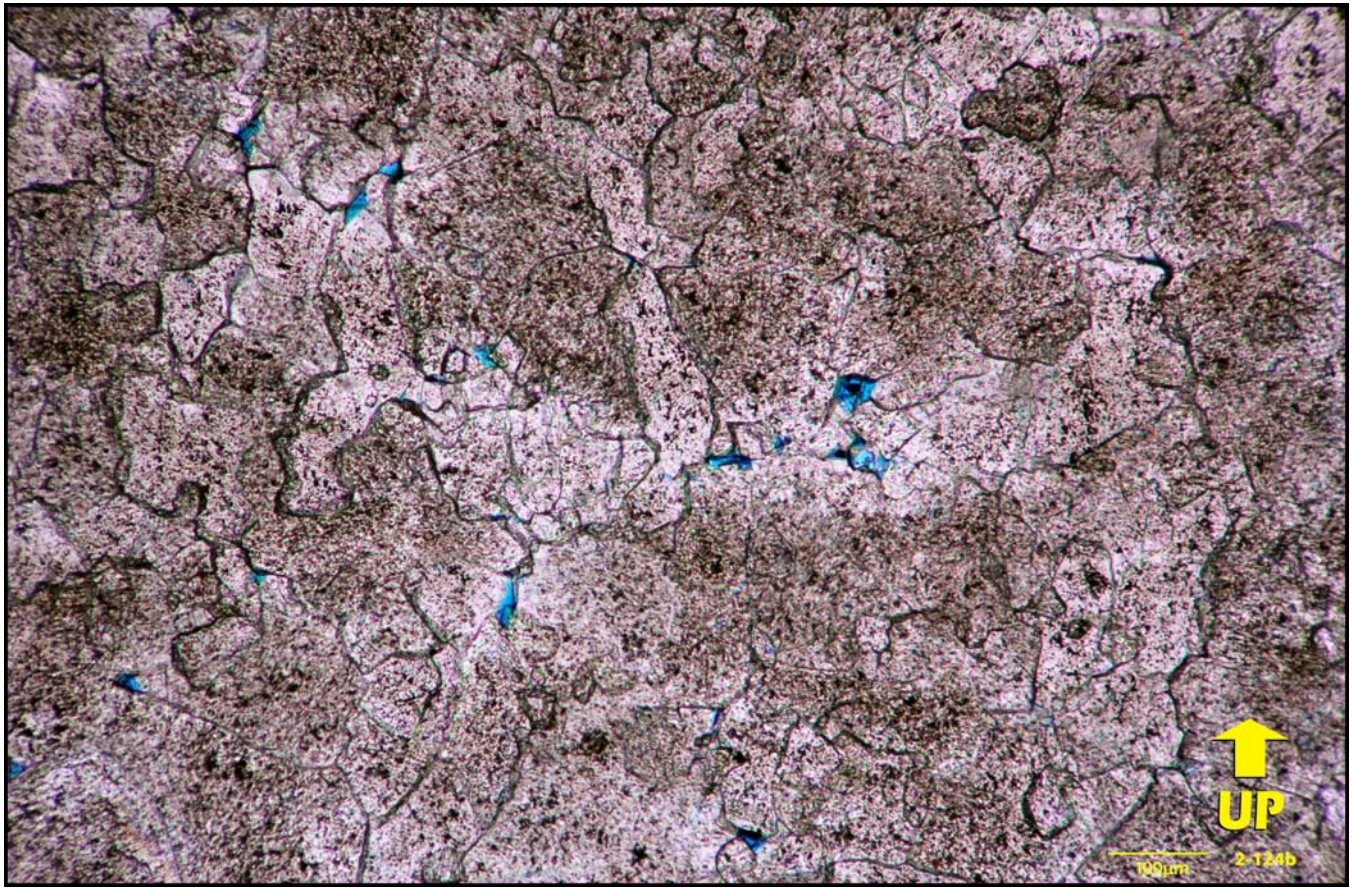

Photomicrograph illustrating dolomite replacing a clast of a tabular stromatoporoid. The dolomite consists of mainly sand-sized crystals with curved boundaries. The dark-coloured masses correspond to positions where the dolomite has replaced the laminae and pillars of the stromatoporoid. The more clear, inclusion-lean dolomite masses correspond to positions where the dolomite has either overgrown primary intraskeletal pores or replaced calcite cements that infilled these pores. This sample has minor intercrystalline porosity. Photomicrograph taken using plane-polarized light. Kusrhaak D-16, 11461.09 ft.

Figure D41

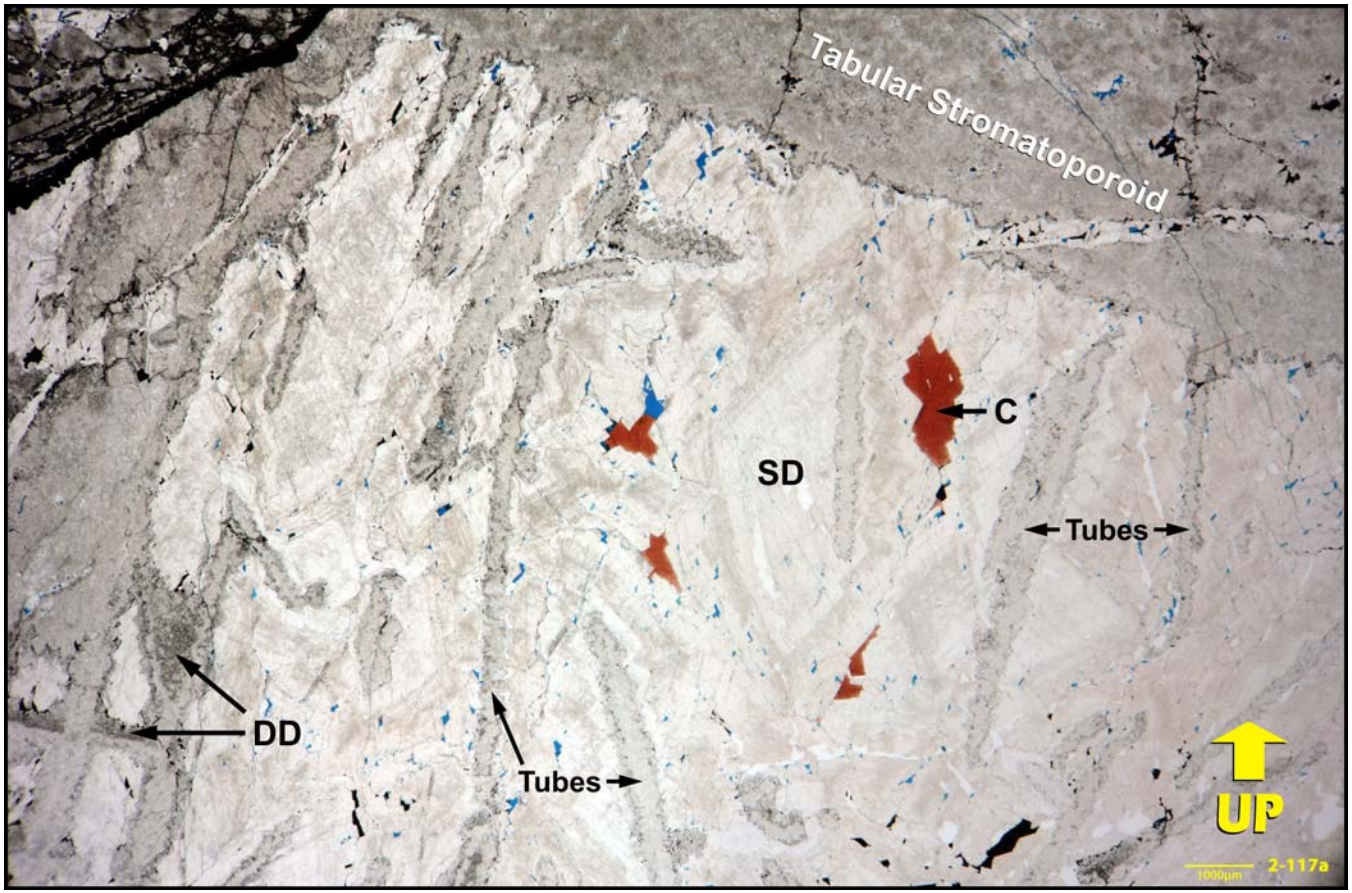

Overview illustrating tubular masses of uncertain original composition that grew in a pendent manner down into a pore sheltered by an overlying tabular stromatoporoid clast (illustrated in Figure D40). At the far left side of the photomicrograph, the tubes coalesce to form wider masses and even have cross-partitions that connect the individual tubes. Detrital dolomite internal sediment (DD) occurs above the cross-partitions. The intervening areas between the tubes are infilled by crystals of saddle dolomite (SD) and by even later coarser crystals of non-ferroan calcite (C). Photomicrograph taken with transmitted plane-polarized light using a binocular microscope. Kusrhaak D-16, 12461.09 ft.

Figure D42

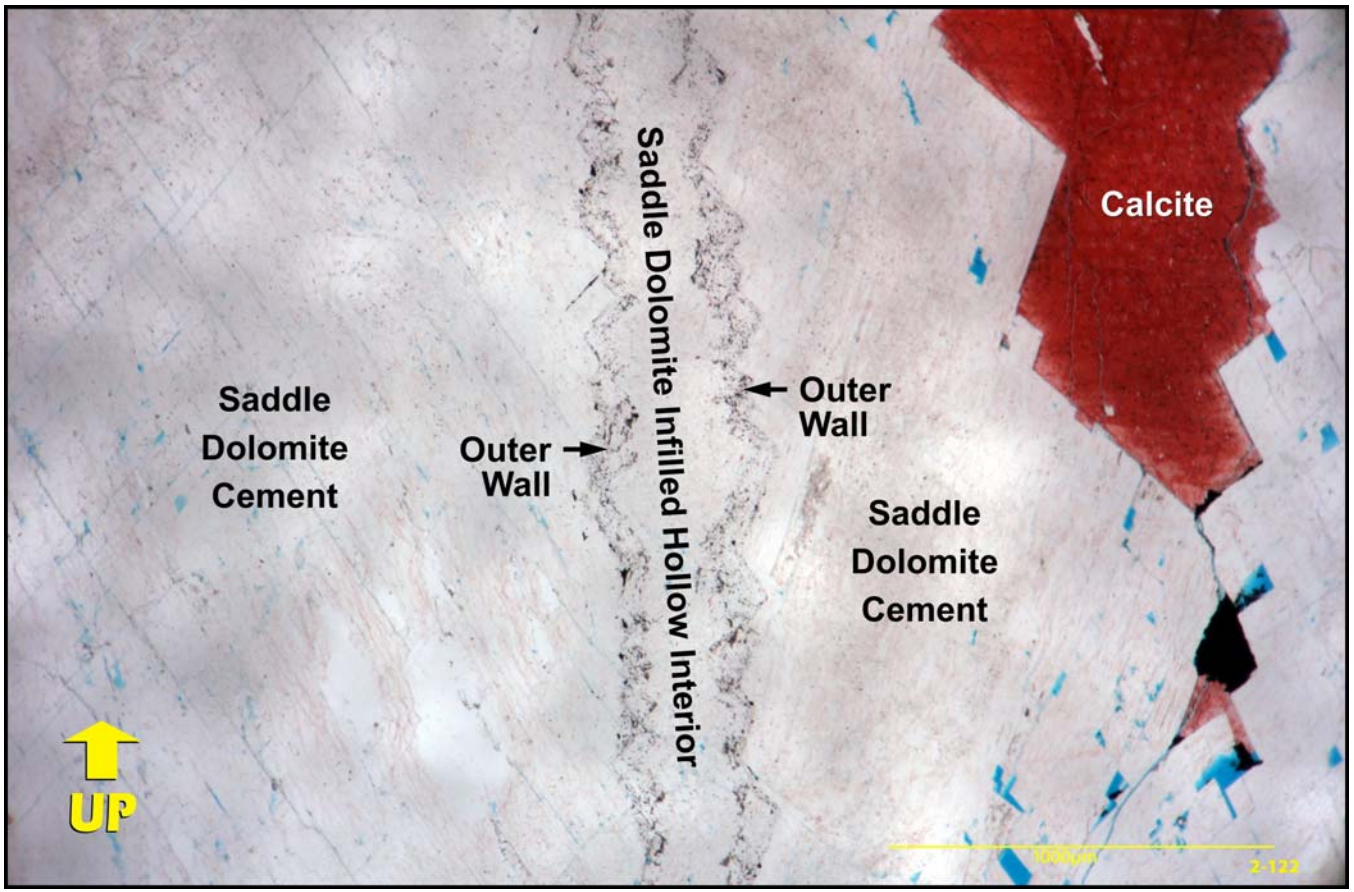

Photomicrograph taken at a higher magnification of one of the pendent tubes illustrated in the photograph in Figure D41. The tube consists of a narrow outer wall replaced by saddle dolomite, with bitumen inclusions, and a hollow interior infilled by saddle dolomite. Photomicrograph taken using plane-polarized light. Kusrhaak D-16, 12461.09 ft.

Figure D43

Core photograph of a dolobreccia varying from matrix-rich clast-supported chaotic breccia to crackle or mosaic breccias. Note the steeply inclined stylolite (arrows) with subhorizontal sutures, indicative of lateral compression. The gradual continuum of sizes of dolomite particles from cm-scale breccia clasts to very fine (mud to silt-sized) detrital dolomite sediment supports the interpretation that both brecciation and the detrital dolomite matrix formed from mechanical compression and breakdown related to fault movement. Photograph taken of a wetted core surface. Kusrhaak D-16, 12470.24 ft.

Figure D44

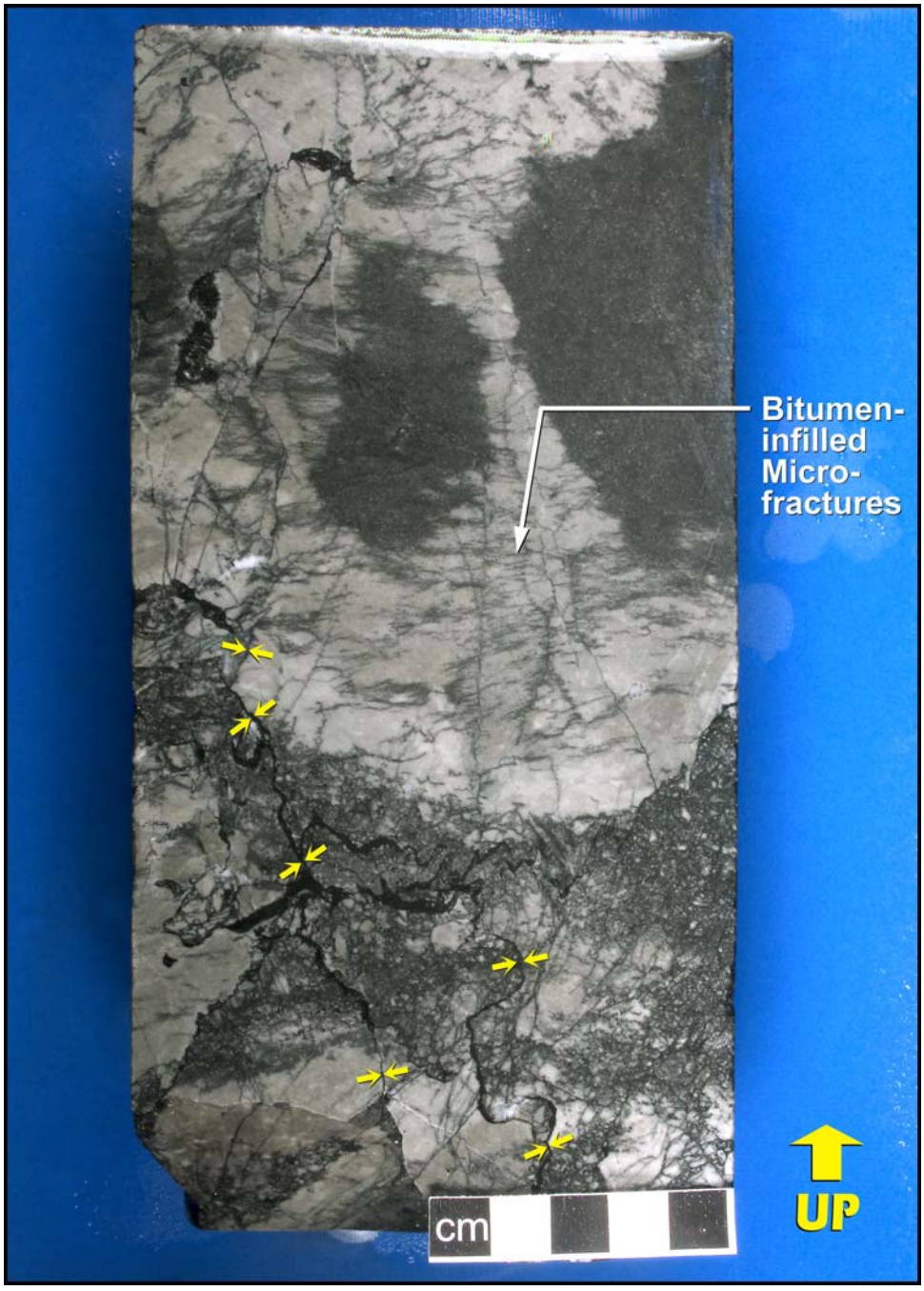

Core photograph illustrating steeply inclined stylolites (arrows) in a matrix-rich clast-supported chaotic dolobreccia. The presence of the steeply inclined stylolites implies lateral compression, possibly during fault movement. Bitumen-infilled microfractures occur in the large breccia clast in the upper part of the photograph. These microfractures have horizontal to subhorizontal orientations and are interpreted to have formed from uplift and the relaxation of vertical forces following brecciation. Photograph taken of a wetted core surface. Kusrhaak D-16, 12470.24 ft.

Figure D45

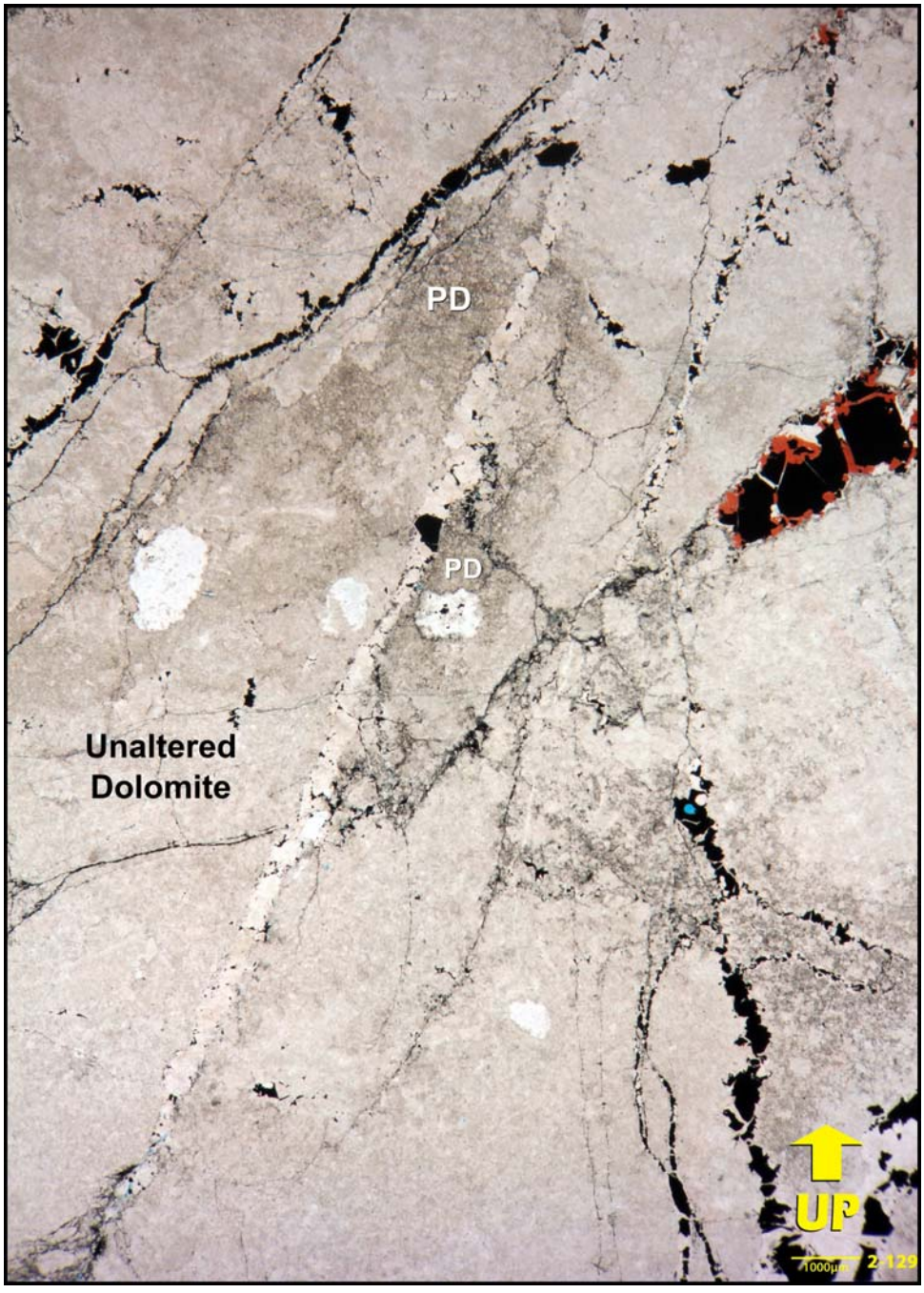

An overview of a mosaic to crackle breccia showing the preferential occurrence of fine particulate dolomite (PD) in the outer portion of breccia clasts adjacent to or close to fractures. The fractures were infilled later by saddle dolomite and calcite cements, as well as by bitumen. Photomicrograph taken with transmitted plane-polarized light using a binocular microscope. Kusrhaak D-16, 12024.20 ft.

Figure D46

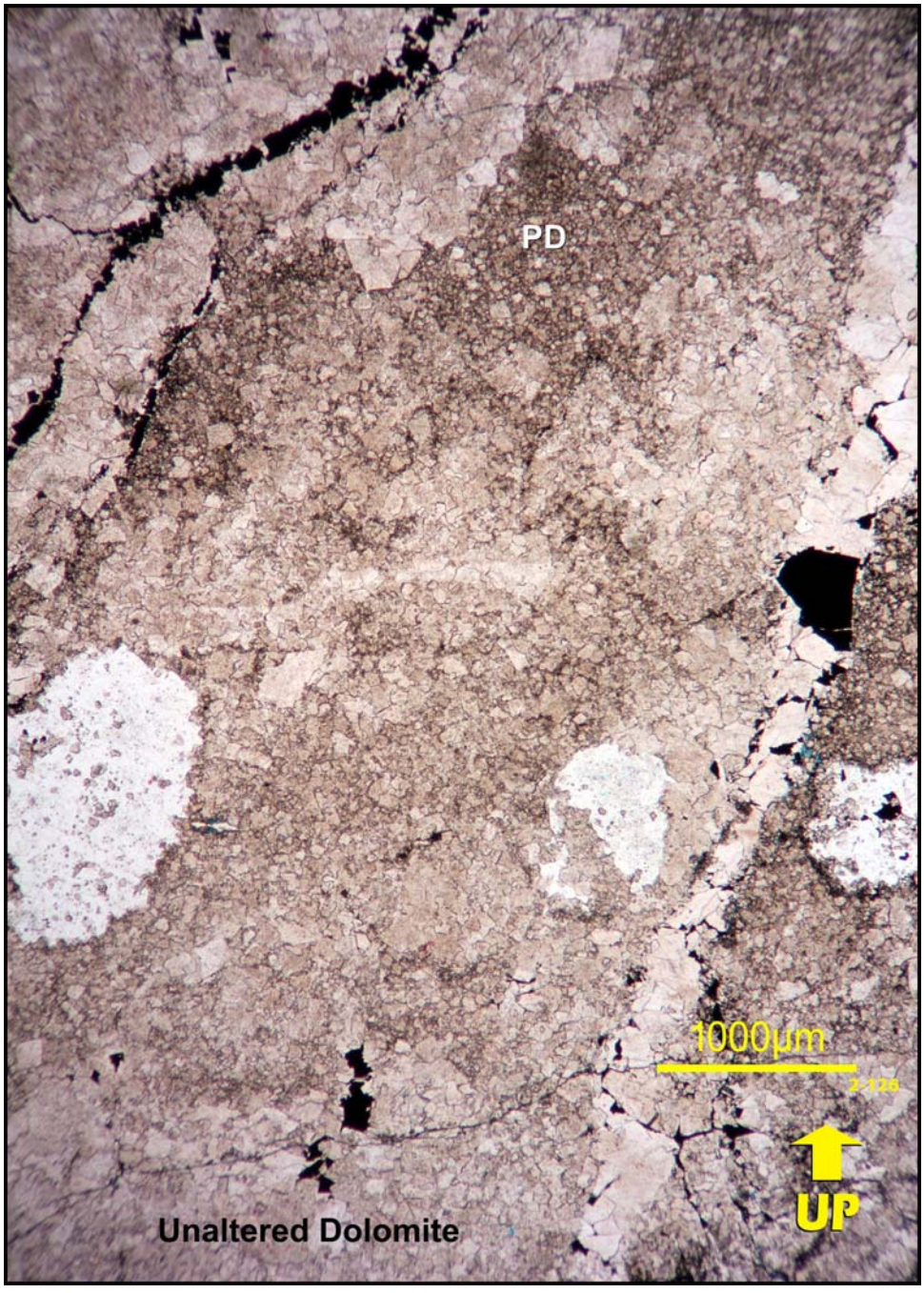

Photomicrograph taken at a higher magnification of one of the dolobreccia clasts from the previous photomicrograph. Fine particulate dolomite (PD) occurs in the upper part of the breccia clast and gradually becomes diminished downward. The fine particulate dolomite is interpreted to have formed *in situ* from the breakdown of the original dolomite, possibly by a chemical dissolution process. This fine *in situ* particulate dolomite is identical to the fine detrital dolomite matrix that occurs between dolobreccia clasts. Photomicrograph taken using plane-polarized light. Kusrhaak D-16, 12024.20 ft.

Figure D47

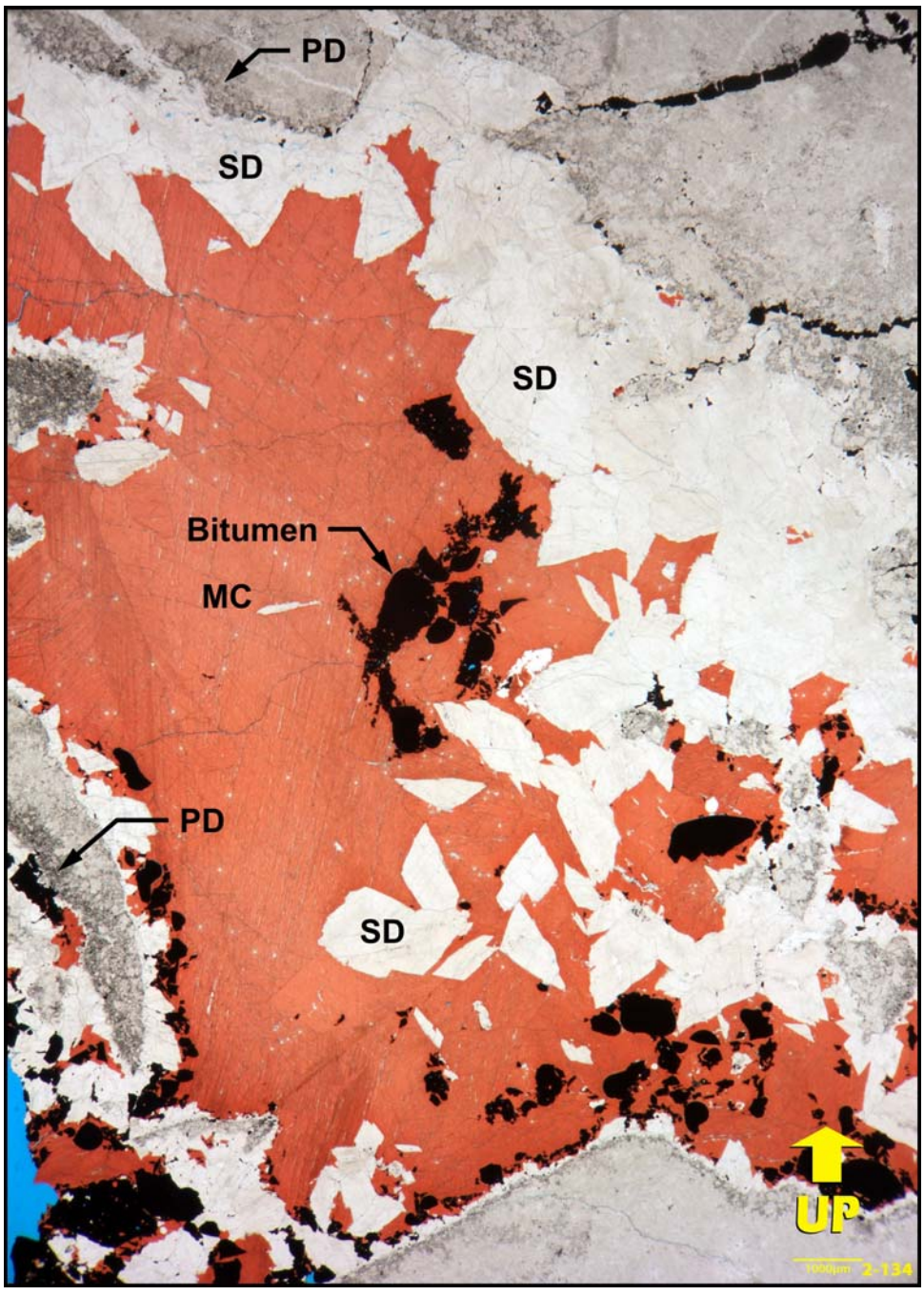

Overview of a portion of a clast-supported chaotic dolobreccia with saddle dolomite (SD), macrocalcite (MC) and bitumen infilling a sheltered pore that occurs between dolobreccia clasts. Note that fine particulate dolomite (PD) commonly occurs in the outer portions of the dolobreccia clasts. Photograph taken with transmitted plane-polarized light using a binocular microscope. Kusrhaak D-16, 12005.37 ft.

Figure D48

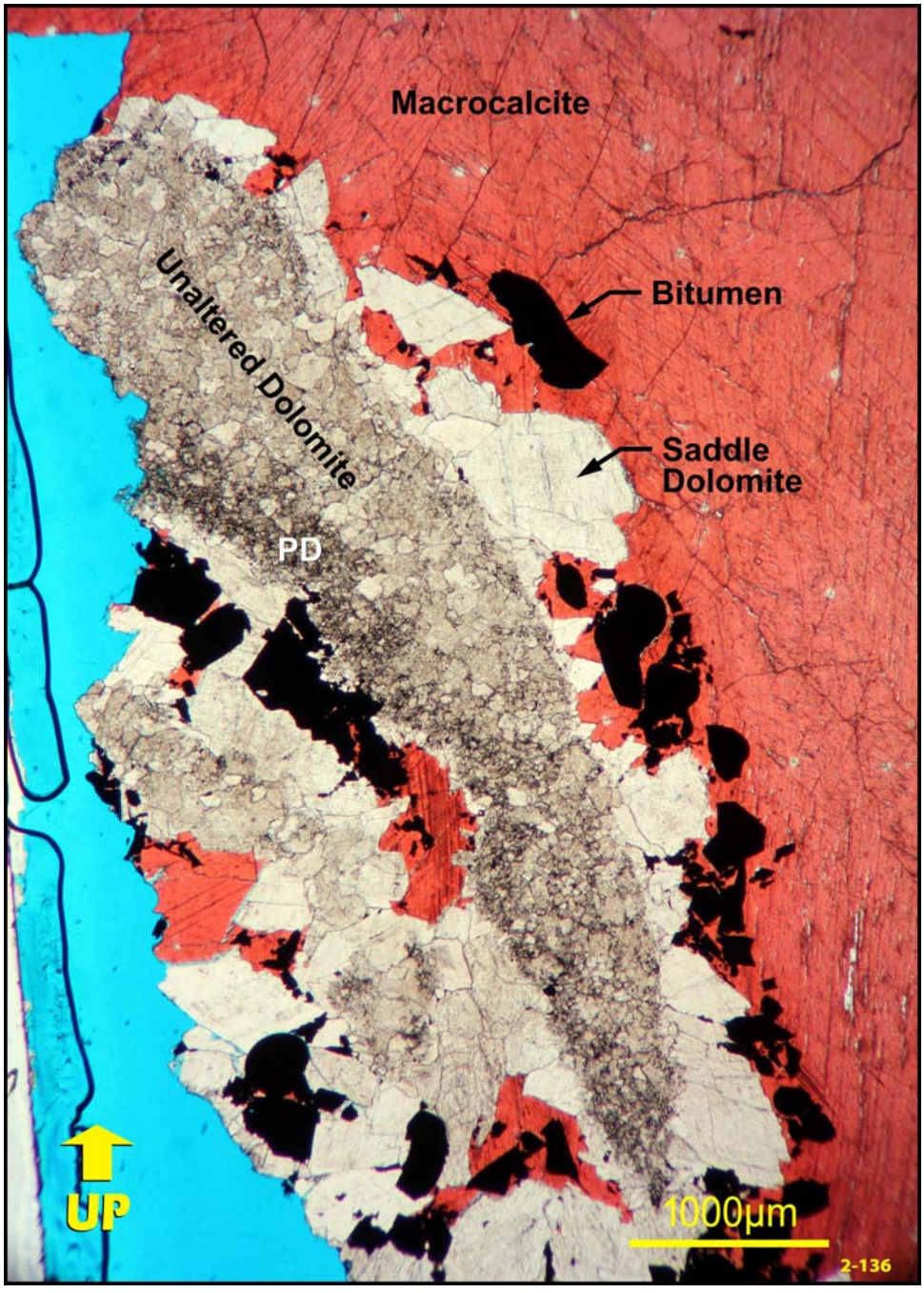

Photomicrograph taken at a higher magnification of one of the chaotic dolobreccia clasts in the previous photomicrograph. Fine particulate dolomite (PD) occurs along one of the margins of the clast and gradually becomes diminished away from this surface. This fine particulate dolomite is identical to that in the outer portions of dolobreccia clasts in mosaic or crackle breccias and to the detrital dolomite matrix between dolobreccia clasts. Photomicrograph taken using plane-polarized light. Kusrhaak D-16, 12005.37 ft.

Figure D49

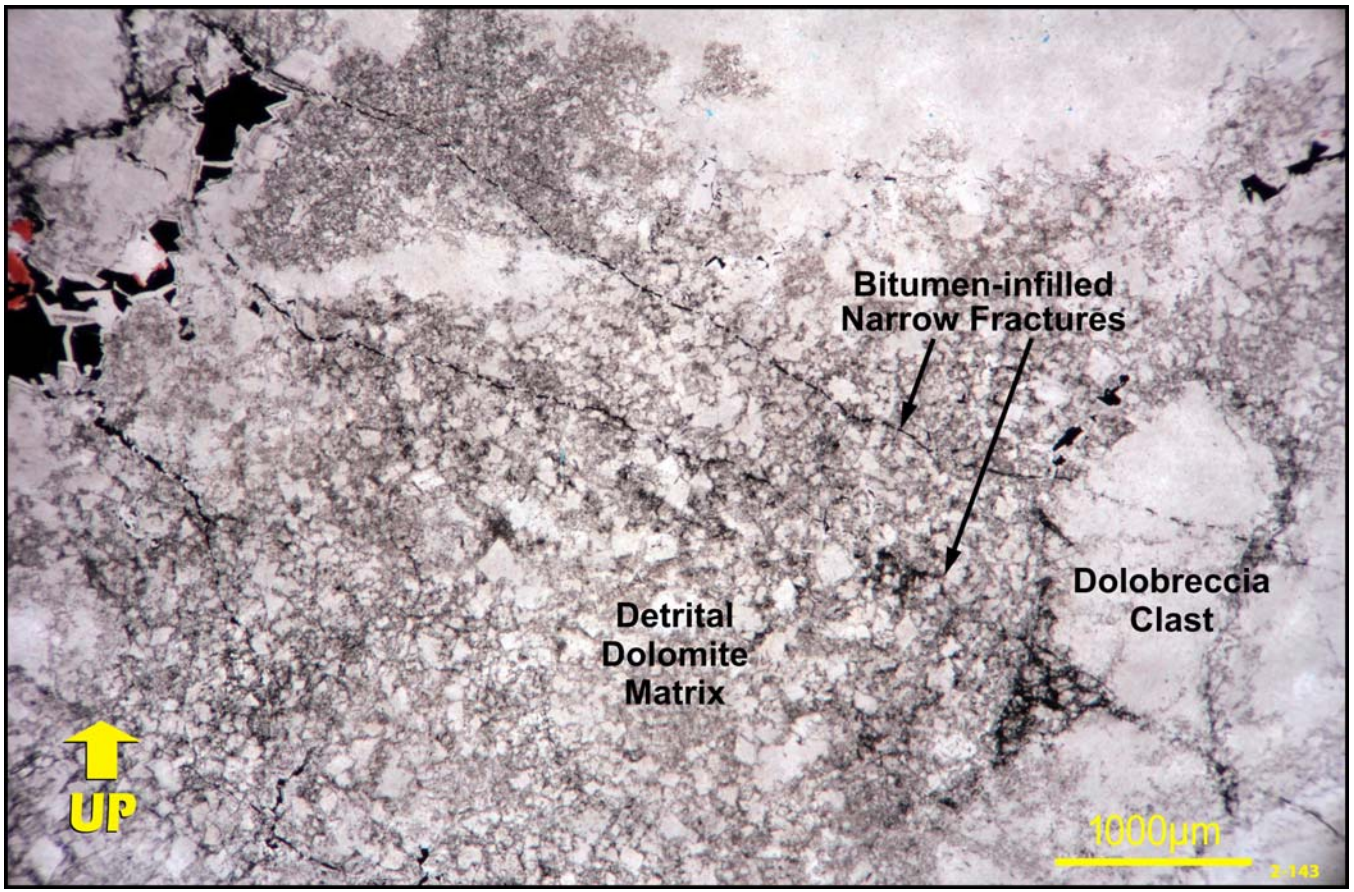

Photomicrograph illustrating bitumen-infilled narrow fractures that cut both dolobreccia clasts and the detrital dolomite matrix. Although these fractures clearly follow breccia formation, they are interpreted to be part of a related, albeit somewhat later, fault-related process. Photomicrograph taken using diffused plane-polarized light. Kusrhaak D-16, 12000.25 ft.

Figure D50

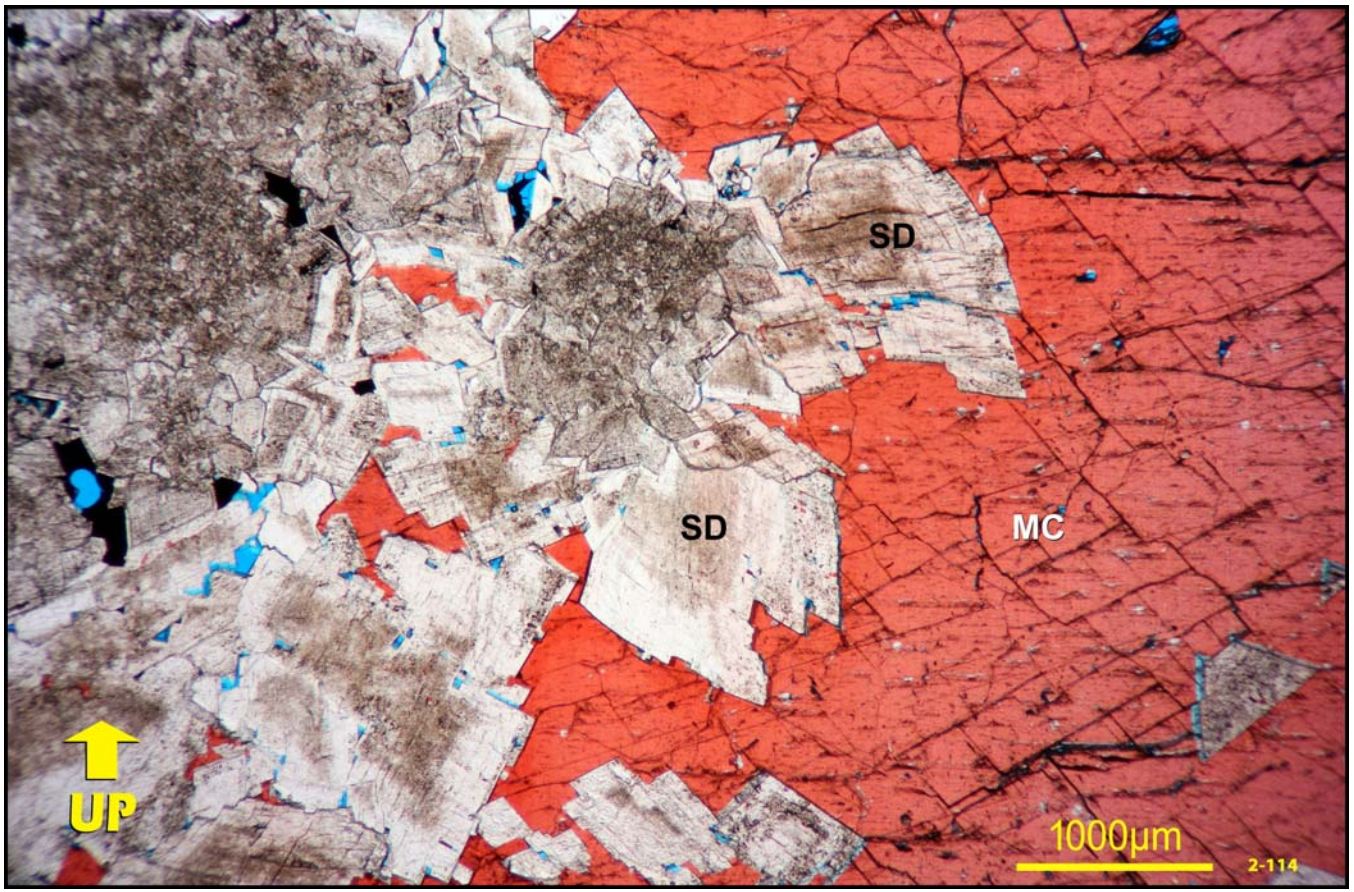

Photomicrograph of a portion of a pore sheltered beneath dolobreccia clasts showing a crystal of macrocalcite (MC) overgrowing finer crystals of saddle dolomite (SD) that nucleated on the dolobreccia clasts. The saddle dolomite crystals have either an inclusion-rich core and an inclusion-lean outer rim or consist of alternating bands of inclusion-rich and inclusion-lean zones. Photomicrograph taken using plane-polarized light. Kusrhaak D-16, 12468.20 ft.

Figure D51

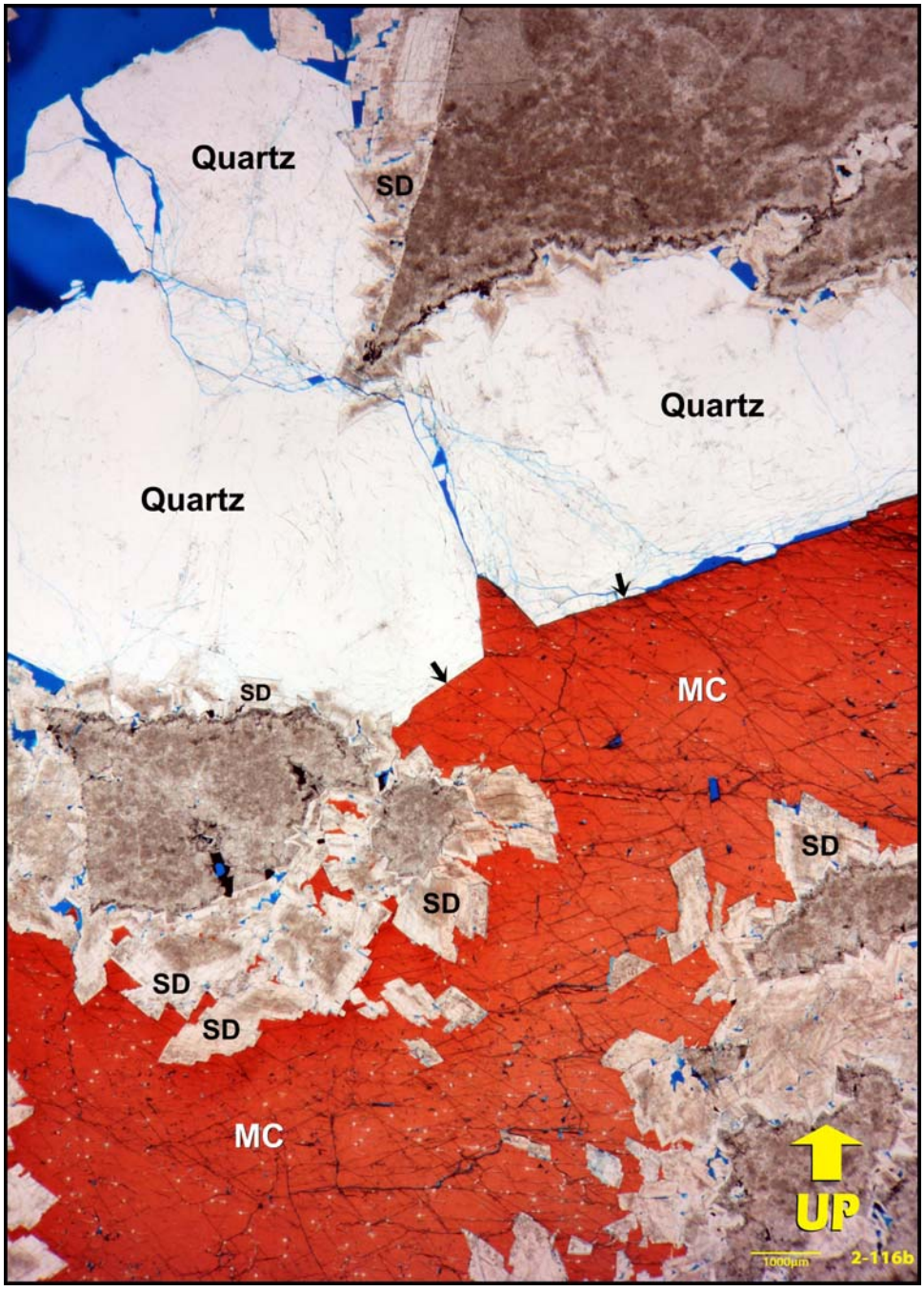

Overview of a portion of a pore sheltered beneath dolobreccia clasts. Crystals of saddle dolomite (SD) line the margins of the dolobreccia clasts, along the periphery of the pore, and are overgrown by either quartz crystals or by a single crystal of macrocalcite (MC). Euhedral crystal faces of the quartz (arrows) are overgrown by the macrocalcite crystal. Minor porosity within the sheltered pore remains open. Photomicrograph taken with transmitted plane-polarized light using a binocular microscope. Kusrhaak D-16, 12468.20 ft.

Figure D52

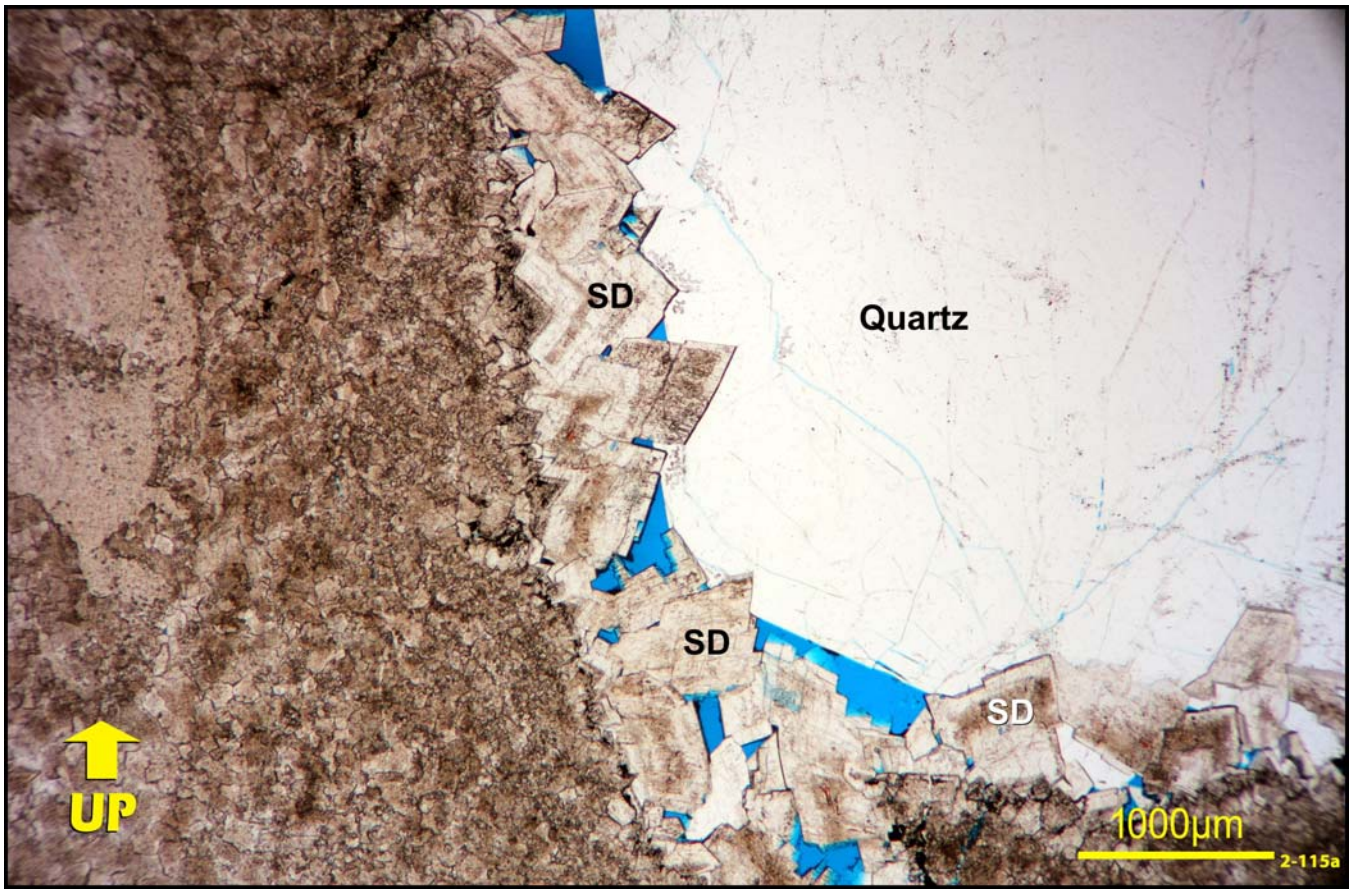

Photomicrograph showing a portion of a pore sheltered beneath dolobreccia clasts. Crystals of saddle dolomite (SD) line the margin of dolobreccia clasts and are overgrown by a quartz crystal that partly infills the pore. Euhedral crystal faces of both saddle dolomite and quartz face the remaining open pore. Photomicrograph taken using plane-polarized light. Kusrhaak D-16, 12468.20 ft.

Figure D53

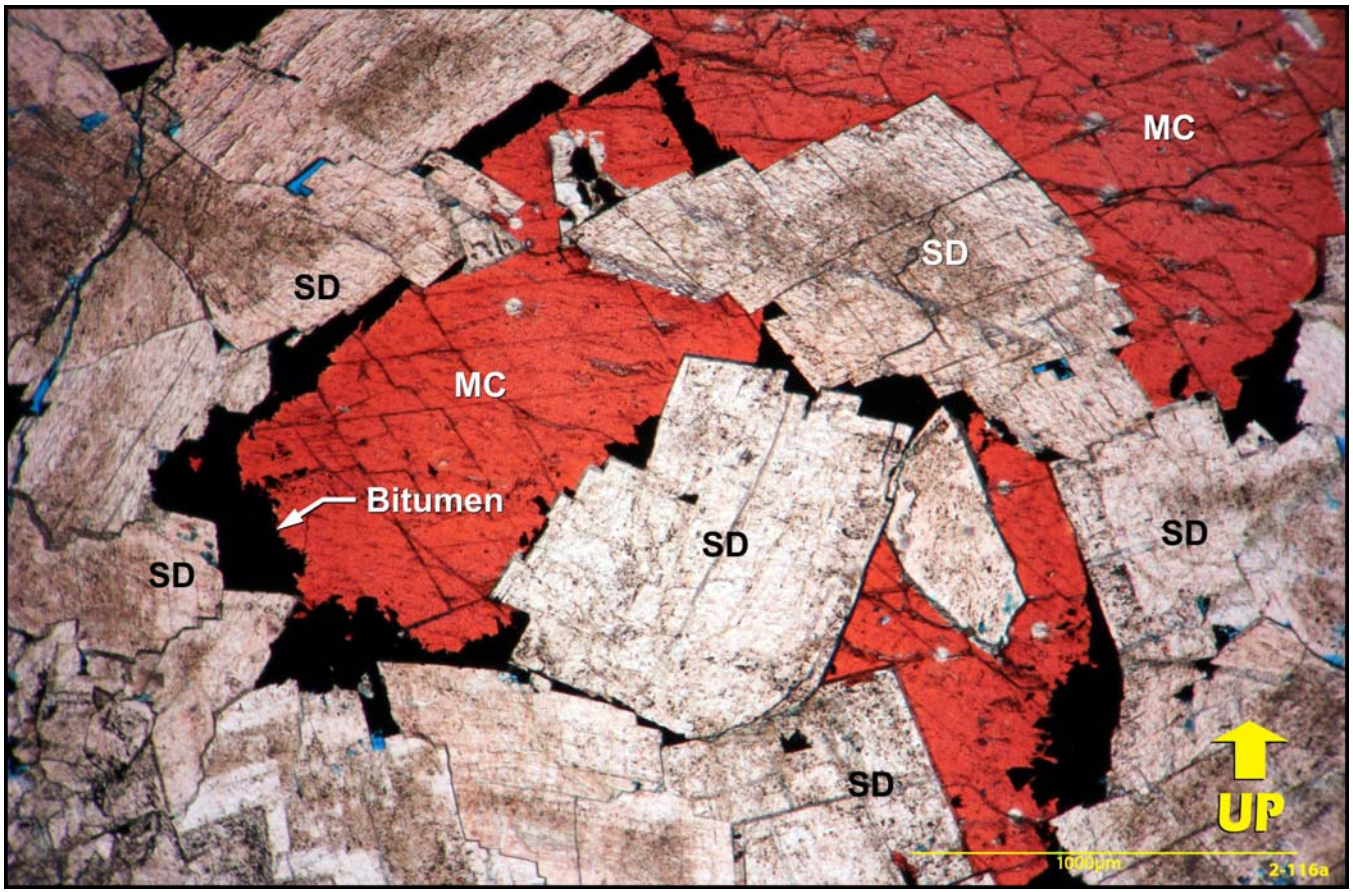

Photomicrograph of a portion of a pore sheltered beneath dolobreccia clasts showing the occurrence of bitumen. Bitumen occurs in vugs of dissolution origin in a macrocalcite crystal (MC), along the margins of the earlier-formed crystals of saddle dolomite (SD). This position would have been the preferential flow path of fluids that dissolved the more soluble calcite phase. Photomicrograph taken using plane-polarized light. Kusrhaak D-16, 12468.20 ft.

Figure D54

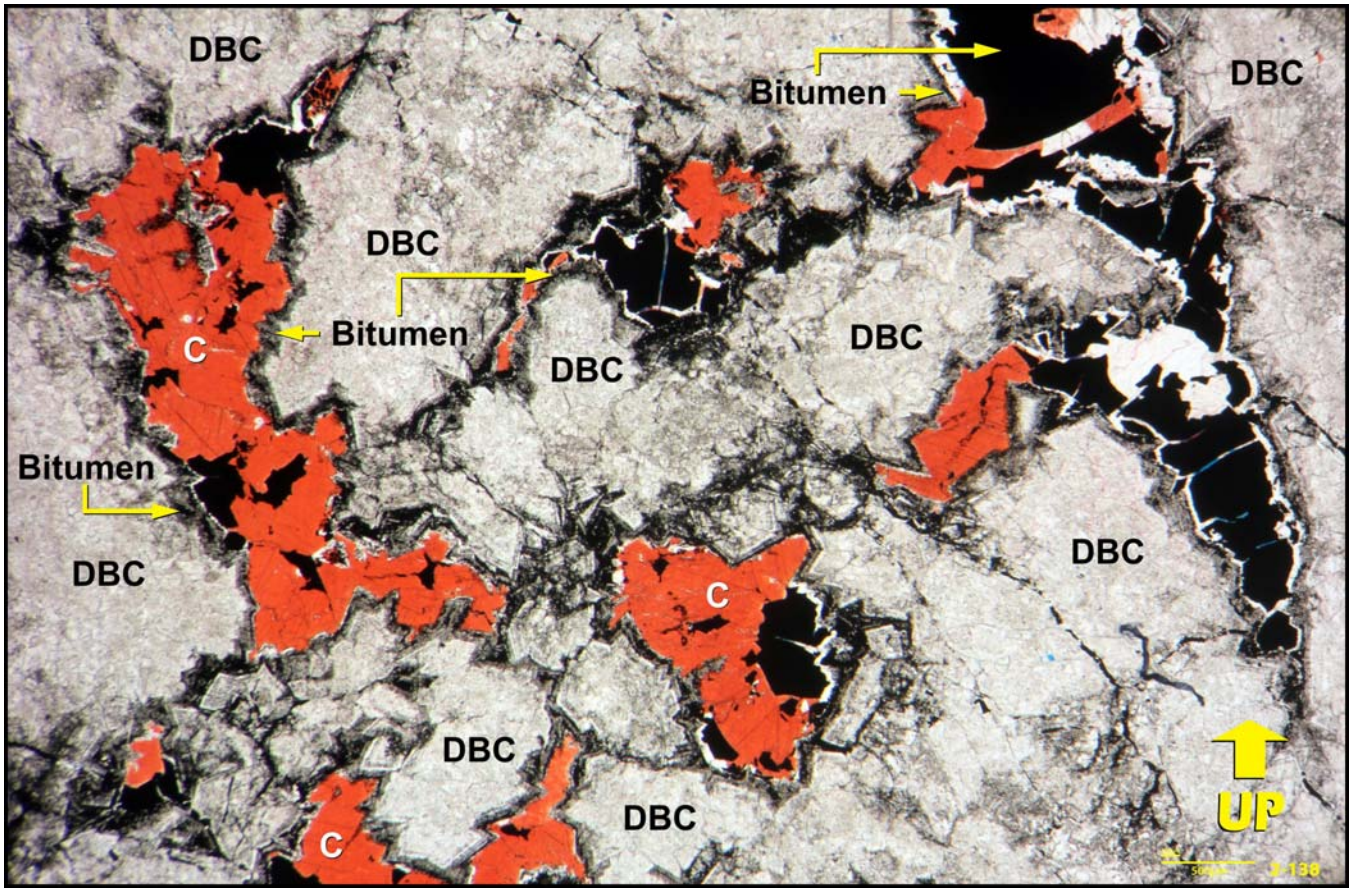

Overview of sheltered pores between dolobreccia clasts (DBC) illustrating the occurrence of bitumen. These pores are lined by crystals of saddle dolomite and are completely infilled by coarse sand-size crystals of non-ferroan calcite (C). Bitumen infills micropores of dissolution origin that occur in bands within the outer part of saddle dolomite crystals, as well as solution vugs in the calcite and saddle dolomite crystals. The bands of bitumen-infilled micropores within saddle dolomite crystals can be traced virtually completely around the periphery of the pores. Photomicrograph taken with transmitted plane-polarized light using a binocular microscope. Kusrhaak D-16, 12000.25 ft.

Figure D55

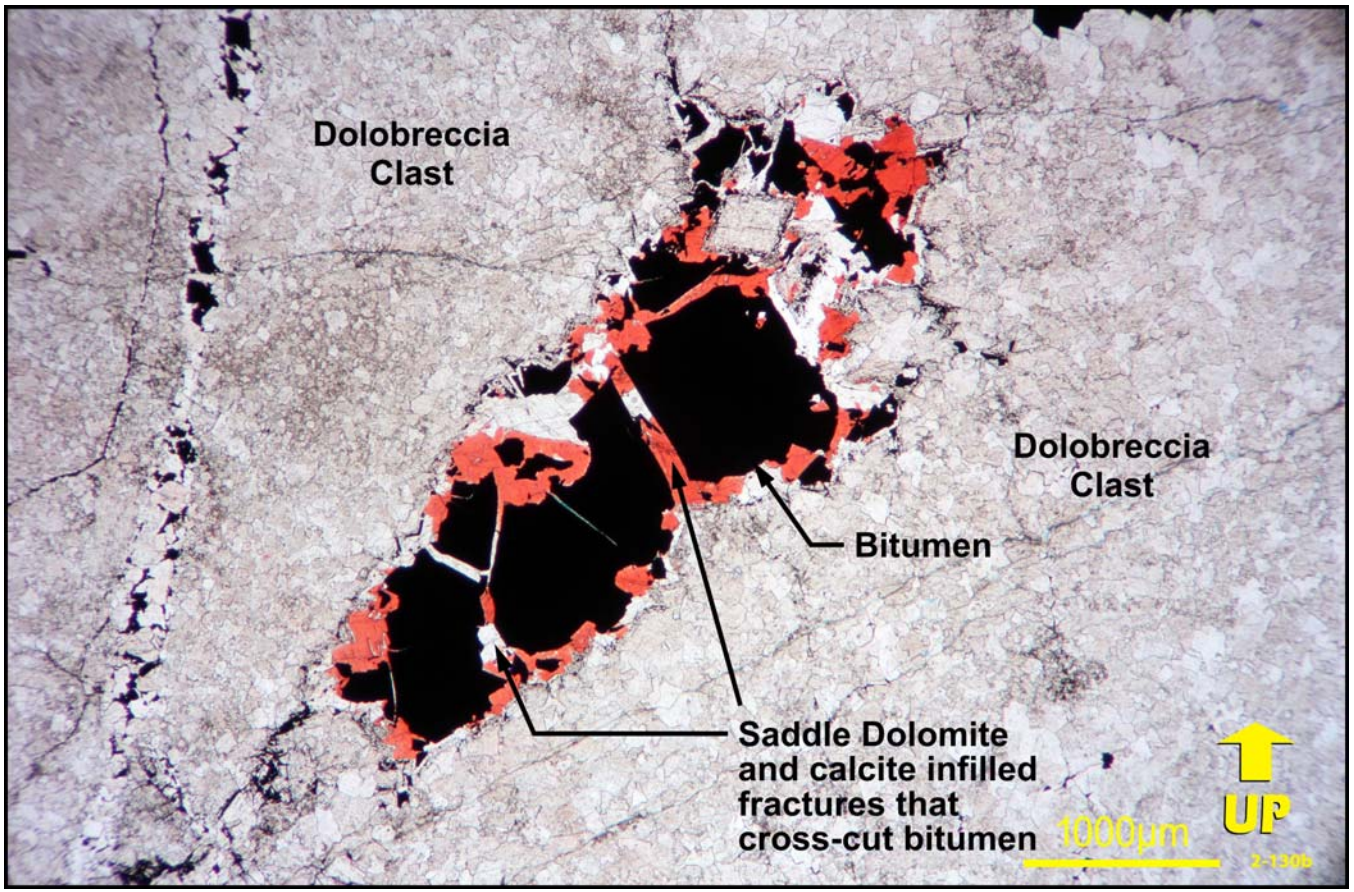

Photomicrograph illustrating fractures that cross-cut bitumen present within a sheltered pore between dolobreccia clasts. The bitumen infills vugs of dissolution origin within crystals of non-ferroan calcite (stained red). Significantly, the fractures do not extend into the surrounding dolobreccia clasts. These fractures are interpreted as having formed by shrinkage from de gassing during the transformation of oil to bitumen. These short fractures are infilled by a later phase of both saddle dolomite and non-ferroan calcite. Photomicrograph taken using plane-polarized light.
Kusrhaak D-16, 12024.20 ft.

ACKNOWLEDGEMENTS

Throughout the study Keith Dewing provided keen insights, from both the examination of cores and thin sections, as well as from discussions. David Sargent prepared the figures, as well as assembled this report. Glenn Edwards took photographs of rock samples from the cores. Odette Abaco (Abaco Geological Consulting Ltd.) took the thin-section photomicrographs. Deanna Pratt (Copy Writers) typed the manuscript and provided sound editorial advice. Graham Davies (Graham Davies Geological Consulting Ltd.) and Laurie Slezak (P. Geol.) aided through discussions on aspects of thin-section petrography. One-inch diameter core plugs were drilled by the staff at the Alberta Energy Resources Conservation Board Core Research Centre and analyzed by AGAT Laboratories. Calgary Rock and Materials Services made all the thin sections. I would also like to thank Rick Fontaine and Bill Dwyer for laying out the cores at the Geological Core and Sample Repository at the Geological Survey of Canada (GSC)-Calgary and for assistance in sampling the cores. As well, I would be remiss in not acknowledging Dr. John Harper, former Director of the Geological Survey of Canada-Calgary, for his vibrant leadership at the GSC-Calgary during much of the period in which this study was conducted.

APPENDIX

ONE-INCH DIAMETER CORE PLUG ANALYSIS

Well Name	Depth (ft.) and metres where noted	Gas Permeability			Porosity	Density (Kg/m^3)	
		K_{max} (mD)	K_{90} (mD)	K_V (mD)		Bulk	Grain
Bent Horn A-57	11049.92	<.01	-	-	0.011	2670	2700
Bent Horn A-57	11037.78	0.01	-	-	0.006	2670	2690
Bent Horn A-57	11022.79	0.03	-	-	0.007	2680	2700
Bent Horn A-57	10996.25	<.01	-	-	0.006	2700	2710
Bent Horn F-72	10436.20	<.01	-	-	0.011	2690	2720
Bent Horn F-72	10428.40	0.01	-	-	0.015	2670	2710
Bent Horn F-72	10412.50	<.01	-	-	0.010	2690	2720
Bent Horn F-72	10392.00	<.01	-	-	0.011	2670	2700
Bent Horn F-72	10374.00	<.01	-	-	0.008	2660	2690
Bent Horn F-72	10358.50	<.01	-	-	0.011	2650	2680
Bent Horn F-72	10320.33	<.01	-	-	0.008	2680	2700
Bent Horn F-72	10296.00	<.01	-	-	0.008	2660	2690
Bent Horn F-72	10280.30	<.01	-	-	0.006	2690	2710
Bent Horn F-72A	10134.50	<.01	-	-	0.011	2680	2710
Bent Horn N-72	11527.70	<.01	-	-	0.013	2710	2740
Bent Horn N-72	11524.50	<.01	-	-	0.007	2690	2710
Bent Horn N-72	10730.10	<.01	-	-	0.012	2670	2700
Bent Horn N-72	10726.25	<.01	-	-	0.011	2670	2700
Bent Horn N-72	10525.40	<.01	-	-	0.009	2660	2690
Cape Fleetwood M-21	11521.10	0.01	-	-	0.007	2670	2690
Cape Fleetwood M-21	11518.00	<.01	-	-	0.008	2660	2690
Cape Fleetwood M-21	11505.80	<.01	-	-	0.005	2710	2720
Cape Fleetwood M-21	11503.00	<.01	-	-	0.006	2680	2700
Richardson Point G-12	7962.00	<.01	-	-	0.007	2690	2710
Richardson Point G-12	7960.00	<.01	-	-	0.009	2680	2700
Richardson Point G-12	7916.90	<.01	-	-	0.010	2660	2690
W. Bent Horn C-44	10496.30	<.01	-	-	0.009	2660	2690
W. Bent Horn C-44	10489.40	0.13	-	-	0.011	2660	2690
W. Bent Horn C-44	10456.00	0.24	-	-	0.008	2690	2710
King Point West B-53	3620.50 m	<.01	-	-	0.007	2670	2690
King Point West B-53	3618.90 m	0.01	-	-	0.006	2680	2700
King Point West B-53	3612.00 m	0.01	-	-	0.005	2690	2700
Key Point O-51	7409.35 m	<.01	-	-	0.005	2700	2710
Key Point O-51	7394.05 m	0.03	-	-	0.006	2690	2700
Key Point O-51	7386.25 m	<.01	-	-	0.005	2690	2700
Key Point O-51	7374.88 m	<.01	-	-	0.007	2670	2700

AGAT® Laboratories